Exploring Sources of Magnetospheric Plasma Using the Validated SWMF

by
Daniel T. Welling

A dissertation submitted in partial fulfillment
of the requirements for the degree of
Doctor of Philosophy
(Atmospheric and Space Sciences)
in The University of Michigan
2009

Doctoral Committee:

Professor Tamas I. Gombosi, co-Chair
Associate Professor Aaron J. Ridley, co-Chair
Professor Andrew F. Nagy
Professor Quentin F. Stout
Associate Professor Michael W. Liemohn

The wonderful thing about science
is that it doesn't ask for your faith,
it just asks for your eyes.
-XKCD

Knowledge, like air, is vital to life.
Like air, no one should be denied it.
-V for Vendetta

Dedicated to Kylie,
who reminded me to believe in myself,
and Aurora,
who reminded me what is most important in life.

ACKNOWLEDGEMENTS

During the toughest part of my graduate career, Dr. Bob Clauer told me that grad school is "10% intelligence, 90% perseverance." Of all the things I learned in graduate school, this lesson quickly became the most important. I have found that perseverance comes much easier when you have the right people around you. I am thankful to have been surrounded by all the right people.

I would like to recognize my mentors inside of the department for investing their time and energy into my degree. First of these is Dr. Clauer, who brought me into this program. Dr. Tamas Gombosi deserves equal thanks for taking me on as his student after Dr. Clauer left Michigan for Virginia Tech. My doctoral committee also deserves recognition for the time they have sacrificed guiding my progress. Most importantly, I give my sincerest thanks to Dr. Aaron Ridley for showing me how to grow from a good student to a good scientist.

My family has been a constant source of strength during my graduate school work, and for them I am eternally grateful. My wife, Kylie, has never wavered in her support for my goals. My parents, Mary Ann, George, Marv, and Lori, as well as Dale and Cindy, are all key figures in my life, who put me in a position to be writing this doctoral thesis today. All of my siblings, Amy, David, Katie, Steven, Skylar, Holly, and Scott, have helped me reach my goals in their own special ways. My daughter Aurora, whose picture remains mounted on my computer monitor today, has a smile that always cheers me up.

Finally, I would like to thank my friends, both inside and outside the department. Troy Dowd, Rick Runkle, Jason Sondergeld, and Matt Hudson made the transition from Marquette to Ann Arbor as easy as coming home. Alex Glocer, Ofer Cohen,and Jared Bell could always be looked to when I needed help, as well as a good laugh. While traveling to the artic is not a true vacation, it was made easier by Tom O'Brien, Ken Arnett, Xia Cai and Anna DeJong. Jan Beltran makes the morning smoother with her vast collection of rock music, and John Schwanneke's constant encouragement ensured that I continued to write during the final months. Without these people, graduate school would have been far more difficult to finish.

TABLE OF CONTENTS

LIST OF FIGURES

Figure

LIST OF TABLES

Table

CHAPTER I

Introduction

1.1 The Solar Wind

A common misconception among the layperson concerning the space environment is that, beyond massive bodies such as planets, space is a perfect vacuum. While this approximation is useful under some circumstances, it is far from the truth. Plasma, or electrically charged gas, is omnipresent and non-trivial in the universe.

The most important source of plasma in our solar system is the Sun. Hot plasma is accelerated from the solar surface to supersonic speeds into the heliosphere. That this plasma, now known as the "solar wind", reaches supersonic flow speeds was originally predicted by Parker (1958); it was finally measured by the Luna 1 satellite in 1959.

This plasma is in the presence of the Sun's strong magnetic field. The bulk flow of the plasma and the time evolution of the magnetic field lines are coupled through the induction equation, seen in Equation 1.1. The first term on the right side of Equation 1.1 is dependent on flow velocity, while the second term is dependent on the magnetic viscosity (Equation 1.2). In a slow moving plasma, the first term may be neglected and the induction equation becomes a diffusion equation, allowing the field to diffuse through the plasma. Alternately, when the plasma is fast moving and

viscosity is low (for example, the conductivity, σ_0, is very high), the second term may be neglected and the magnetic field is "frozen in" to the advecting plasma and the two move together. This is the case in the solar wind, so the Sun's magnetic field is pulled out into the heliosphere along with the plasma. Away from the sun, this field is known as the "Interplanetary Magnetic Field" or IMF.

$$\frac{\partial \mathbf{B}}{\partial t} = \nabla \times (\mathbf{u} \times \mathbf{B}) + \eta_m \nabla^2 \mathbf{B} \tag{1.1}$$

$$\eta_m = \frac{1}{\sigma_0 \mu_0} \tag{1.2}$$

Average solar wind characteristics at the first Lagrangian location (L_1, ~1.5 million km from the Earth radially towards the Sun) are listed in Table 1.1. These values are hardly stable, however, as transient events on the solar surface can quickly increase the values listed in Table 1.1 as well as the complexity of the IMF (Hundhausen, 1972; Burlaga, 1995). Examples of such events are solar flares, coronal mass ejections (CMEs), and high-speed streams. These events vary with the solar cycle (Feynman and Gu, 1986).

Quantity	Value
Plasma number density	$8.7 cm^{-3}$
Bulk velocity	$470 km/s$
Proton Temperature	$1.2 * 10^5 K$
Magnetic field strength	$6.2 nT$

Table 1.1: Average plasma and IMF properties at the L_1 point. (Gombosi, 1998).

1.2 The Terrestrial Magnetosphere

The Earth's magnetic field stands as an obstacle to the solar wind. Because the frozen flux approximation, as described above, is still valid, solar wind particles and the IMF cannot readily cross terrestrial field lines. This causes the formation of

a hydrodynamic shock that transitions the solar wind from supersonic to subsonic velocities while increasing the density, temperature, and field strength (typically by factors of 4.) Further inside the region of shocked solar wind plasma, a cavity forms that separates solar wind fields and plasmas from terrestrial fields and plasmas (Chapman and Bartels, 1940). This cavity stretches from 10 Earth Radii (R_E) upstream of the planet to several hundred R_E downstream and is known as the magnetosphere.

Figure 1.1 shows a basic diagram of the a slice of the magnetosphere taken in the noon-midnight meridian. Just inside of the bow shock is the magnetosheath, a region encasing the magnetosphere that contains shocked solar wind plasma. The boundary between the region of solar wind and terrestrial magnetic field and plasma marks the magnetopause.

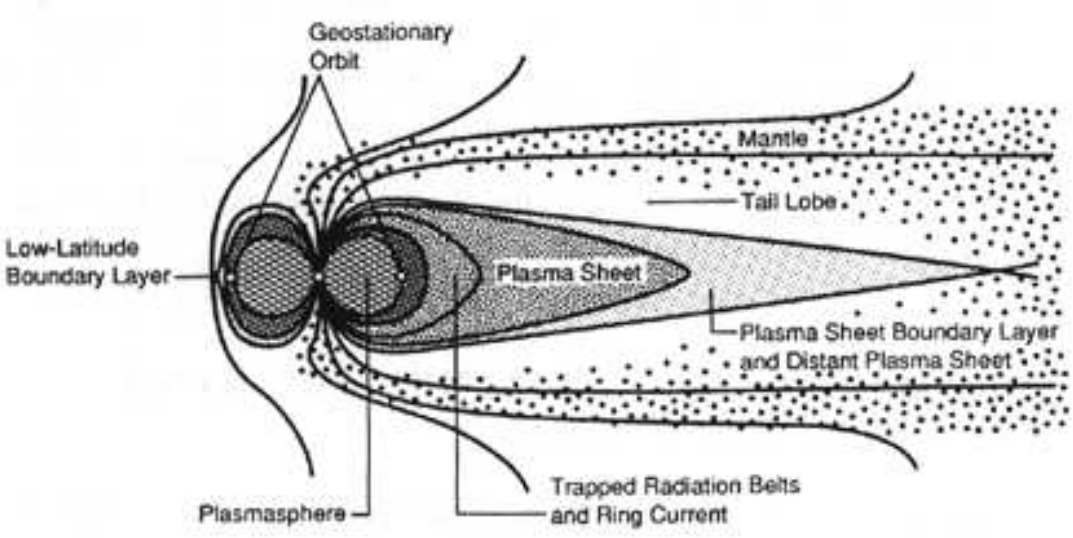

Figure 1.1: Noon-midnight meridian slice of the magnetosphere showing locations of various regions and particle populations. In this diagram, the Sun is to the left. (Wolf, 1995).

Without a flowing solar wind, the shape of the magnetosphere would follow the dipole shape of the Earth's intrinsic field. Because of the validity of the frozen flux approximation, however, the dayside magnetopause is pushed Earthwards. The

standoff point in the equatorial plane can be expressed as a balance between the ram pressure of the solar wind and the magnetic pressure of the terrestrial field (Equation 1.3, where u is the bulk flow of the solar wind, ρ is the mass density, and B_0 is the strength of the terrestrial field at the standoff point). On the nightside of the magnetosphere, field lines are stretched downstream to form a magnetotail. The size and shape of the magnetosphere is highly variable, depending on solar wind velocity and density and, as will be discussed later, reconnection rates and magnetospheric plasma pressure.

$$\rho u^2 \approx \frac{B_0}{2\mu_0} \tag{1.3}$$

The inner magnetosphere region houses three important particle populations that overlap spatially. The first is the plasmasphere, extending out to a radius of 3-5 Earth Radii (R_E). This population is cold ($\sim$1eV) and dense ($\sim 100 cm^{-3}$) plasma whose source is the upper atmosphere of the Earth's atmosphere, the ionosphere (Horwitz and Singh, 1991). Overlapping this region and extending to 6-7R_E are the radiation belt and ring current populations. There is no clear distinction between these populations, but it is reasonable to treat ring current particles as those with keV energies and radiation belt particles as those with 100's of KeV to MeV energies (Wolf, 1995). The source of the ring current and outer radiation belt particles is plasma entering through the plasma sheet; the mechanisms and ultimate sources will be discussed in Sections 1.3 and 1.4 and investigated in depth in Chapter V.

Particles in the magnetosphere are subject to three basic types of motion: cyclotron motion about field lines, bounce motion between magnetic mirror points along field lines as the lines diverge and converge between magnetic poles, and drift perpendicular to the magnetic field (Kivelson, 1995; Gombosi, 1998). The third is the most important when following bulk flows of particles through the inner magne-

tosphere as it is responsible for the transport of the plasma throughout this system.

Drift perpendicular to the field is the result of an external force (**F**) changing the gyroradius of a particle of mass m and charge q as it circulates around a field line (**B**). The general form is seen in Equation 1.4. There are three types that are of concern for the inner magnetosphere: drift due to electric fields and drift due to gradients and curvatures of the magnetic field. The drift equation combining all of these effects is seen in Equation 1.5. In the first term, **E** refers to the corotational electric field caused by the rotation of the Earth. This field converges on the body and is always present in the magnetosphere; other large scale electric fields may also be imposed (see Section 1.3). The result of this term is a total plasma drift that rotates with the Earth, independent of mass or charge. The next term is the combined gradient and curvature drifts. Unlike the first, this term is dependent on the particle's charge and kinetic energy perpendicular to and parallel to the magnetic field. The resulting drift causes ions to flow opposite of the Earth's direction of rotation; electrons opposite of the ions. Energy dependence creates the distinction between cold plasmasphere particles, whose drift is dominated by the first term, and ring current and radiation belt particles, whose drift is dominated by the second.

$$\mathbf{V}_{Drift} = \frac{m}{q}\frac{\mathbf{F}\times\mathbf{B}}{B^2} \tag{1.4}$$

$$\mathbf{V}_{Drift} = \frac{\mathbf{E}\times\mathbf{B}}{B^2} + \frac{m}{q}\frac{v_{\parallel}^2 + \frac{1}{2}v_{\perp}^2}{B}\frac{\mathbf{B}\times\nabla B}{B^2} \tag{1.5}$$

There are several ways in which particles may escape the magnetosphere (Wolf, 1995). The first is transport via guiding center drift to the magnetopause and into the sheath. Another important mechanism is loss into the ionosphere. As charged particles bounce between mirror points, they may be disrupted (typically via plasma waves) as to change their mirror point to be deeper within the atmosphere, where

they cannot exit. Finally, charge exchange with neutral particles allows previously charged particles to leave the confines of the Earth's magnetic field. Investigation of the importance of various loss processes is a rich and important field of study.

1.3 Energy Transfer Between the Solar Wind and Magnetosphere

Energy transfer from the solar wind involves transferring the momentum of the solar wind to the fields and particles inside of the magnetosphere. This imposes a motional electric field, or that which satisfies the generalized Ohm's law when the conductivity is sufficiently large (Equation 1.6), across the magnetosphere, changing the drift paths of particles flowing due to Equation 1.5. The net effect is large-scale convective motion of plasma and field lines. There are two well researched and accepted modes for transferring energy from the solar wind to the magnetosphere.

$$\mathbf{E} = -\mathbf{u} \times \mathbf{B} \tag{1.6}$$

The first mechanism is that of magnetospheric convection, as conceived by Dungey (1961, 1963). This process begins with reconnection at the subsolar point. This opens the magnetosphere to the motional electric field of the solar wind and creates large-scale convective motion of terrestrial field lines from the dayside reconnection point to the far tail and back again.

Magnetic reconnection (Dungey, 1953), the ignition of the Dungey magnetosphere, occurs when two plasma populations with antiparallel magnetic field configurations are brought together at an interface (Figure 1.2, left panel). As the two populations and their respective magnetic fields are pressed together, the first term of Equation 1.1 begins to diminish as $\mathbf{u} \rightarrow 0$. Simultaneously, kinetic collisionless processes diminish the conductivity (σ_0 in Equation 1.2) (Drake and Shay, 2007), increasing

the importance of the second term on the right hand side of Equation 1.1. This allows the field to diffuse across the boundary, changing the topology of the magnetic field (Figure 1.2, center). Plasma flowing into the reconnection site is accelerated away along with the newly reconnected lines (Figure 1.2, right).

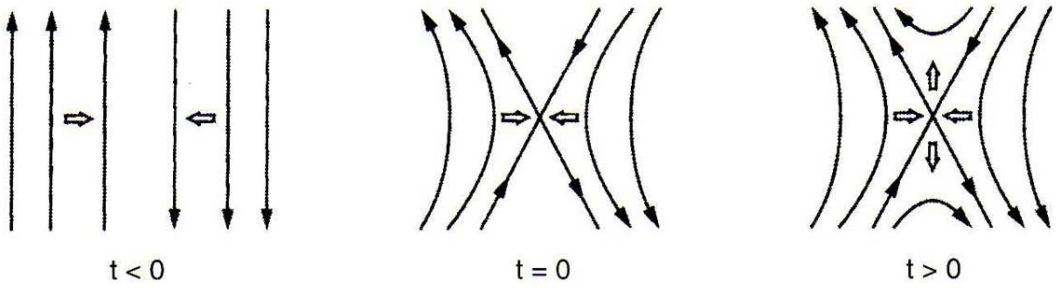

Figure 1.2: A diagram illustrating the topological changes in magnetic field that occur during reconnection. The long lines are magnetic field lines, the short arrows indicate plasma flow. At t<0 (left), the field lines have not yet reconnected but are advecting towards each other. At t=0 (center), field lines begin to diffuse across the two plasma populations. At t>0 (right), plasma is accelerated away from the null point, carrying newly reconnected lines with it. (Gombosi, 1998).

The rate of this reconnection is defined as the inflow velocity of plasma into the merging region and can be expressed several ways. Sweet (1958) and Parker (1957) were the first to quantify this rate for steady state reconnection; their result is seen in Equation 1.7, where v_A is the Alfvén wave speed (Equation 1.8), and S is the Lundquist number (Equation 1.9). The Alvén speed is dependent on the mass density of the plasma (ρ) and the strength of the field (B); it is the speed at which electromagnetic information travels through the magnetosphere. The Lundquist number, or the ratio between the time scales of resistive diffusion and the Alfvén wave speed, is dependent on the length of the reconnection zone (L) as well as the resistivity (η). The Lundquist number is typically very large for space plasma applications, resulting in a reconnection rate that is too slow to account for short timescale events in the Earth's magnetosphere. To overcome this, Petschek (1964) re-derived the reconnection rate

that took into account slow, standing shocks radiating from the reconnection zone. The result, seen in Equation 1.10, is now inversely proportional to the natural log of the Lundquist number, increasing the rate by several orders of magnitude. This expression grows increasingly complex as more factors are taken into account (e.g., Sonnerup (1974); Borovsky and Hesse (2007); Cassak and Shay (2007)). As will be seen, these rates are of great significance to solar wind-magnetosphere coupling.

$$v_{in} = \frac{v_A}{S^{1/2}} \tag{1.7}$$

$$v_A = \frac{B}{\sqrt{\mu_0 \rho}} \tag{1.8}$$

$$S = \mu_0 L v_A / \eta \tag{1.9}$$

$$V_{in} = \frac{v_A \pi}{8 ln(S)} \tag{1.10}$$

Reconnection between the IMF and the terrestrial magnetosphere at the subsolar point arises when the IMF is southward oriented or, equivalently, parallel to the terrestrial dipole axis (Figure 1.3, lines labeled 1). This reconnection combines a purely IMF field line with a purely terrestrial field line (or a "closed" field line as each end is connected to the Earth) to create an "open" field line, which is closed to the Earth at one end but travels far into the solar wind at the other. These newly open field lines are still flowing with the solar wind far away from the Earth, so they are convected over the polar caps toward the night side of the the magnetosphere (Figure 1.3, lines 2, 3, and 4). The motion of the field lines is mirrored at their ionospheric footprints, as seen in the lower-right of Figure 1.3

There are two immediate consequences of the dayside reconnection. First, magnetic flux is eroded from the dayside magnetosphere, changing the location of the

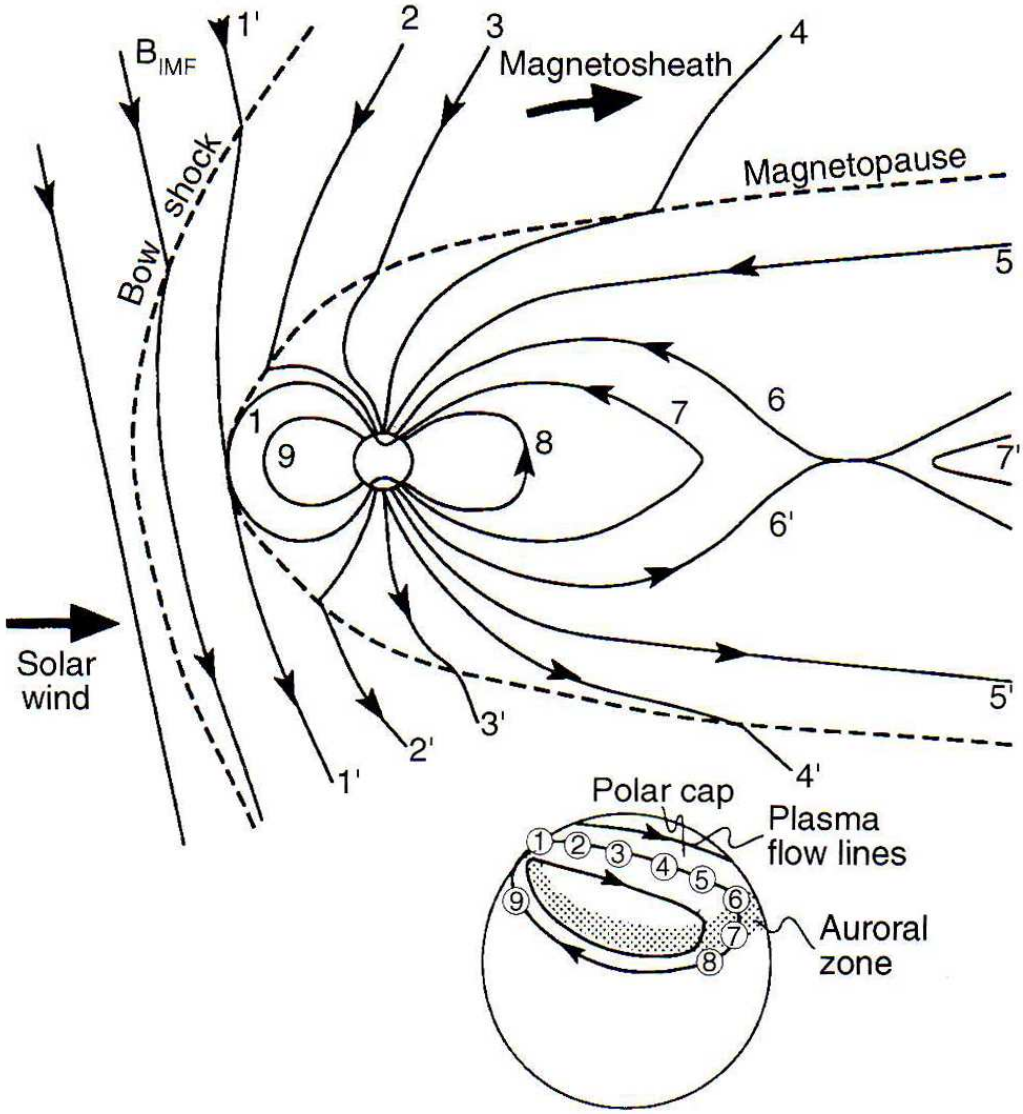

Figure 1.3: A diagram of the Dungey (1963) model for magnetospheric convection. The numbers show how field lines progress through the convection pattern as time advances. Motion of the lines is mirrored in the ionosphere, as is seen in the lower-right hand side. This process opens the magnetosphere up to the motional electric field of the solar wind, which maps down to the ionosphere. (Hughes, 1995).

dayside magnetopause. Secondly, the magnetosphere is now open to the motional electric field of the solar wind as experienced in the Earth's reference frame (Equation 1.6). Because the field lines act as equipotentials (Gombosi, 1998), this potential maps down to the ionosphere, where plasma electromagnetically drifts with the convecting field line footprints. The relationship between this cross polar cap potential drop and the solar wind has been thoroughly investigated (Reiff et al., 1981; Hones, 1984; Kamide and Slavin, 1986; Goertz et al., 1993); it has been linked to solar wind Mach number and reconnection rate (e.g. Siscoe et al. (2002); Ridley (2005)).

Figure 1.4 shows polar cap potential information during a period of southward IMF driving. The two-cell pattern is a typical signature of Dungey-type magnetic convection. The equipotential lines indicate plasma streamlines as field line footprints move first anti-sunward across the polar cap, then return to the dayside at lower latitudes.

As magnetic flux builds on the night side of the magnetosphere, lines are pressed together down tail (Figure 1.3, lines 4 and 5). Because these lines are antiparallel, a second reconnection point forms (Figure 1.3, lines 6). This results in a purely IMF field line that may flow downstream to be reunited with the solar wind and new closed field lines that snap Earthwards in response to the magnetic tension force (Figure 1.3, line 7). These field lines finally advect around the inner magnetosphere to replenish dayside flux (Figure 1.3, lines 8 and 9).

While it is questionable whether or not the dayside and night side reconnection rates can remain balanced (e.g., Kivelson and Spence (1988); DeJong and Clauer (2005)), the effects of unbalanced rates are frequently observed. When the night side cannot return magnetic flux as fast as dayside reconnection can provide it, flux builds up in the tail (Figure 1.5, frame A). As magnetic pressure builds in the tail, a

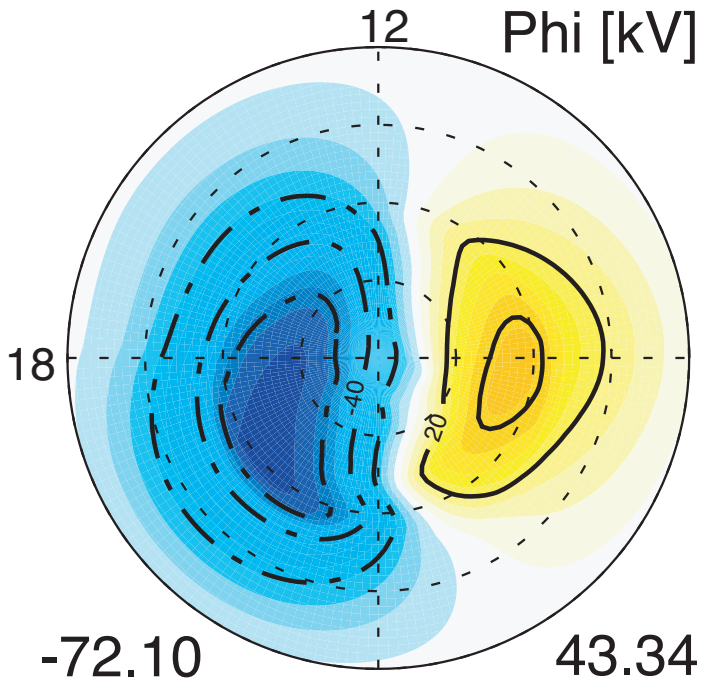

Figure 1.4: The two-cell convection electric field in the northern ionosphere resulting from the motional electric field of the solar wind penetrating the magnetosphere. Local noon is on the top of the plot, local dawn (dusk) on the left(right). The color contours, outlined by the thick, solid and dashed contour lines, show potential strength in kilovolts; blue is negative while yellow is positive. Minimum and maximum voltage values are shown to the left and right of the plot. This plot is the result of coupled MHD and ionospheric electrodynamics numeric modeling, as described in Chapter III.

new, near-Earth neutral line forms and quickly reconnects tail field lines (Figure 1.5, frame B). The mechanism responsible for beginning this process is still under dispute. As the last closed line is reconnected, the tail snaps towards the Earth, making the field topology more dipolar. This is often referred to as a "dipolarization" of the magnetosphere. The circular, self connected field lines are no longer restrained by the magnetosphere. This "plasmoid" is free to eject down tail (Figure 1.5, frame B). These events are known as "substorms" (Akasofu, 1964; McPherron, 1973; Russell and McPherron, 1973; Rostoker et al., 1980; Baker et al., 1997), and are an interesting and important dynamic in the magnetosphere.

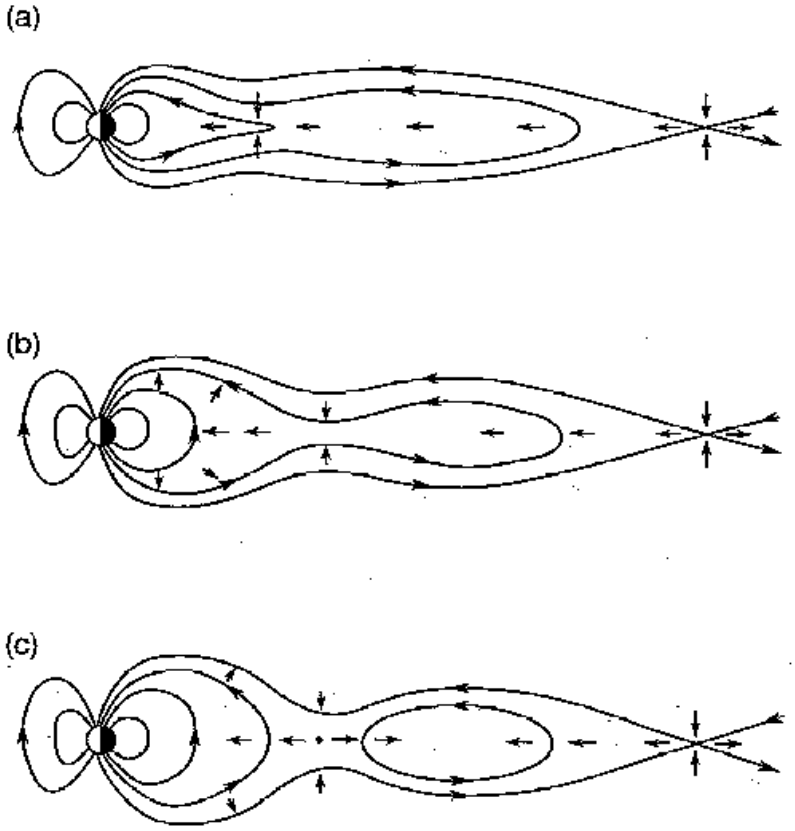

Figure 1.5: A basic diagram of a magnetospheric substorm. In frame (a), unbalanced reconnection builds up magnetic flux in the tail. In (b), rapid reconnection develops at a near-Earth neutral line, resulting in (c) plasmoid formation and dipolarization of the magnetosphere. Cowley (1996).

The description of the Dungey model of magnetospheric convection thus far has fo-

cused on southward IMF orientations. Such driving has been observed (e.g. Coleman et al. (2001); Sandholt and Farrugia (2003)) and examined (e.g. Friis-Christensen and Wilhjelm (1975); Luhmann et al. (1984); Cowley et al. (1991)) for other orientations as well. Different orientations result in very different ionospheric potential patterns and plasma flow patterns.

The case for northward IMF was explored in detail by Song and Russell (1992). For this scenario, field lines are antiparallel not at the subsolar point, but at two high latitude locations: one above the north pole and one below the south. This reconnection adds a solar wind field line to the dayside magnetosphere rather than erode the flux away. The new flux tube then "sinks" into the magnetosphere, bringing solar wind plasma with it. Through the interchange instability (Gold, 1959; Ö. Sonnerup and Laird, 1963), the field lines are pulled azimuthally around the magnetosphere, forming the low-latitude boundary layer. Energy from the highlatitude reconnection is converted to thermal energy as the field line is shortened, then converted to kinetic energy through the instability.

As Dungey (1961, 1963) was proposing the preceding theory for energy transfer to the magnetosphere, Axford and Hines (1961) were developing an alternate method. Rather than rely on magnetic reconnection, Axford and Hines (1961) suggested that viscous interactions between the solar wind and the flank magnetospheric plasma could result in the transfer of momentum across the boundary. Flank plasma is then drawn to the night side, where an increase in pressure would force a return flow (Figure 1.6). This flow would pull magnetic field lines with it, imposing a dawn-dusk motional electric field (Equation 1.6) that maps to the ionosphere in the same fashion as Dungey (1963), again seen in Figure 1.4.

The Axford & Hines viscous interaction model for magnetospheric convection has

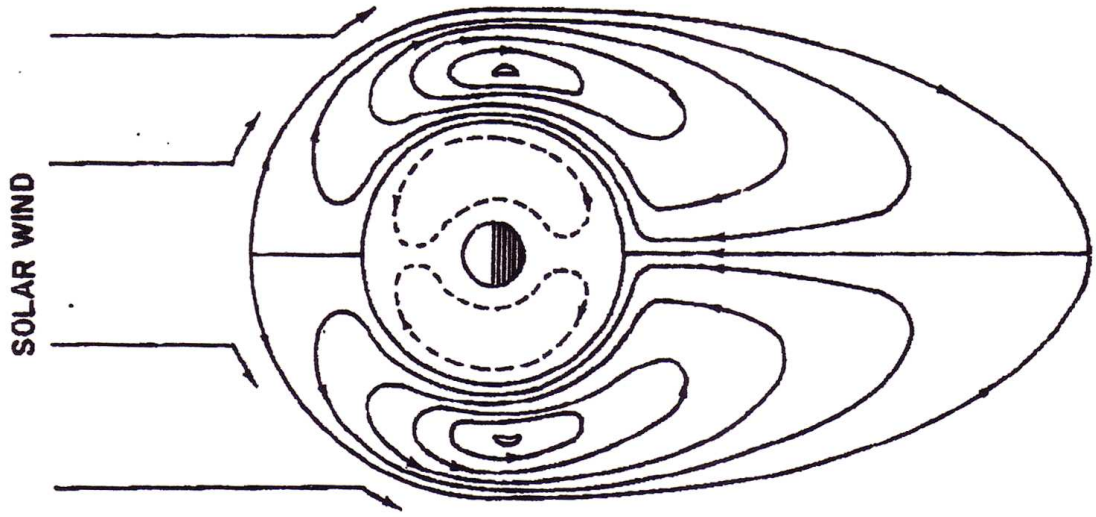

Figure 1.6: A diagram of the magnetospheric flows caused by viscous interactions between solar wind and flank magnetosphere plasma. The slice is in the magnetic equatorial plane with the Sun to the far left of the figure. Axford and Hines (1961).

some interesting distinctions from its Dungey counterpart. Axford & Hines type driving only produces a single convection pattern, as opposed to the Dungey model which yields different patterns for different reconnection configurations. Because the solar wind is always blowing, viscous driving does not "turn off" as reconnection driven driving can when the IMF changes orientation. It has been shown that this type of driving yields a consistent background cross polar cap potential of 35kV (Reiff et al., 1981), and viscous interactions are considered to account for 10-20% of the energy transferred from the solar wind to the magnetosphere (Hughes, 1995).

A final note concerning this mode of driving: the original work by Axford and Hines (1961) did not suggest a specific mechanism to account for the viscous interactions. Observational support for the existence of a viscous mechanism of momentum transfer was published early by Sonett (1960). A popular, contemporary candidate is the Kelvin-Helmholtz instability (Sckopke et al., 1981), with recent observational (Fairfield et al., 2000) and modeling (Damiano et al., 2008) results yielding new evi-

dence. Axford and Hines (1961) were careful to note that the exact process was not important, just that such an interaction exists.

1.4 Sources of Magnetospheric Plasma

Given the above descriptions of solar wind-magnetosphere coupling, the most obvious plasma source for the magnetosphere is the solar wind itself. Following Dungey (1961), reconnection in the tail accelerates plasma tied to the field lines into the plasma sheet and inner magnetosphere. It has been argued that this is the primary source of sheet and ring current particles (Eastman et al., 1985; Kivelson and Spence, 1988; Lennartsson, 2001), and recent modeling efforts provide support for this (Winglee, 2003; Moore et al., 2005). Alternatively, flank interactions, as postulated by Axford and Hines (1961), allows mixing of the two populations, drawing in fresh solar wind particles into the sheet and inner magnetosphere. This method has observational (Eastman et al., 1985) and numerical (Damiano et al., 2008) support as well.

Another source is the Earth's ionosphere. The predominate escape mechanism is the polar wind, first proposed by Axford (1968) and Banks and Holzer (1968). This process begins with the escape of electrons, setting up an ambipolar electric field between them and the major ionospheric ion, O^+, and the minor species, H^+ and He^+. The field accelerates the ion species, but the massive oxygen is not accelerated as quickly as the smaller ions, thus preserving the ambipolar field. A situation arises that is analogous to the solar wind acceleration, and the light ions reach supersonic outflow speeds. This flow is augmented by bulk auroral upflow of particles that are heated, likely through frictional heating (Heelis et al., 1993; Wilson, 1994), whose source is lower in altitude that the polar wind (Loranc et al., 1991; Wahlund et al.,

1992).

There exists non-polar wind processes that draw out significant, more energetic oxygen as well (Abe et al., 1993; Ganguli, 1996; Yau and André, 1997; Andre and Yau, 1997). The resulting flows are known as ion beams, ion conics, and upwelling ions. The names derive from the pitch angle distribution of the populations, and the distinctions are not sharp (Andre and Yau, 1997). The exact mechanisms driving these flows is not well understood. Vertical accerlation is believed to be a combination of parallel electric fields (Klumpar et al., 1984) and ion heating over an extended altitude (Temerin, 1986). Perpendicular energization, which creates ion conics, is believed to be driven by wave-particle interactions (Chang and Coppi, 1981; Borovsky, 1984; Hultqvist, 1991), especially resonance with waves of frequency on the order of the gyro frequency (Ashour-Abdalla and Okuda, 1984; Chang et al., 1986).

While it is well accepted that the ionosphere is the main source of the plasmasphere population (Horwitz and Singh, 1991), its contribution to the plasma sheet and ring current has been a long standing question. Large fluxes of O^+ are observed during geomagnetic storms (Shelley et al., 1972; Lennartsson and Shelley, 1986; Nosé et al., 2003; Denton et al., 2005), indicating ionospheric plasma origins. Furthermore, it has been argued that ionosphere sources could account for nearly all of the magnetosphere plasma (Chappell et al., 1987, 2000; Huddleston et al., 2005). Simultaneously, detections of He^{++} (Lennartsson, 2001) imply plasma from solar wind origins. The strength of each source and the exact mechanism remains unsolved. Accurate knowledge of magnetospheric plasma sources is vital for accurate modeling and understanding of the coupled ionosphere-magnetosphere system.

1.5 Motivation of This Work

The magnetosphere acts as a giant, self-perpetuating, natural plasma laboratory. Studying this region yields insight into how charged particles behave in complex electromagnetic fields. This expands the scientific community's knowledge of processes such as magnetic reconnection, wave-particle interactions, and ion-neutral interactions. This understanding is relevant to other fields that study plasma mechanics, such as fusion physics.

Just as tropospheric weather plays an important role in everyday life, the interaction between the space environment and human technological systems has given rise to the notion of "space weather." Ionospheric currents can couple into long, ground-based conductors, damaging electrical lines and stations and dangerously heating oil pipelines. Communication satellites are vulnerable to signal scintillation, electrical charging, and increased atmospheric drag- all driven by magnetospheric processes. Even commercial airlines face new risks as crews and passengers are exposed to radiation during transpolar flights. Table 1.2 summarizes the averaged annualized losses of these and other industries due to space weather. These losses continue to grow as reliance on technological systems, as well as their sensitivity to the space environment, continues to grow.

Sector	Annual Space Weather Loss
Commercial and Government Satellite Operations	\$700 Million
Electric and Oil Utilities	\$150 Million
Commercial Airlines	\$200 Million

Table 1.2: Average annual losses due to space weather on several industries. Compiled from Horne (2001).

The operational aspect of this area of research gives it practical significance that is far more direct than many other scientific focuses. Dependence on space-borne intelligence systems makes space weather a topic of national security. This drives

demand for advances in this subject by government agencies such as the Department of Defense. There is also a latent commercial need, as airline, utility, and spacecraft operators struggle to control space weather driven losses.

This need provides strong motivation for research in heliospheric and magnetospheric space sciences. Mitigation techniques require a full understanding of the space environment as well as robust, accurate computer models capable of predicting these effects well before they happen. Current capabilities lie in "now-casting" of simple indexes and are inadequate for government and commercial needs (Horne, 2001). Much work stands to be done to create system-specific forecasting that predicts the full effects of space weather storms.

1.6 Goals of This Study

The first goal of this work is to further study the link between space weather and human technological systems by demonstrating the link between long-term exposure to space weather hazards and satellite problems. There is a growing body of work that demonstrates the connection between anomalous behavior aboard communication satellites and tumultuous space weather conditions at the time of the anomaly. However, these studies neglect the total effect that space weather has had on these spacecraft leading up to the issue. For the first time, lifetime exposure is linked to the onset of satellite anomalies.

With numerical models becoming increasingly important to the scientific and operational communities, it is important to fully understand the capabilities of the models that are in use today. The second goal of this work is to validate the Space Weather Modeling Framework (SWMF) against in-situ measurements of the magnetic field and plasma properties at geosynchronous locations. This validation work

is the first extensive investigation of the SWMF's abilities to predict these values. Different combinations of modules are used within the framework to fully explore the effect that different physics capabilities have on the results.

The third and final goal is to use the validated system to examine the problem of the dominate source of plasma for the magnetosphere. This is executed by using the multispecies version of the BATS-R-US magnetohydrodynamics (MHD) code to follow the destination of ionospheric and solar wind origin plasma. Different ionospheric outflows and solar wind conditions are tested. The results are then verified using data-model comparisons of real-life simulations. This is the first exploration of the outstanding plasma source problem using multispecies MHD.

CHAPTER II

The Long Term Effects of Space Weather

2.1 Introduction

Anomalous satellite behavior can disrupt spacecraft operation, negatively affecting all who rely on space borne assets- from operators and service providers to consumers. While there are many causes of these problems, such as software glitches or hardware failure, many can be induced by the effects of the space environment (Baker, 2000a; Feynman and Gabriel, 2000; Koons et al., 1999; Pirjola et al., 2005a). Satellite engineers and operators work diligently to prevent the occurrence of spacecraft anomalies, but space weather introduces an uncontrollable, hard to predict variable into the system.

There is a growing body of work that correlates the occurrence of these anomalies with space weather conditions. Krause et al. (2000) found significant correlations between the geomagnetic activity indices Kp and Dst and observed surface charging values from the Defense Satellite and Communication System III spacecraft. Fennell et al. (2001) found similar correlations between these indices and the SCATHA (Spacecraft Charging AT High Altitudes) satellite, noting that surface charging events correlated to substorm activity while internal charging events corresponded to geomagnetic storm events. Wilkinson et al. (1991) showed that

single event upset (SEU) anomalies recorded by the TDRS-1 (Tracking and Data Relay Satellite) were associated with increases in galactic cosmic ray and high energy proton fluxes. Both Iucci et al. (2005) and Pilipenko et al. (2006) used the National Oceanic and Atmospheric Administration's (NOAA) National Geophysical Data Center's (NGDC) spacecraft anomaly database to show that on days when there was an increase in anomalies, there was a corresponding increase in in-situ particle flux measurements and/or geomagnetic indices. While all of these studies illustrate the connection between space weather conditions at the time of the anomaly and the spacecraft disruption itself, they all neglect the long term effects of the background radiation environment.

Energy deposited onto the spacecraft from high energy particles and electromagnetic radiation has the ability to break down and rearrange atomic bonds of spacecraft materials, from paints and coatings to electronic insulators, dielectrics and circuitry components. These total dose effects are described by Scarpulla and Yarbrough (2003, and references therein). Over time, coatings become less reflective and electronics change their characteristics and this may cause the satellite to become more likely to experience an operational anomaly. Investigating solar and magnetospheric activity during or near the epoch of the anomaly will not uncover correlations between space weather and anomalies driven by long term radiation damage.

Total dose damage and its effects present a special problem for satellite operators and the space research community. Without the proper instrumentation on board, it is difficult to know how much particle radiation exposure a particular satellite has experienced (described as a satellite's "radiation life" by Gubby and Evans (2002).) While investigations of radiation hardening are performed on individual spacecraft

components (e.g. Malou et al. (2002); Wajima et al. (2007)), this is not the case for the system as a whole. Additionally, total exposure effects are often confused with normal satellite aging due to insufficient diagnostics (Dyer, 2002). These complications have made understanding the full importance of these effects especially challenging. This study explores the relationship between long-term radiation exposure and spacecraft operational anomalies by investigating the total life time high energy particle exposure experienced by a spacecraft at the time an anomaly occurred.

2.2 Procedure

Geostationary Operational Environmental Satellites (GOES) energetic particle flux data was collected from 1974 to 1994. This data consists of an integral measurement of $\geq$2 MeV electrons and a seven channel differential measurement of protons, all recorded by the Energetic Particle Sensor (EPS) instrument aboard the Space Environment Monitor (SEM) subsystem. A list of the proton energy channels is displayed in the first column of Table 2.1. This data was time-integrated to yield total particle exposure per day. For days where there was more than one GOES satellite present, the multiple measurements were averaged together to create values that better reflect conditions at all geosynchronous locations. These averaged daily particle exposure values were used to investigate satellite anomalies that were reported to the NOAA NGDC spacecraft anomaly database (described in Wilkinson (1989)).

The anomaly database was refined to fit the confines of this study. First, any anomaly for which the launch date of the satellite could not be found was discarded. Launch dates were unattainable for satellites whose real name was not used in the database. Anomaly events that occurred on satellites that were launched before July, 1974 were also discarded, because a lifetime exposure could not be calculated using

Particle Channel	Mean	% > 2
≥2 MeV Electrons	1.445	33.7%
0.8 to 4 MeV Protons	0.616	< 0.5%
4 to 9 MeV Protons	0.822	1.1%
9 to 15 MeV Protons	0.871	1.0%
15 to 40 MeV Protons	1.092	10.8%
40 to 80 MeV Protons	1.543	35.2%
80 to 165 MeV Protons	0.366	< 0.5%
110 to 500 MeV Protons	0.531	0.6%

Table 2.1: Analysis of perceived to actual age ratios. The left column lists the eight GOES EPS particle/energy channels used in this study. The center column lists the average ratio of perceived age to chronological age for all 1609 anomaly events. The rightmost column lists the percent of the events whose age ratio exceeded two.

the GOES data. Finally, only anomalies from satellites in geosynchronous orbits were used in order to match the orbit type of the GOES measurements. This reduced the anomaly database to 1609 events from 4996 total.

The NGDC database can be perceived as being limited in scope because anomalies reported to the database managers were, at least initially, thought to be caused by the space environment. However, events were reported on a voluntary basis, often before a formal investigation and without a follow up to improve database accuracy. Additionally, 51% of all anomalies reported to this database are catagorized as having an unknown diagnosis (21% are diagnosed as surface charging events, 16% single event upsets, and 9% internal charging, 3% other). Figure 2.1 shows the distribution of the Kp indexes recorded at the time of each spacecraft anomaly. Of all the events reported, only 15% occurred when the Kp index was 5^- or greater (disturbed magnetospheric conditions or stormier.) Apart from the selection criteria described above, no bias towards anomaly type or diagnosis was shown in this study.

For each anomaly, the lifetime energetic particle exposure was calculated by summing all daily values from the beginning of the satellite's life to the date the anomaly occurred. This value was normalized by dividing by the average particle exposure per year (calculated over two solar cycles). The "exposure-years" experienced by a

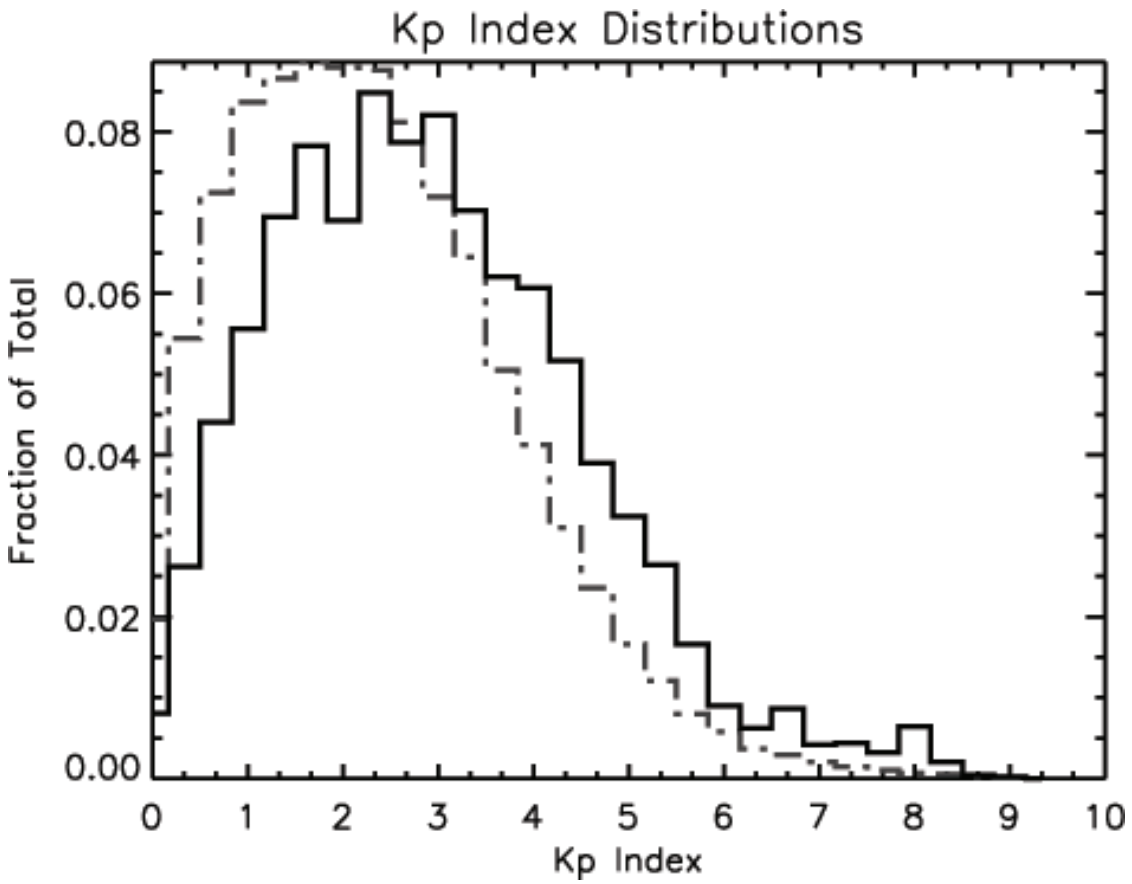

Figure 2.1: Distribution of Kp index values corresponding to NGDC database anomaly epochs (solid line) and the distribution of all Kp values over the temporal span of the database (1963 to 1994). Although there is a clear shift between the two distributions, only 15% of all anomalies in the database occured during disturbed or stormier (greater than 5^- Kp) conditions.

satellite at the time of the anomaly was compared to the chronological age of the satellite. This process was repeated for all eight particle channels listed in Table 2.1.

By converting the units of particle exposure to units of time ("exposure-years"), a number is created that reveals how many years worth of typical particle exposure a satellite has experienced. This number, the satellite's "perceived age," can be much different than a satellite's actual age. In addition, the perceived age based on ring current electrons will be different than the perceived age based on galactic cosmic ray protons because of the different processes that govern the separate particle populations.

A useful analogy for understanding this unit is miles on a car. The transmission may fail when the car is only five years old chronologically, but the car perceives that it is ten years old because it has been driven for as many miles as a typical ten year old car (in other words, ten "mile-years"). While miles on a car represents wear and tear from use of the car, the perceived age of a satellite in this study represents wear-and-tear from the effects of particle exposure. It is an approximation of the radiation life referred to by Gubby and Evans (2002).

2.3 Results

The top frame of Figure 2.2 shows the distribution of satellite chronological age at the epoch of an operational anomaly. Just over 30% of anomalies occur when the satellite is one year old or less. The distribution drops off quickly, with barely 5% occurring on satellites that are greater than ten years old.

In the second frame of Figure 2.2, the distribution of satellite perceived age based on total 4 to 9 MeV proton exposure at the epoch of an operational anomaly is displayed. Most anomalies occurred on satellites that had only experienced less than

two typical years worth of particle exposure for this energy channel. Because of its similarities to the distribution of the chronological ages, this data demonstrates that 4 to 9 MeV protons have little effect on a satellite's susceptibility to anomalies throughout the satellite's life.

For higher energy proton exposure (40 to 80 MeV), the distribution changes dramatically (Figure 2.2, third frame from the top). More satellites have a higher perceived age when an anomaly occurs. Comparing this to the actual age distribution shows that a portion of the anomalies happened on satellites that received a lifetime particle exposure that is disproportionate to that satellite's age. These satellites are wearing down faster than they are aging. This pattern is greatly exacerbated when perceived ages are calculated using the $\geq$ 2 MeV electron channel (Figure 2.2, bottom frame). While only a handful of anomalies occurred on satellites that were $\geq$5 years old, many anomalies occurred on satellites whose perceived age is $\geq$5 exposure years.

For each satellite anomaly, the perceived age for each particle channel is divided by the age of the satellite. This number indicates how much more or less particle exposure a satellite has received compared to its actual age, or how much faster (or slower) a satellite is wearing down due to high energy particle exposure than it is chronologically aging. This value allows for a quantifiable investigation of the data.

Table 2.1 shows a summary of this analysis. The center column shows the mean perceived to chronological age ratio for each particle channel used in this study. This ratio is less than one for lower energy proton channels, but larger than one for the electron, 15 to 40 MeV proton and 40 to 80 MeV proton channels. The rightmost column lists the fraction of events that occurred on satellites that received more than two times the expected total exposure given their chronological age (age ratio of two

or greater.) The ≥2 MeV electron, 15 to 40 MeV and 40 to 80 MeV proton channels stand out again with values of 33.7%, 10.8% and 35.2%, respectively.

Further analysis is performed by considering only the maximum perceived age of the eight channels for each anomaly. The resulting distribution is presented in the top frame of Figure 2.3. 73.5% of all anomalies occurred on satellites that are wearing down more than twice as fast as they are chronologically aging due to one of the eight particle populations measured. This distribution may be skewed by anomalies that occurred on very young satellites. It is unlikely that these early anomalies are the result of integrated particle damage. The second frame of Figure 2.3 includes only events from satellites that were one year old or older when the anomaly occurred. The number of satellites that are wearing down twice as fast as they are aging increases to 78%. For anomalies that occurred on older (five years or greater, bottom frame of Figure 2.3) satellites, this number drops to 50.5%.

2.4 Discussion

Of the anomalies investigated, the majority occur on satellites that have received a lifetime particle exposure that is disproportionate to that satellite's chronological age, with ≥2MeV electrons and 40 to 80 MeV protons showing the greatest disparity. These results show that the historical conditions leading to most anomalies are congruous for making satellites more anomaly prone. This pattern becomes less prevalent in older (five years or greater) satellites, as seen in Figure 2.3. Gubby and Evans (2002) found that sensitivity to space weather on the Anik E2 satellite decreased with time in orbit, and they speculated that one cause of this may be integrated radiation effects. The results shown in the bottom frame of Figure 2.3 support this hypothesis, but there are too few events that fall into this age bracket

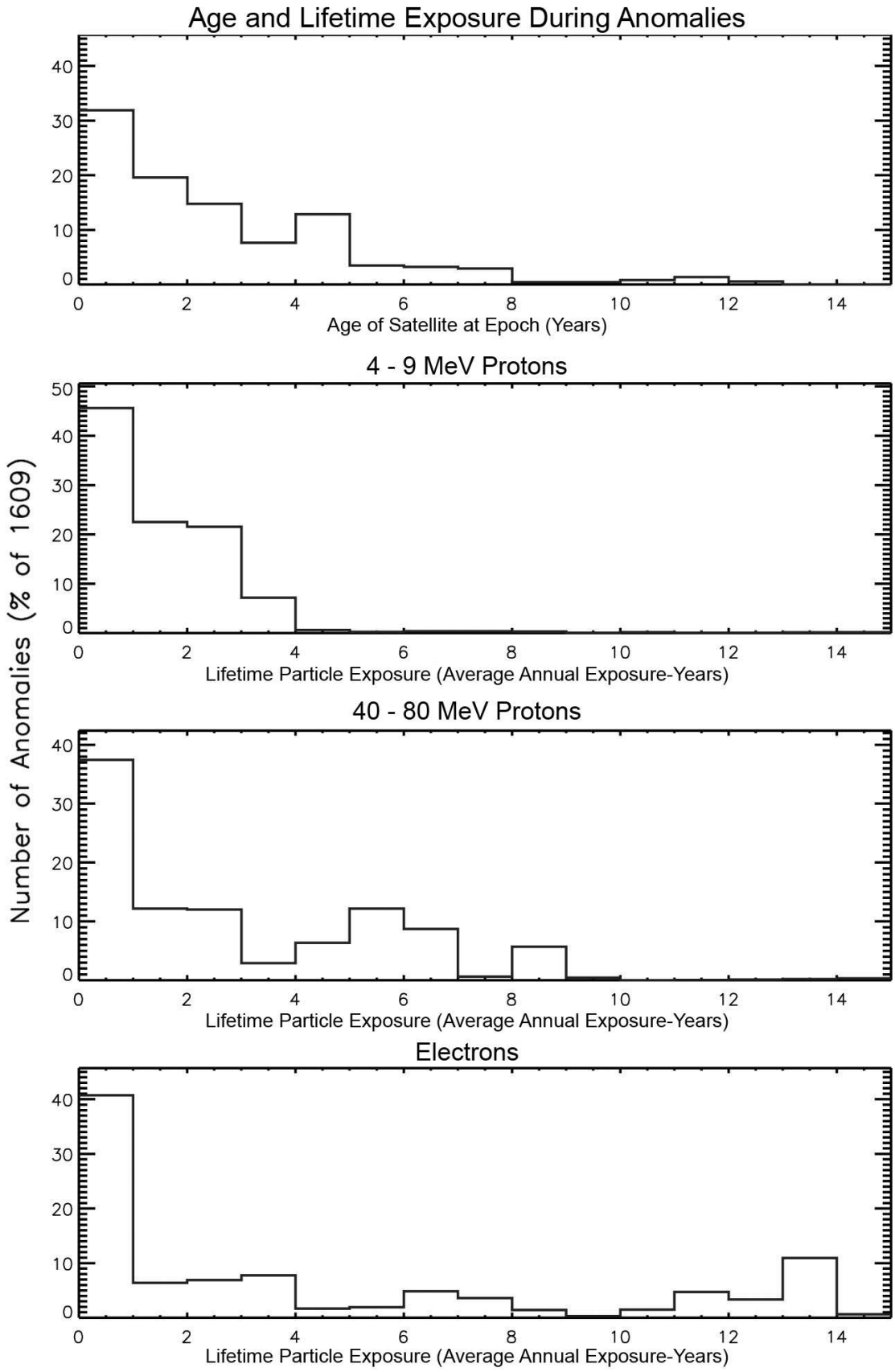

Figure 2.2: Distribution of satellite age when an operational anomaly occured (top frame), perceived age calculated from 4-9 MeV protons (2nd frame from top), perceived age calculated from 40-80 MeV protons (3rd frame from top), and perceived age calculated from ≥ 2 MeV electrons (bottom frame).

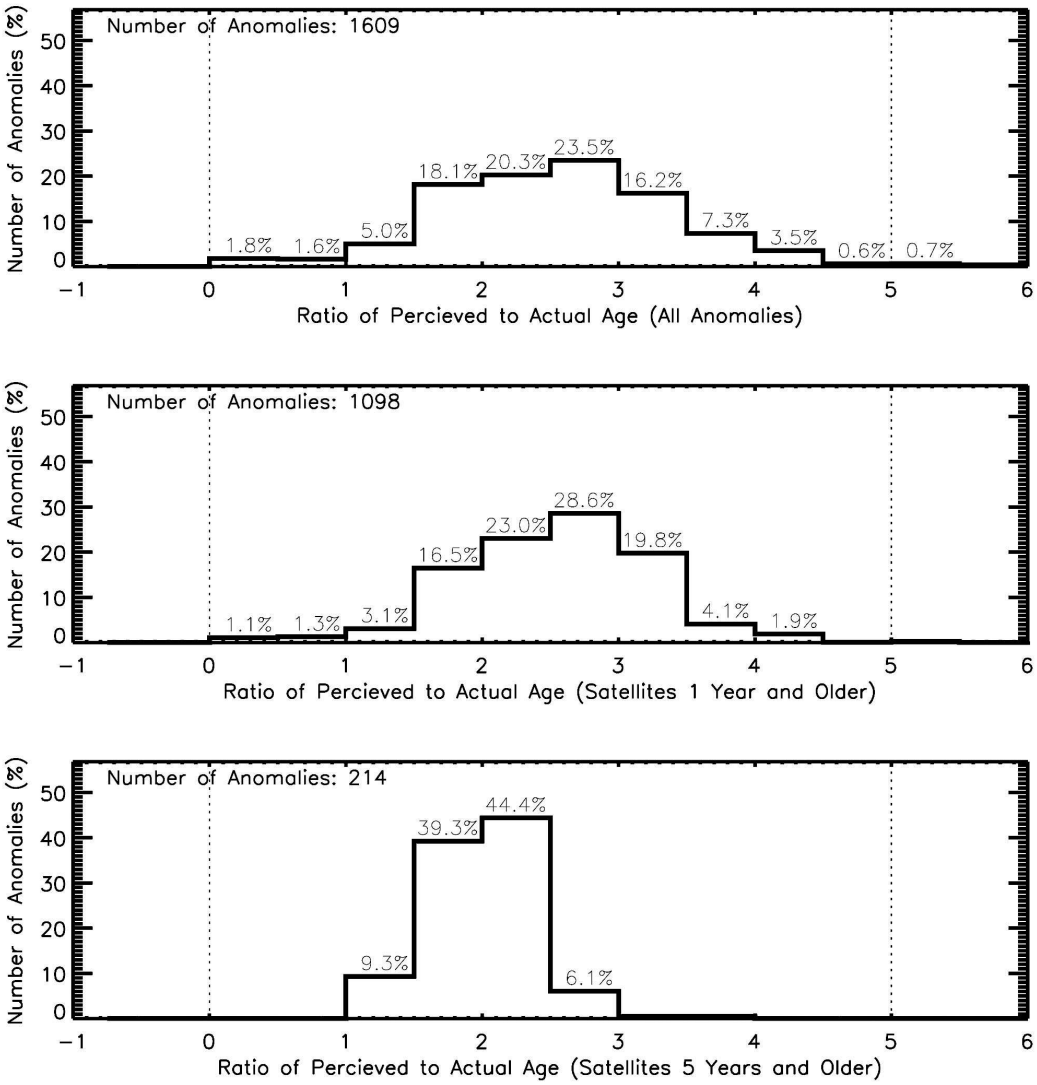

Figure 2.3: Distributions of the greatest ratio of perceived age to chronological age. The top frame includes all anomaly events, while the middle frame includes only events where the satellite was one year old or older at the time the event occured, and the bottom frame includes only satelites that were 5 years old and older.

(n=214) to draw a solid conclusion.

Interpretation of the GOES electron results in the bottom panel of Figure 2.2 is not straightforward because the EPS electron detector responds significantly to >32 MeV protons. Hence, during periods of increased proton flux, this data becomes polluted. For this reason, the electron results represent the total impact of electrons and protons combined. Isolating the impact of the electrons alone may require another data set.

There are several limitations that, if properly addressed, could enhance the completeness of this study:

1. Environmental data localized to the spacecraft that experienced the anomaly could be increased. By reducing the flux measurements to a single average value, any spatial variation is lost. The nominal situation would be to have a particle detector on every spacecraft, but this is not feasible.

2. The limitations of the scope of the NGDC anomaly database, as described earlier, is also an issue. It remains unknown if this database is an accurate representation of all anomalous satellite behavior. Recurring problems on a single satellite may or may have not been consistently reported, depending on the operator. Obtaining additional events is extremely difficult, however, due to the commercial impacts releasing such data would have on operators (Koons et al., 1999).

3. Other variables, such as micrometeroid and ultraviolet radiation exposure, can play a significant role in satellite performance. These factors were not taken into account in this study, and may be difficult to properly account for.

Another issue of this study is potential skewing of the results caused by the natural

seasonality of space weather. Energetic electron fluxes in the magnetosphere are raised during solar minimum periods (Miyoshi et al., 2004); for proton flux variations this pattern is in phase with the solar cycle (Simunac and Armstrong, 2004). Such seasonality may artificially inflate perceived ages calculated here depending on the date of the anomaly. This is especially problematic if there is a similar seasonality observed in event occurrence. Fluctuations of time scale smaller than a year should not impact these results, however, especially for the >2 year old satellite results.

To address this, correlation of yearly average perceived ages based on electron and 40 to 80 MeV proton exposure to sunspot number was investigated. Correlation coefficients, designated as 'r', were calculated; a value of r = $\pm$1(0) demonstrates perfect(no) correlation or anti-correlation. Both comparisons yielded poor correlation (r = -0.376 and 0.277, respectively). In the case of ions, the correlation coefficient is nearly half of what is found in Simunac and Armstrong (2004). Furthermore, event occurrence correlates extremely poorly (r = -0.141) to the solar cycle. These results imply that seasonality does not play a strong role in this study. To fully eliminate seasonality as a major contributor, however, a complete anomaly database that spans more than two cycles is required.

Despite these limitations, the evidence here strongly suggests that the long-term effects of the background radiation environment indeed play an important role in the occurrence of spacecraft anomalous behavior. There is a strong correlation between enhanced lifetime high energy particle exposure and anomaly occurrence. The potential to create anomalies during unperturbed periods makes the effects of space weather even more difficult to understand and mitigate. Operators, engineers, and scientists must not neglect a spacecraft's integrated particle exposure when investigating the cause of an anomaly.

While predicting and preventing anomalies caused by total dose effects may be difficult, operators can take steps to monitor a spacecraft's perceived age. In situ particle and electromagnetic radiation measurements can yield lifetime exposure estimates. Assimilative and first principle based simulations can complement these measurements by providing better spatial data. By tracking perceived age information, operators can see how fast their equipment is wearing down and know which satellites are more likely to experience problems.

CHAPTER III

Overview of the SWMF and Numerical Models Used

3.1 The Space Weather Modeling Framework

Numerical modeling of the near-Earth space environment has become a broad and important field. Models range from empirical codes (Papitashvili and Rich, 2002; Tsyganenko, 2002a,b; Weimer, 1996) to large, first principle based systems (Powell et al., 1999; Gombosi et al., 2002; Raeder et al., 2001; Lyon et al., 2004). These codes are invaluable tools for learning about the near-Earth environment. Because space weather conditions can impact communications, ground based utilities, and even airlines (Baker, 2000b; Fey, ????; Horne, 2001; Pirjola et al., 2005b), numerical models of the space environment are becoming equally vital as operational forecast tools as they are scientific tools.

The prototypical approach to modeling the space environment is to focus on a region of interest- whether it be a specific spatial region, a certain physical process, or an explicit particle population. This allows for a detailed investigation of the partition without making the code too resource intensive for simulations to be completed in a timely manner. The downside, however, is that effects from other regimes are marginalized. They are either accounted for by simplistic, unphysical methods or neglected outright. This is issue is especially problematic in the magnetosphere, where

coupling between regions (e.g., the ionosphere and inner magnetosphere) cannot be neglected if accurate results are desired.

To overcome this, the Space Weather Modeling Framework (SWMF) has been developed. The Framework is a flexible system that allows many models of the space environment to be executed concurrently and coupled together easily (Tóth et al., 2005). It accomplishes this by dividing the Sun to upper atmosphere system into 11 physical components or "modules." Each module contains a numerical model whose execution is controlled by the SWMF in order to synchronize the entire system. Coupling between modules through the SWMF is configured to simulate the interactions between the different physical systems. The framework has been used to perform complicated studies of the Sun to Earth system that are easily performed by several coupled models working together (Tóth et al., 2007; Ridley, 2007).

Figure 3.1 displays a simple diagram of the available modules in the SWMF. Each one represents a numerical model implemented into the framework. While the codes currently implemented are first-principle physics codes, simpler systems, such as empirical codes, can be implemented as well. While the system is capable of simulating the space environment from the solar atmosphere to the Earth atmosphere, as few as one module can be used at a time. In the following chapters, all simulations are driven by measurements of the solar wind at the first Lagrangian point. Up to four modules will be used: Global Magnetosphere (GM), Ionosphere Electrodynamics (IE), Inner Magnetosphere (IM), and Polar Wind (PW). The models used and the coupling invoked is described in the following sections.

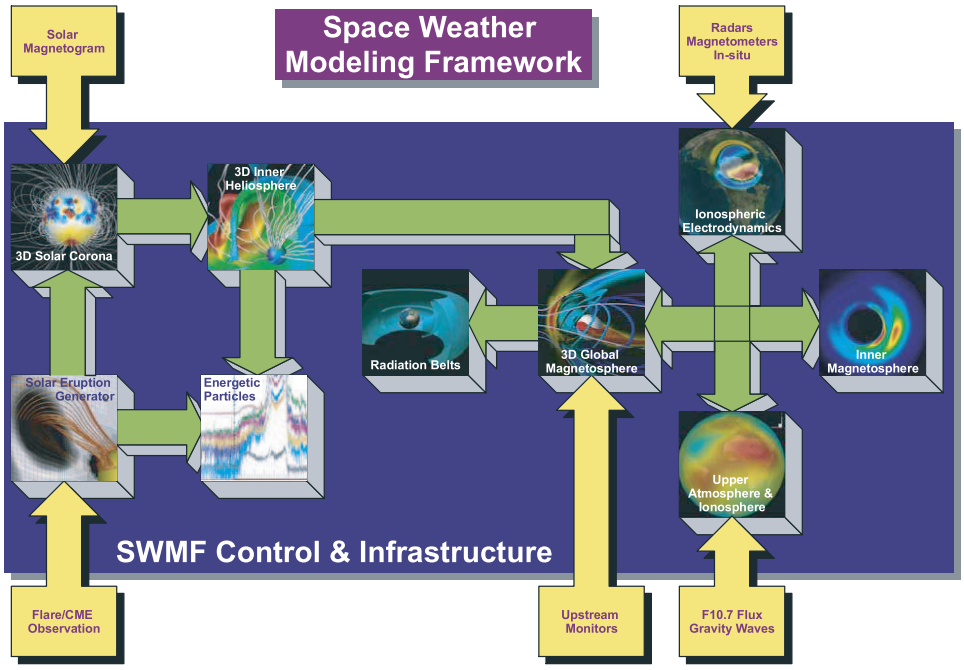

Figure 3.1: The available modules in the SWMF. Arrows indicate couplings between modules. From Tóth et al. (2007).

3.2 Global Magnetosphere

The GM component simulates the magnetosphere from the bowshock to the distant tail. It is responsible for large-scale processes such as the transfer of energy and mass from the solar wind to the magnetosphere and global magnetospheric convection. This component is currently modeled by the Block Adaptive Tree Solar-wind Roe-type Upwind Scheme (BATSRUS) code (Powell et al., 1999; De Zeeuw et al., 2000). This component is the most important of all of the codes used in this dissertation.

BATSRUS solves the magnetohydrodynamic equations (MHD). The theory behind these equations begins with the Euler macroscopic transport equations for a conducting fluid. These equations are combined with the generalized Ohm's law as well as the Maxwell electrodynamic equations. This merging results in the ideal MHD equations (Equations 3.1 to 3.4). The derivation of the MHD equations from

kinetic and electrodynamic theory can be found in many textbooks, including Gombosi (1998).

$$\frac{\partial \rho}{\partial t} + \nabla \cdot (\rho \mathbf{u}) = 0 \tag{3.1}$$

$$\frac{\partial \rho \mathbf{u}}{\partial t} + \nabla \cdot (\rho \mathbf{u}\mathbf{u} - \mathbf{B}\mathbf{B}) + \nabla p_{tot} = 0 \tag{3.2}$$

$$\frac{\partial e}{\partial t} + \nabla \cdot (\mathbf{u} e + \mathbf{u} p_{tot} - \mathbf{B}\mathbf{B} \cdot \mathbf{u}) = 0 \tag{3.3}$$

$$\frac{\partial \mathbf{B}}{\partial t} + \nabla \cdot (\mathbf{u}\mathbf{B} - \mathbf{B}\mathbf{u}) = 0 \tag{3.4}$$

In these equations, the conserved quantities are mass density (ρ), momentum density ($\rho\mathbf{u}$), energy density (e, Equation 3.5) and magnetic field ($\mathbf{B}$). $\mathbf{u}$ is the bulk flow of the plasma, p is the isotropic thermal pressure, and p_{tot} is the thermal plus magnetic pressure (Equation 3.6). Equation 3.4, first introduced in Chapter I, is the induction equation; it ties the motion of the plasma to the motion of the magnetic field lines.

$$e = \frac{p}{\gamma - 1} + \frac{\rho u^2}{2} + \frac{B}{2\mu} \tag{3.5}$$

$$p_{tot} = p + \frac{B^2}{2\mu} \tag{3.6}$$

There are several important assumptions made in the derivation of the ideal MHD equations:

1. The electron-proton plasma is treated as a single fluid.

2. Charge neutrality is assumed.

3. Pressure is isotropic (thermal pressure is treated as a scalar and not a tensor.)

4. Heat flow is neglected.

5. The plasma is perfectly conducting, so resistive terms are discarded ($\eta \to 0$).

Equations 3.1 through 3.4 are expressed in their conservative form, which lends to straight-forward discretization. The generic form is shown in Equation 3.7, where $\mathbf{W}$ is the state vector (variables inside of the time derivative), $\mathbf{F}$ is the flux tensor (terms inside of the divergence), and $\mathbf{Q}$ is the source vector, which is zero for the idealized case as defined above. This equation is solved using the finite-volume approach, where the domain is divided into small volume regions. The governing equations are integrated over a cell, i, as seen in Equation 3.8. The divergence theorem allows the volume integral of the divergence term to be converted into a surface integral, resulting in Equation 3.9. The surface integral can then be evaluated as the sum of the fluxes at the surfaces of the cell using the midpoint rule (Equation 3.10). This method has the beneficial property of automatically conserving the state variables.

$$\frac{\partial \mathbf{W}}{\partial t} + (\nabla \cdot \mathbf{F})^T = \mathbf{Q} \tag{3.7}$$

$$\int_{cell\, i} \frac{\partial \mathbf{W}}{\partial t} dV + \int_{cell\, i} \nabla \cdot \mathbf{F} dV = \int_{cell\, i} \mathbf{Q} dV \tag{3.8}$$

$$\frac{\partial \mathbf{W}_i}{\partial t} + \frac{1}{V_i} \oint_{cell\, i} \mathbf{F} \cdot \hat{\mathbf{n}} dS = \mathbf{Q}_i \tag{3.9}$$

$$\frac{\partial \mathbf{W}_i}{\partial t} + \frac{1}{V_i} \sum_{faces} \mathbf{F} \cdot \hat{\mathbf{n}} dS = \mathbf{Q}_i \tag{3.10}$$

Evaluation of flux at cell interfaces is calculated by a Roe scheme approximate Riemann solver (Powell et al., 1999). Time stepping scheme is an optimally smoothing, multi-stage scheme developed by van Leer et al. (1989). Control of $\nabla \cdot \mathbf{B} = 0$ is performed by keeping $\nabla \cdot \mathbf{B}$ terms in the derivation of the MHD equations, resulting in non-zero source terms. Inclusion of these terms constrains $\nabla \cdot \mathbf{B}$ to truncation-error levels (Powell et al., 1999) and has been shown to improve overall results (Tóth and Odstrčil, 1996).

BATS-R-US uses an adaptive Cartesian, block-based grid (see Berger and Jameson (1985); Berger and Colella (1989); Powell et al. (1999)). The domain is divided up into blocks, and each block contains $n \times n \times n$ cells (in all subsequent chapters, $n = 8$). This block tree structure lends itself naturally to parallelization by distributing blocks to separate processors. It also allows for easy refinement of blocks, either manually or automatically. Blocks flagged for refinement are split into 8 new blocks by dividing the block in half for each dimension. The resulting blocks contain the same number of grid points, but the resolution is halved. Solution-based automatic refinement is possible but not used here.

For simulations of the Earth's magnetosphere, the Geocentric Solar Magnetospheric (GSM) coordinate system is used. In this system, the X axis points radially from the center of the Earth to the Sun. The Z axis points towards the northern hemisphere such that the terrestrial dipole remains in the X-Z plane, and the Y axis points dusk ward, completing the right-handed system. The Earth's dipole is titled away from the rotation axis by 11°, so it rotates around the rotation axis each day. This causes the GSM coordinate system to rock from dawn to dusk and back again

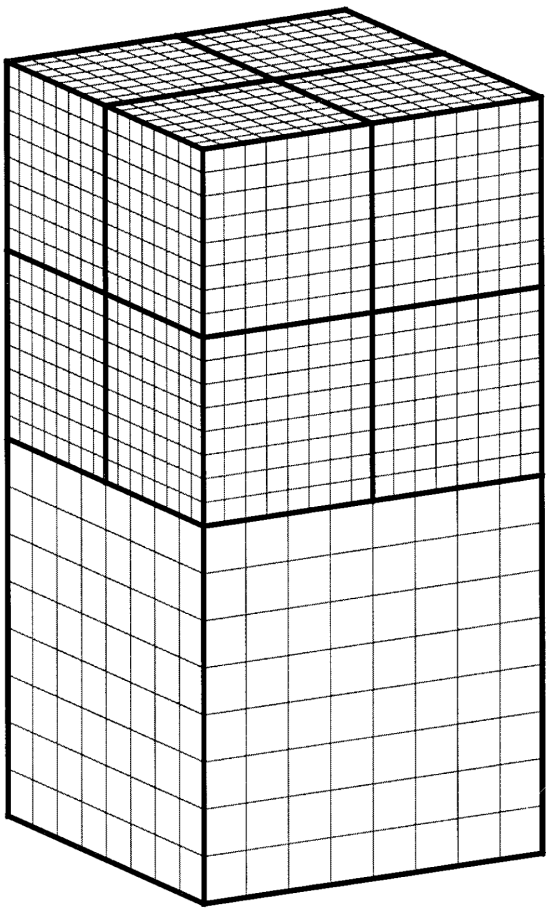

Figure 3.2: Example of the block structure used in BATS-R-US. The dark lines represent the boundary between blocks, the lighter lines represent the boundary between grid cells. Although each block contains the same number of cells, the top blocks would be the result of one refinement of the lower block. From Powell et al. (1999).

over the span of one day.

For simulations in the following chapters, the inner boundary is a sphere of radius 2.5 Earth radii (R_E); the outer boundary is 32 R_E in the upstream direction, 224 R_E downstream, and 128 R_E in each other direction. Observed upstream solar wind conditions (either from the ACE or Wind spacecraft measurements) are imposed as the upstream boundary conditions. The inner boundary number density is set at $28cm^{-3}$.

The GM module (BATS-R-US) couples to each other module used in the subsequent studies. Flux tube volume and ionospheric footprints are handed to the inner magnetosphere (IM) component, and the IM-calculated plasma pressure is returned to nudge the GM solution (De Zeeuw et al., 2004). The ionospheric electrodynamics (IE) component receives field-aligned current strength and position from GM and returns the electric potential (ψ) at the inner boundary of GM. This value is converted to velocity at the inner boundary through the relationship $\mathbf{B} = -\nabla\psi$ and the formula for $\mathbf{E} \times \mathbf{B}$-drift (first term of Equation 1.5). The Polar Wind (PW) module acts as new density and velocity inner boundary conditions for GM when activated

3.3 Ionospheric Electrodynamics

The IE component calculates height integrated ionospheric quantities at an altitude of about 110 km. It currently is handled by the ionosphere electrodynamics solver described in Ridley and Liemohn (2002) and Ridley et al. (2004). This model receives field-aligned currents from the GM component and uses them to calculate particle precipitation and conductance patterns. The conductance and field-aligned currents are used to calculate the electric potential, which is in turn mapped back to the inner boundary of the GM module. The IE module also provides electric

potential to the IM and PW modules through one-way coupling.

The process used by this model to obtain the ionospheric electric potential is the one described by Goodman (1995) and later altered by Amm (1996). This process begins by mapping the field aligned currents, $J_{\parallel}$, from the MHD solution at $R = 3.5R_E$ down to the ionospheric height where the calculation will occur. Because the greater portion of the mapping occurs in the "gap region" between the MHD inner boundary (2.5 R_E) and 110 km, a dipole field configuration is used. The current strength is scaled appropriately using the ratio $B_{ionosphere}/B_{3.5R_E}$. The radial (field-aligned) current at the ionosphere height is used to calculate the electric potential using Equation 3.11, where Σ is the conductance tensor, ψ is the electric potential, and R_I is the radial height where the calculation occurs. The potential is then mapped back to the inner boundary of the GM component, creating an ionospheric feedback system.

$$J_{Radial}(R_I) = [\nabla_{\perp} \cdot (\Sigma \cdot \nabla\psi)_{\perp}]_{R=R_I} \tag{3.11}$$

The conductance tensor includes effects from four sources: solar EUV conductance, night side star light conductance, auroral conductance, and polar cap conductance. All of these and their effects on results are described in detail by Ridley et al. (2004) and are summarized here. Solar illumination is an important ionization and thus conductance source on the dayside. This effect is approximated by taking the $F_{10.7}$ flux (the 10.7cm solar radio flux) as a model input and using the relationships shown in Equations 3.12 and 3.13 (Moen and Brekke, 1993), where Σ_H is the resulting Hall conductance, Σ_P is the Pederson conductance, and ζ is the solar zenith angle.

$$\Sigma_H = F_{10.7}\left(0.81cos(\zeta) + 0.54\sqrt{cos(\zeta)}\right) \tag{3.12}$$

$$\Sigma_P = F_{10.7}\left(0.34cos(\zeta) + 0.93\sqrt{cos(\zeta)}\right) \tag{3.13}$$

Auroral zone conductance is generated by precipitating particles creating ionization in the thermosphere, which in turn collide with neutrals to form Hall and Pederson conductivities (e.g. Frahm et al. (1997), Galand et al. (2001)). Because the MHD code does not include high-energy particles, a first principle formulation of this effect cannot be generated. To account for this effect, auroral zone conductance is set via an empirical relationship based on results from the Assimilative Mapping of Ionospheric Electrodynamics (AMIE) technique (Richmond and Kamide, 1988). This method is described further in Ridley et al. (2004).

Polar cap conductance describes the effects of "polar rain" (Newell and Meng, 1992), which is a uniform precipitation of electrons that produces a small amount of F-region conductance. Processes such as star light irradiance can cause some additional ionization as well. Both of these are included as constant, uniform conductances in this model and are secondary to the other conductance sources.

3.4 Inner Magnetosphere

The Inner Magnetosphere (IM) domain is the region that is characterized by closed magnetic field lines and particles of keV energies. To simulate this region, the Rice Convection Model (RCM) (Harel et al., 1981; Sazykin, 2000; Toffoletto et al., 2003) is used. This model treats the inner magnetosphere plasma as an isotropic, slowly flowing ($V \ll V_{thermal}$ and $V \ll V_{Alfven}$ (Wolf, 1983)) fluid that is electromagnetically

drifting due to corotation and electromagnetic fields. The plasma is divided into many independent fluids of varying energy and species, whose flux tube averaged characteristics are advected through the magnetosphere. This approach is better suited to handle the intricacies of this region versus single-fluid MHD.

The RCM characterizes the plasma by adiabatic energy invariant, λ, defined in Equation 3.14, where W is kinetic energy, and flux tube content, η, defined in Equation 3.15, where n is number density. In each of these definitions, V is flux tube volume, specified in Equation 3.16. The plasma is separated into fluids both by species and by set energy invariant windows. In the version used here, there are 200 fluids: 30 electron fluids, 85 proton fluids and 85 O^+ fluids.

$$\lambda = WV^{2/3} \tag{3.14}$$

$$\eta = nV \tag{3.15}$$

$$V = \int \frac{1}{B} ds \tag{3.16}$$

The individual fluids are advected through the system using Equation 3.17, where the subscript s denotes an individual fluid, q is electric charge, Φ is electric potential in the ionosphere, Φ_c is the corotation potential, and L represents explicit losses. While there are several loss mechanisms, such as precipitation and charge exchange, the version employed in later chapters only handles loss through the model boundary. The algorithms used to numerically solve Equation 3.17 are detailed by Toffoletto et al. (2003).

When the RCM is not coupled to the IE and GM modules, Φ is calculated self-consistently by calculating the field-aligned currents (Vasyliunas, 1970), acquiring ionospheric conductance from an external source, and leveraging current conservation in the ionosphere. This process is extraneous because of coupling to the IE component, so further description is neglected here.

$$\frac{\partial \eta_s}{\partial t} + \frac{\mathbf{B} \times \nabla \left(\Phi + \Phi_c + \frac{\lambda_s}{q_s} V^{-2/3} \right)}{B^2} \cdot \nabla \eta_s = -L \tag{3.17}$$

Because the RCM works with flux tube averaged quantities, it is spatially two-dimensional. An ionospheric grid is used, where each point represents the footprint of a flux tube. The inner boundary is 9.86° invariant magnetic latitude; the outer boundary is set to encompass as much of the inner magnetosphere as is desired. In this study, the outer boundary is dynamic, following the boundary of last closed field lines. Initial and boundary conditions for the stand-alone code require empirical and/or measured information. Again, detailed description of this process is neglected in favor of the SWMF coupling used instead.

The IM component receives flux tube volumes from the GM component and returns pressure values to correct those calculated in GM (De Zeeuw et al., 2004). Density and temperature values are calculated from the GM component by treating them as moments of the distribution function (assumed to be maxwellian-shaped). The proton temperature is set to 7.8/8.8 of the total plasma temperature; electron temperature is 1/8.8 of the total. IM receives the ionospheric electric potential from the IE component, creating a self-consistent inner magnetosphere when all three components are used.

Transfer of information from GM to IM is expedited by efficient ray-tracing algorithms in BATS-R-US, described in De Zeeuw et al. (2004). The ray tracing allows

field lines to be quickly traced from hemisphere to hemisphere, yielding flux tube foot points and averaged densities and temperatures. It also yields the open/closed field line boundary, which is handed to the IM module on each coupling to update the spatial boundary on a continuous basis.

3.5 Polar Wind

The Polar Wind (PW) module has been recently developed to capture the processes that occur in the "gap" region, or the region between ionospheric altitudes and the inner boundary of the GM component. In this area, ionospheric outflow is an important dynamic. Accurate knowledge of this outflow is critical, as this source of plasma into the magnetosphere is known to provide mass to the plasmasphere, and may be a dominant source for plasma sheet and ring current ions (see Chapter V).

This region is currently modeled by the Polar Wind Outflow Model (PWOM) (Gombosi et al., 1985, 1991; Glocer et al., 2007). The PWOM solves the one dimensional gyrotropic continuity, momentum, and energy equations (Gombosi and Nagy, 1989) which describe supersonic outflow along magnetic field lines. At Earth, the PWOM solves these equations for electrons and three ion species: H^+, He^+, and O^+. All horizontal motion is dictated by the $\mathbf{E} \times \mathbf{B}$ drift of the magnetic field lines, which is controlled externally through coupling with the IE module.

Because horizontal and vertical motion in PWOM are independent of each other, the grid layouts for each direction are very different. Vertically, there are 390 points along each field line modeled from the lower boundary (set at an altitude of 250km in the following chapters) to the upper boundary (set at 8000km). This creates a uniform spacing of 20km between points. Horizontally, the grid is unstructured,

allowing the foot point of each field line to drift as the ionospheric electric field dictates. 125 field lines are used here.

The PW module couples to the GM module by providing new mass and velocity inner boundary conditions. It receives ionospheric electric potential and field-aligned current locations from the IE module. Although this model does not directly couple to the IM module, it will be shown later that mass leaving the ionosphere through the PW component arrives in the IM module by means of magnetospheric convection through the GM module.

CHAPTER IV

Validating the Space Weather Modeling Framework Magnetosphere

4.1 Introduction

As numerical models mature, it becomes increasingly necessary to validate their results against measurements of the environment being modeled. Thorough validation expands the understanding of models and aids in the interpretation of their results. It also allows code developers to track the impact that changes in the code have on the results. Validation is necessary for operational applications of numerical models, as users rely on the code's accuracy.

This chapter presents validation results of the SWMF magnetosphere, using several components, against in-situ magnetic field and plasma measurements. The validation is performed over a wide range of magnetospheric conditions, and the simulations are run in the same manner as they would under operational conditions. Performance of the SWMF to predict these measurements is assessed both qualitatively and quantitatively. These results will serve as a baseline to compare to future validation as the SWMF's capabilities are expanded.

To increase the operational relevance of this study, the system's capability to predict satellite crossings of the magnetopause at geosynchronous orbit is investigated. These events cause a rapid change in the near-spacecraft plasma environment and

can trigger a spacecraft anomaly. Prediction of such crossings would help fulfill the list of user requirements listed in the European Space Agency's 2001 survey (Horne, 2001).

This work is the first intensive validation of magnetospheric magnetic field and plasma properties as predicted by the SWMF when using the coupled models described in Chapter III. Each model has been validated individually to varying degrees (Powell et al., 1999; Ridley et al., 2001; Tóth et al., 2007), and limited data-model comparisons of the system have been made in the past (Ridley et al., 2002). This study expands upon this previous work and is part of a larger validation effort of the SWMF, whose results are described by Yu and Ridley (2008) and Wang et al. (2008).

4.2 Procedure

Ten events, listed in Table 4.1, were selected for simulation. The events were selected to provide a broad range of space weather conditions. Each event is simulated using the Space Weather Modeling Framework (SWMF) with different combinations of physical modules activated (details below). Satellite-specific magnetic field and particle data is extracted to make one to one comparisons with several different scientific satellites. To further demonstrate the operational capabilities of the system, magnetopause crossings of geosynchronous satellites are treated as binary events, with contingency tables constructed to quantify predictive performance of these events.

4.2.1 Model Configuration

For the greater portion of this study, the SWMF was configured to use three components: Global Magnetosphere (GM), Inner Magnetosphere (IM), and Ionospheric

Event Date	Start Time	Duration	Quick Description
December 9^{th}, 1996	18:00 UT	30 hours	High speed stream
May 4^{th}, 1998	2:00 UT	12 hours	Strongly Driven Storm
July 15^{th}, 2000	14:00 UT	12 hours	Bastille Day Event
March 31^{st}, 2001	2:00 UT	12 hours	CME-Driven Storm
August 4^{th}, 2001	12:00 UT	12 hours	Steady -Bz IMF
August 31^{st}, 2001	12:00 UT	12 hours	Pressure Triggered Substorm
April 17^{th}, 2002	8:00 UT	24 hours	Sawtooth Storm
October 29^{th}, 2003	2:00 UT	28 hours	First Halloween CME
November 20^{th}, 2003	4:00 UT	20 hours	Strong Storm
September 2^{nd}, 2004	16:00 UT	6 hours	Untriggered Substorm

Table 4.1: List of events chosen for this study with start, duration and a short description.

Electrodynamics (IE). This is a widely used setup for scientific research. It also provides an excellent balance of performance, robust output, and execution speed. For the latter portion, the IM component is disabled to investigate the system's behavior without it. Finally, IM is re-enabled and the Polar Wind (PW) module is activated to analyze the impact of accurate modeling of ionospheric outflow on the other components.

The system is configured to achieve near real time run speeds using 32 processors on NASA's "Columbia" SGI Altix machine. Simulation parameters are constant throughout the study; inputs and parameters are not tailored to individual events. Coupling of the components occurs every five seconds of simulation time for GM-IM and every ten seconds for GM-IE, IM-IE, IE-PW, and GM-PW.

Numerical parameters for the GM module were selected to maximize execution speed, metric performance, and stability. Simulations of the May 4, 1998 event were repeated to determine the effect of the most important numerical parameters implemented in the code. These include the solver, implicit or explicit time stepping scheme, Boris speed of light scaling factor (Gombosi et al., 2002), and if the code solves for conservative or nonconservative variables. Table 4.2 presents the results of six stable runs. Performance is quantified by the ratio of run time to event duration

and by the Root-Mean-Square error (see Section 4.2.2) of the modeled Dst index to the measured Dst index. Of the six parameter combinations listed in Table 4.2, the first setup provided the best overall results and was used for this study. All execution speeds shown in Table 4.2 were increased drastically by improving the coupling order between GM and IM to prevent computational bottle-necks.

#	Solver	Boris	Conservative Criteria	Time Stepping	Speed	Dst RMS
1	Rusanov	0.02	Default	Part Implicit	0.873	0.276
2	Rusanov	0.01	Default	Part Implicit	0.829	0.314
3	Rusanov	0.02	Fully Con	Part Implicit	0.963	0.422
4	Linde	0.05	Con at Bowshock	Explicit	0.329	0.314
5	Linde	0.01	Con at Bowshock	Part Implicit	0.676	0.346
6	Linde	0.05	Con at Bowshock	Part Implicit	0.808	0.324

Table 4.2: Results of Run speed is given as the ratio of run time to event duration.

The resolution used in the GM component for this study is coarser than what is typically used in science-grade runs in order to achieve near real-time simulation completion (Figure 4.1). Towards the inner boundary, the resolution is the finest ($1/4R_E$). Cell size increases to $1/2R_E$ at geosynchronous locations and to 1 R_E for the outer magnetosphere and plasma sheet region. This grows, by factors of 2, to a maximum cell size of 8 R_E.

The BATSRUS model provides the magnetic field values that are compared against in-situ measurements. To simplify the comparison, "virtual satellites" are flown in BATSRUS. Satellite orbits are given to the code as part of the input. Then, as the event is simulated, the MHD solution is interpolated to the satellite's position and saved. In this way, one-to-one comparisons of measured and predicted values can be made easily.

Because the IM component yields more complete information about the inner magnetosphere particle distribution than the other components used, its solution is used for the plasma density and temperature comparisons. Extraction of this

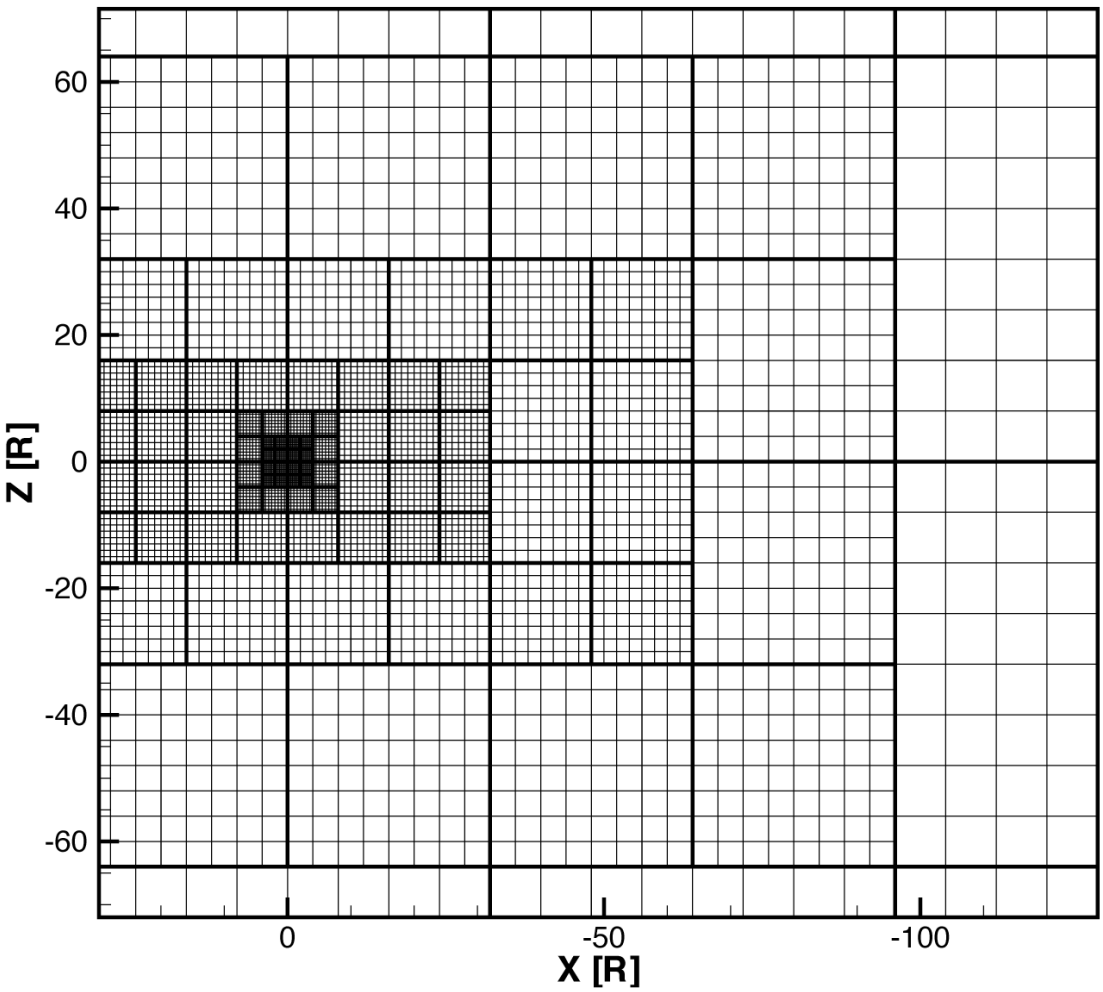

Figure 4.1: The grid used for the BATSRUS code as seen in the Y=0 plane. The grid extends to $\pm 128 R_E$ in the Y and Z directions, and from 32 R_E to $-224 R_E$ in the X direction. The grid is symmetric such that a slice in the Z=0 plane would look identical to this slice. The resolution is finest near the Earth ($1/4 R_E$), growing to a maximum cell size of $8 R_E$ at the outer boundaries.

information along a satellite orbit, as done in BATSRUS, is more complicated because of RCM's 2d ionospheric grid. To determine a satellite's position on this grid, the magnetic field line passing through the satellite's location is traced down to the ionosphere. This tracing is performed by the BATSRUS code (detailed in De Zeeuw et al. (2004)), and the ionospheric footprint of the satellite is passed to RCM when the codes are coupled together. The RCM solution is then interpolated to this position to provide satellite-specific particle distribution information.

4.2.2 Data-Model Comparisons

Satellite specific data, extracted as described by the GM and IM modules, is compared to several in-situ sources to assess model performance. Magnetic field results are compared to fluxgate magnetometer measurements aboard the Polar, Geotail, GOES 8-12, Wind, and Cluster satellites. Particle density and energy results from the RCM model are converted to energy flux and compared to measured spin-averaged energy flux values from the Magnetospheric Particle Analyzer (MPA) instrument aboard the LANL geosynchronous spacecrafts. The instrument and data are described in McComas et al. (1993). Quantitative assessments of plasma density and temperature are made by comparing to density and temperature moments of the MPA measured distribution function for $\sim$100 eV to 40 keV (ions) and $\sim$30 eV - 40 keV (electrons) energy windows. RCM results are integrated over equivalent energy ranges to ensure proper comparisons.

Two mathematical tools are used to quantify the SWMF performance: normalized root-mean-squared error (nRMSE) and correlation coefficient. Correlation coefficient is discussed further in Jolliffe and Stephenson (2003), while nRMSE is also applied in Ridley et al. (2002), Yu and Ridley (2008), and Wang et al. (2008). The formulas for both metrics are presented in Equations 4.1 and 4.2, where x is the measured value, y is the predicted value, and n is the number of data-model pairs used in the calculation. The correlation coefficient ranges from -1 (data and model are anti-correlated) to +1 (perfect correlation), with 0 indicating no correlation. nRMSE ranges from 0 (model is perfect prediction of data) to ∞. A value of 1 indicates that the predicted values are within ± 1 mean of the measured values. This value can be misleading, as a persistent prediction of 0 can yield a nRMSE of 1. Hence, nRMSE scores must be paired with the correlation coefficient for proper interpretation.

$$Corr.\ Coeff.\ =\ \sqrt{\frac{(\sum_i^n x_i y_i - n\overline{xy})^2}{(\sum_i^n x_i^2 - n\overline{x})(\sum_i^n y_i^2 - n\overline{y})}} \tag{4.1}$$

$$nRMSE\ =\ \sqrt{\frac{\sum_i^n (x_i - y_i)^2}{\sum_i^n x_i^2}} \tag{4.2}$$

4.2.3 Magnetopause Crossings

At geosynchronous orbit, magnetopause crossings can be detected in both magnetic field and particle data. In magnetic field data, a sudden change from magnetospheric field to solar wind field (typically, a sharp drop in Bz in GSM coordinates) indicates a crossing (Rufenach et al., 1989). In MPA spectrograms, a sudden change in the particle distribution is observed as the spacecraft moves from the magnetosphere to the magnetosheath (McComas et al., 1994). In RCM data, a crossing appears as a period of missing data because the spacecraft no longer resides in the RCM domain (closed field lines.) All crossings captured in the model are due to BATSRUS results, as this model provides the magnetic field configuration for RCM.

Magnetopause crossings are treated as binary events where a useful forecast would be an unqualified statement that the event will or will not happen. A discussion on the handling of binary events can be found in Jolliffe and Stephenson (2003). The ability of the coupled system to predict these crossings is examined on two timescales: whole event and hourly. For each time increment, there are four possible outcomes: a "hit" (event was predicted and occurred), a "miss" (event occurred but was not predicted), a "false alarm" (event was predicted but did not occur), and a "true negative" (event was neither predicted or occurred.) The results are tallied into contingency tables, and several basic metrics are calculated: hit rate (hits divided by

number of observed crossings), false alarm rate (number of false alarms divided by total number of non-occurences), and critical success rate (number of hits divided by total number of occurrences plus false alarms). CSR is especially suited for scoring predictions of rare events because it neglects non-occurrences.

4.3 Analysis & Discussion

Figure 4.2 displays the data-model comparison for the Geotail satellite during the May 4, 1998 event. The top row shows the satellites position during the event in the X-Y and X-Z planes. The next three rows show the measured (blue dashed) and forecast (black solid) magnetic field in three components. During this event, the Geotail satellite is residing in the dusk flank magnetosheath region. As demonstrated by the excellent data-model comparison, BATSRUS excels at folding the Interplanetary Magnetic Field (IMF) through the bowshock and around the magnetopause. Towards the end of the event, the differences between the data and the model are due to discrepancies in the location of the magnetopause. With an extremely coarse grid at this location, such a discrepancy is not surprising. This comparison is a typical example of outer magnetosphere results.

Similar to Figure 4.2, Figure 4.3 displays the data-model comparison for the GOES 9 geosynchronous satellite during the May 4, 1998 event. Typical of all geosynchronous magnetic field comparisons in this study, the large scale features of the magnetic field are captured well. However, the Z component is consistently over predicted, while the X and Y components are consistently under predicted. This demonstrates that the SWMF magnetic field is less stretched than the measured field. Remedying this issue requires a stronger ring current. Despite this shortcoming, the metric scores are still favorable (as discussed in Section 4.4).

Two dipolarizations of the magnetic field, caused by events such as substorms and sawteeth, are observed in the Z component of the measured data at 8:00 and 9:00 Universal Time (UT). Small time and spatial features such as these are nearly always missed, but do not hamper the metrics significantly because of their brevity. Although the geosynchronous results would imply that the coupled codes are incapable of reproducing such events, this is not the case. Figure 4.4 displays results from the August 31, 2001 event, where a plasmoid forms and releases both in the modeled and observed magnetotail. The top frame shows the X component of the magnetic field as measured by a single Cluster satellite (blue dashed line) and as predicted by the SWMF (black line). The next two frames show Y=0 slices of the magnetotail. Field lines are traced in black; the contours show pressure. At 17:00 UT (center frame), the plasma sheet is thin and elongated before a plasmoid quickly forms and travels down tail. At 17:10 (bottom frame), the plasmoid has passed the cluster constellation. This behavior is reflected in both the measured and modeled magnetic field in the top frame. The differences between the two indicate a difference in plasmoid size and location, but the timing of the event is correct.

While substorms such as the one observed in Figure 4.4 form frequently in the model results, they are not observed in the model results at geosynchronous orbit. An explanation for this may be that the reconnection rate in the tail is too fast, thus not allowing for enough energy to build up in the tail before the plasmoid is released. This hypothesis requires further investigation, which, using the events selected for this study, is hampered by limited data coverage in the tail region.

Examining magnetopause crossings may provide further information about the above issues. Figure 4.5 displays the proton results from the LANL-97A satellite during the May 4, 1998 event. The top row shows the position of the satellite in

three planes (GSM coordinates). During the event, the satellite spent a significant time on the dayside of the magnetosphere. The next two rows display proton energy flux ($Log_{10}(eVcm^{-2}sec^{-1}str^{-1}eV^{-1})$) as simulated by the coupled codes (center plot) and as measured by the LANL MPA instrument (bottom plot). Several distinct magnetopause crossings are observed in the in-situ measurement: a persistent crossing from approximately 3:00 to 5:30 UT, followed by three short, well-pronounced crossings starting at 5:45 UT. The SWMF correctly predicts the first, prolonged crossing as indicated by the drop out in the RCM results. The next three, however, are not captured. During these periods, the virtual satellite is so close to the RCM outer boundary that the recorded distribution is boundary plasma provided by BATSRUS, but the magnetopause is not crossed. Figure 4.6 displays the solar wind drivers for this event, originally measured by the ACE spacecraft and time shifted from the Lagrangian point to the upstream boundary of the GM component. Examining the X-component of the IMF (center row) reveals that the IMF is strongly southward during the first magnetopause crossing observed in Figure 4.5. This crossing was clearly driven by magnetic erosion of the dayside magnetosphere. The next three crossings correspond to strong pressure pulses in the solar wind, as seen in the number density in Figure 4.6 (fourth from the top). The model's increased sensitivity to dayside reconnection over pressure pulses as drivers for magnetopause crossings, a consistent pattern in the results, supports the conclusion that the reconnection rate in the code may be faster than the real world rate. The modeled magnetosphere's resilience to the pressure pulses may indicate too much thermal pressure in the inner magnetosphere on the dayside.

There are numerous other factors that affect the magnetopause crossing results. Although the BATSRUS model takes into account the tilt of the Earth's intrinsic

dipole field, it neglects the offset from the center of the Earth. This has the effect of artificially strengthening the field on the American sector of the Earth and weakening it on the opposite side. The low resolution used, chosen to allow the simulations to finish quickly, also plays a role. At 1/2 R_E cell size, one grid point can be the difference between well inside or outside of the magnetosphere. This is seen in Figure 4.5, where the satellite is a mere one cell away from being in the magnetosheath. Although these near misses stand out qualitatively, they are counted as misses in the magnetopause crossing contingency tables discussed in Section 4.4.

Figure 4.5 exemplifies the model's particle performance during storm-time conditions. Because the RCM is initialized with single-fluid MHD plasma, during the first moments of the simulation, the simulated plasma distribution at all locations is a Maxwellian determined from the BATSRUS solution. Southward IMF imposes a convection electric field capable of drawing in fresh plasma from the tail boundary of the RCM, which is quickly accelerated to keV energies and begins to circulate around the Earth. This creates a more favorable data-model comparison of the warmer (keV energies) plasma, as is observed starting at 8:00 UT in Figure 4.5. Any southward turning leads to a fresh injection of plasma from the tail and a corresponding dispersion pattern in the RCM results (e.g., 8:00 UT, 9:00 UT, 10:00UT, etc. in Figures 4.5 and 4.6). This pattern is observed in the in-situ data for longer, stronger southward IMF turnings (e.g., 10:45 UT), but overall dynamics are not captured accurately. There is a clear void in the simulated cold plasma distribution due to the lack of cold, ionospheric sources of particles in the version of RCM used in this study.

Figure 4.7 shows the results from Figure 4.5 integrated over the 100eV to 46.5keV energy window to yield a single proton density and temperature. The effects described above are clearly observed in the integrated results. Notably, the lack of

a direct cold particle source from the ionosphere into the RCM drives up the predicted proton temperature while keeping the predicted density too low. Additionally, dynamics are captured poorly. These are persistent features of the data-model comparisons and are reflected in the statistics outlined in Section 4.4.

Results from the August 4, 2001 and September 2, 2004 event demonstrate the importance of IMF B_z in the particle results. The driving solar wind conditions for the 2001 event are displayed in Figure 4.8. The IMF B_z is steadily southwards for the greater portion of the event (center plot), while the density and velocity remain relatively steady throughout. The solar wind drivers for the 2004 event (Figure 4.9) are similar, but with B_z northward. Data-model proton energy flux comparisons are shown in Figures 4.10 and 4.11. As during the 1998 event results, both RCM particle distributions are initialized as Maxwellians using the MHD solution. The model results from the 2001 event (Figure 4.10) are quickly energized with fresh plasma that has been accelerated through the plasmasheet and into the inner magnetosphere. Although the dynamics are lacking, the average warm plasma characteristics are captured reasonably well by the coupled codes. In stark contrast, the model plasma from the 2004 event (Figure 4.11) remains stagnant throughout. Neither the cold or warm populations are captured well, even though the in-situ measurements show that the real plasma is equally unexciting. Because of this, plasma results are less dependable during periods of steadily northward IMF B_z.

The observed plasma distribution in Figure 4.10 exhibits a feature that may exacerbate the discrepancy between the measured and modeled integrated plasma properties. As warm electrons build up on the spacecraft's body, cold ions are accelerated toward the sensor, raising their measured energy. This generates a "cold ion line", as observed from 16:00 UT to the end of the event. This draws cold particles into the

warm plasma integration window (> 100 eV), causing the overall measured density to rise and temperature to fall. This effect cannot be properly removed from the MPA data at the present time.

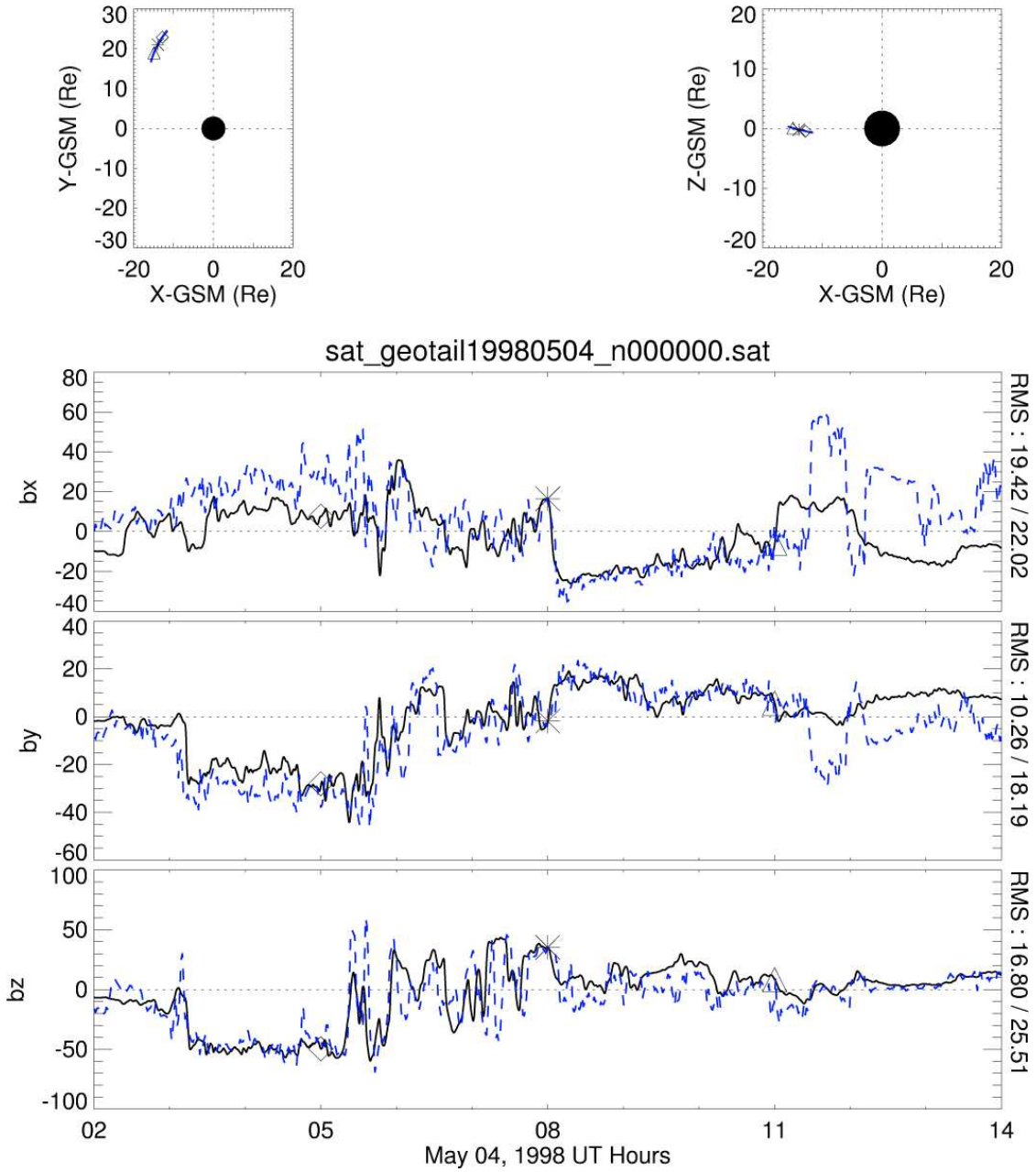

Figure 4.2: Comparison between Geotail measured (blue dashed lines) and SWMF forecasted (black solid lines) magnetic field (nT) in three orthogonal components in GSM coordinates. The satellite's position during the event is displayed in the top two frames, with the star, diamond and triangle symbols used on both the orbit and magnetic field plots to help coordinate the two.

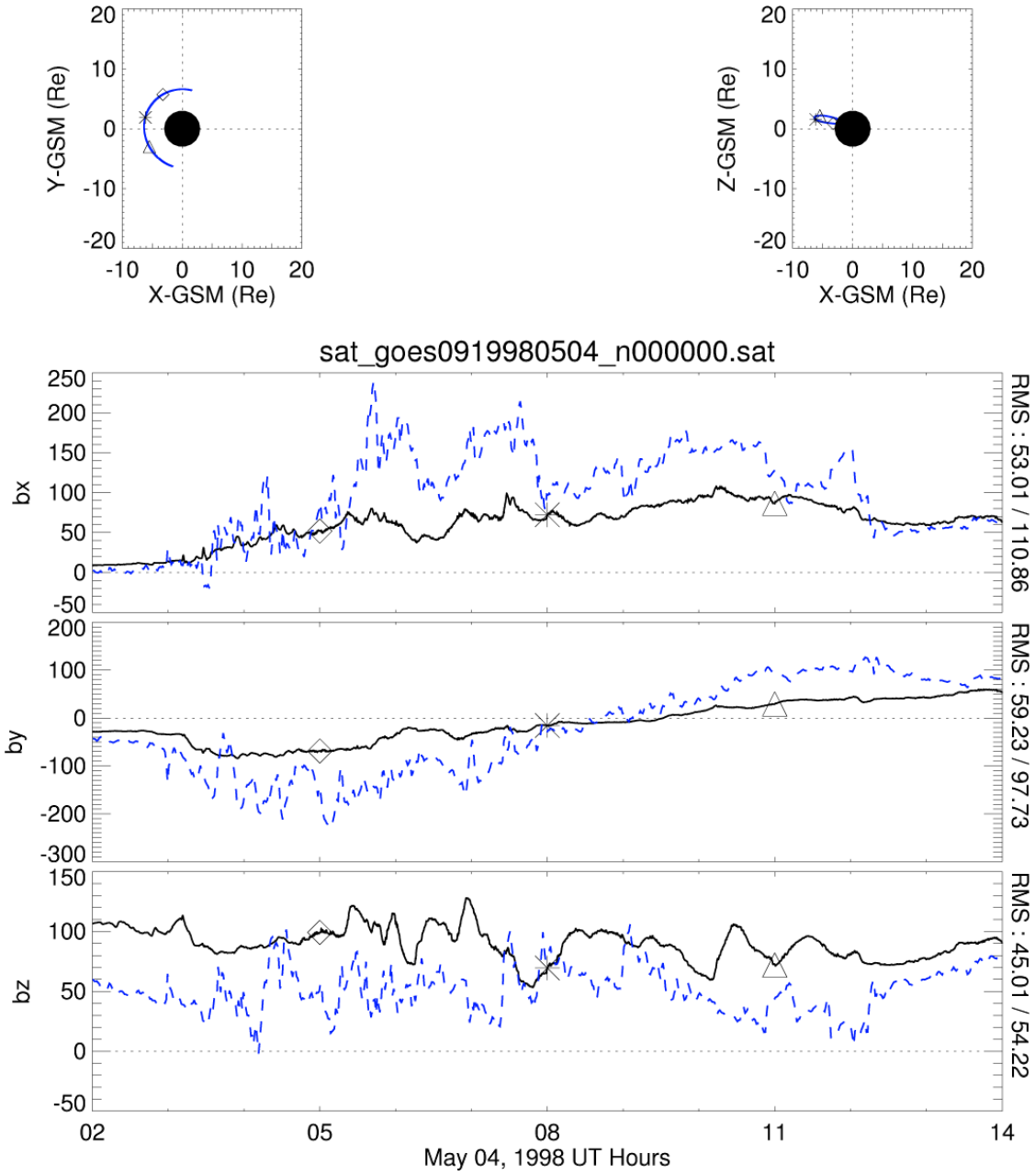

Figure 4.3: Similar to Figure 4.2, but for the GOES 9 geosynchronous satellite.

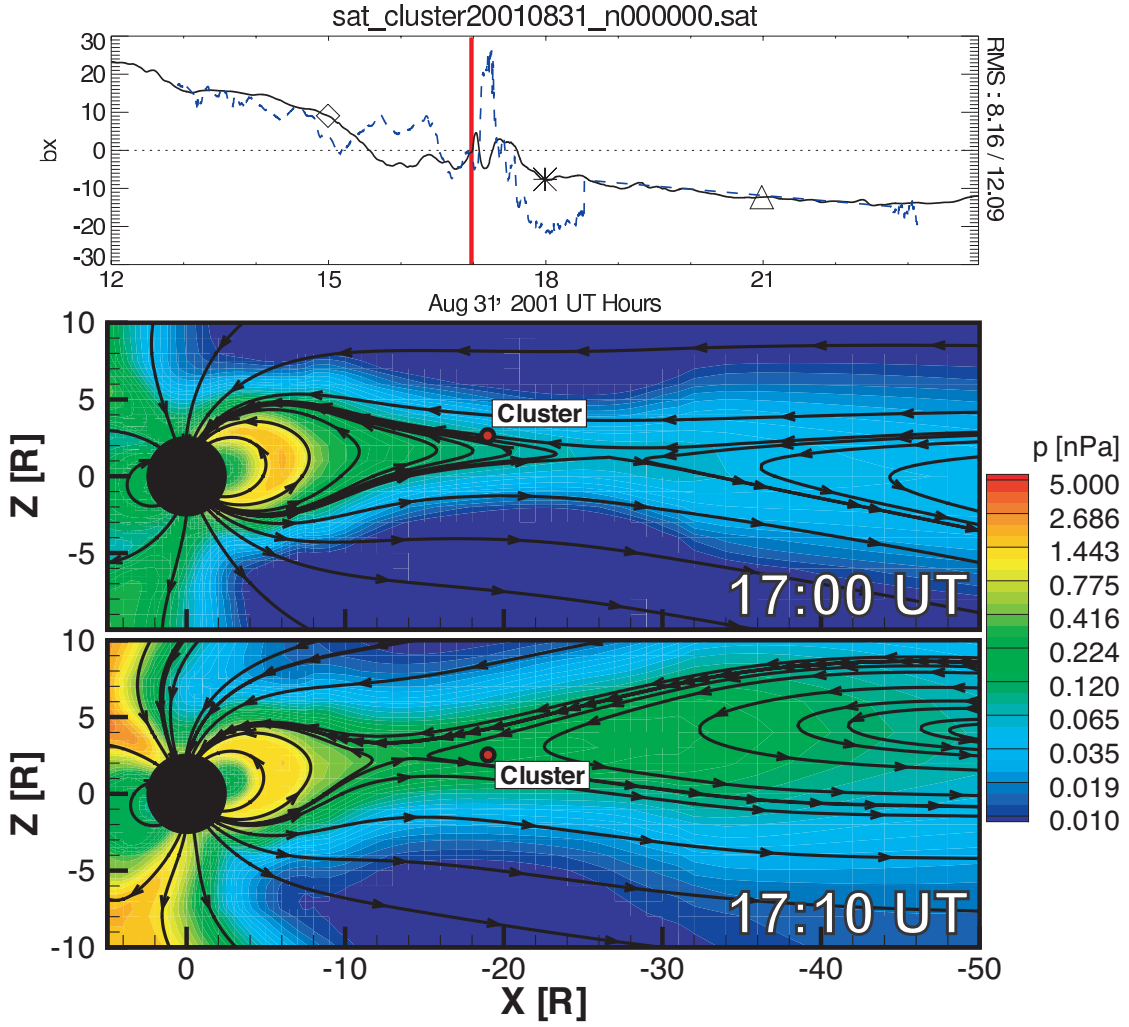

Figure 4.4: Results from the August 31, 2001 event, where an observed substorm is reproduced by the coupled models. The top frame shows the model (solid black) and data (blue dashed) comparison of the X component of the magnetic field for a single Cluster satellite. The vertical red dashed line marks 17:00 UT. The next two frames are Y=0 slices of the magnetotail taken from the simulation results. Field lines are traced in black, the contours show pressure (nPa), and the red dot indicates the location of the Cluster satellite used in the top frame. At 17:00 UT, the plasma sheet is thin and elongated before a plasmoid quickly forms and travels downtail. At 17:10 UT (bottom frame), the plasmoid has passed the Cluster constellation. This behavior is reflected in both the measured and modeled data shown in the top frame.

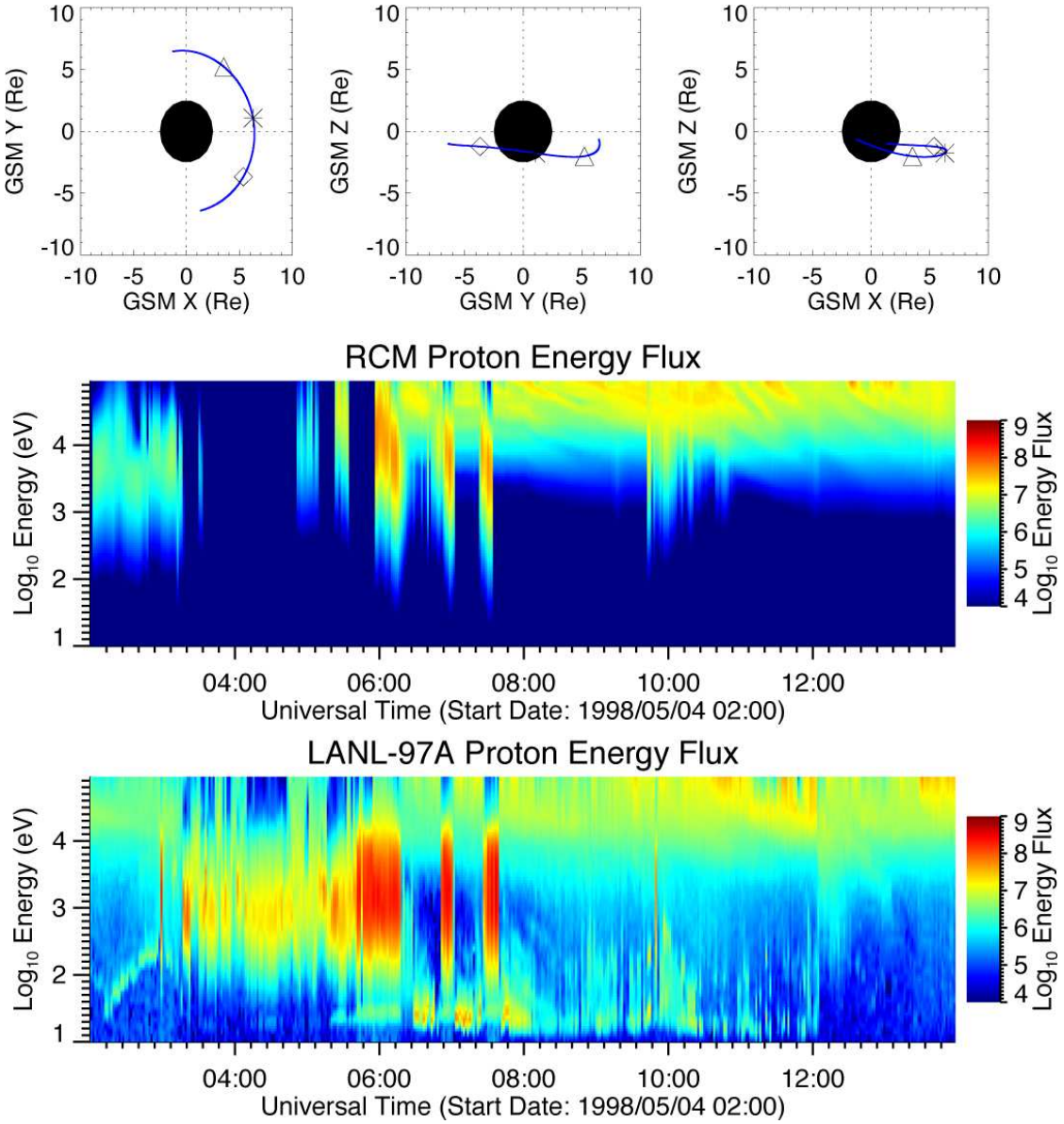

Figure 4.5: Proton energy flux comparison for the May 4, 1998 event at the LANL 97A geosynchronous satellite, as simulated by the coupled codes (center plot) and as measured by the LANL MPA instrument (bottom plot). The color bar is in units of energy flux $Log_{10}(eV * cm^{-2} * sec^{-1} * str^{-1} * eV^{-1})$. The top row shows the position of the satellite in three planes (GSM coordinates).

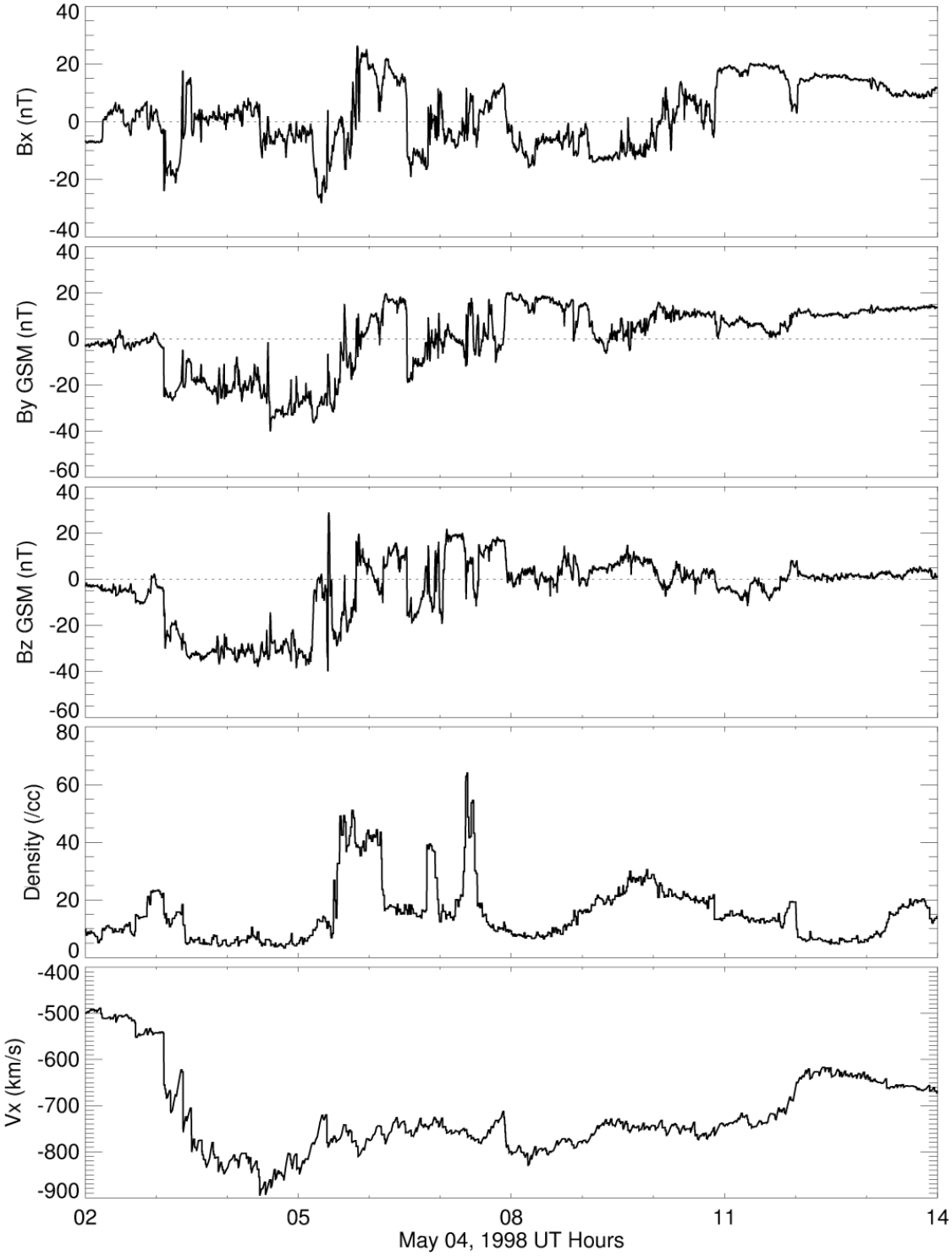

Figure 4.6: Solar wind drivers during the May 4, 1998 event as measured by the ACE spacecraft. Shown, from top to bottom, are the X, Y, and Z component of the IMF (nT), proton number density ($^{1}/_{cm^3}$), and Earthward flow velocity ($^{km}/_{s}$).

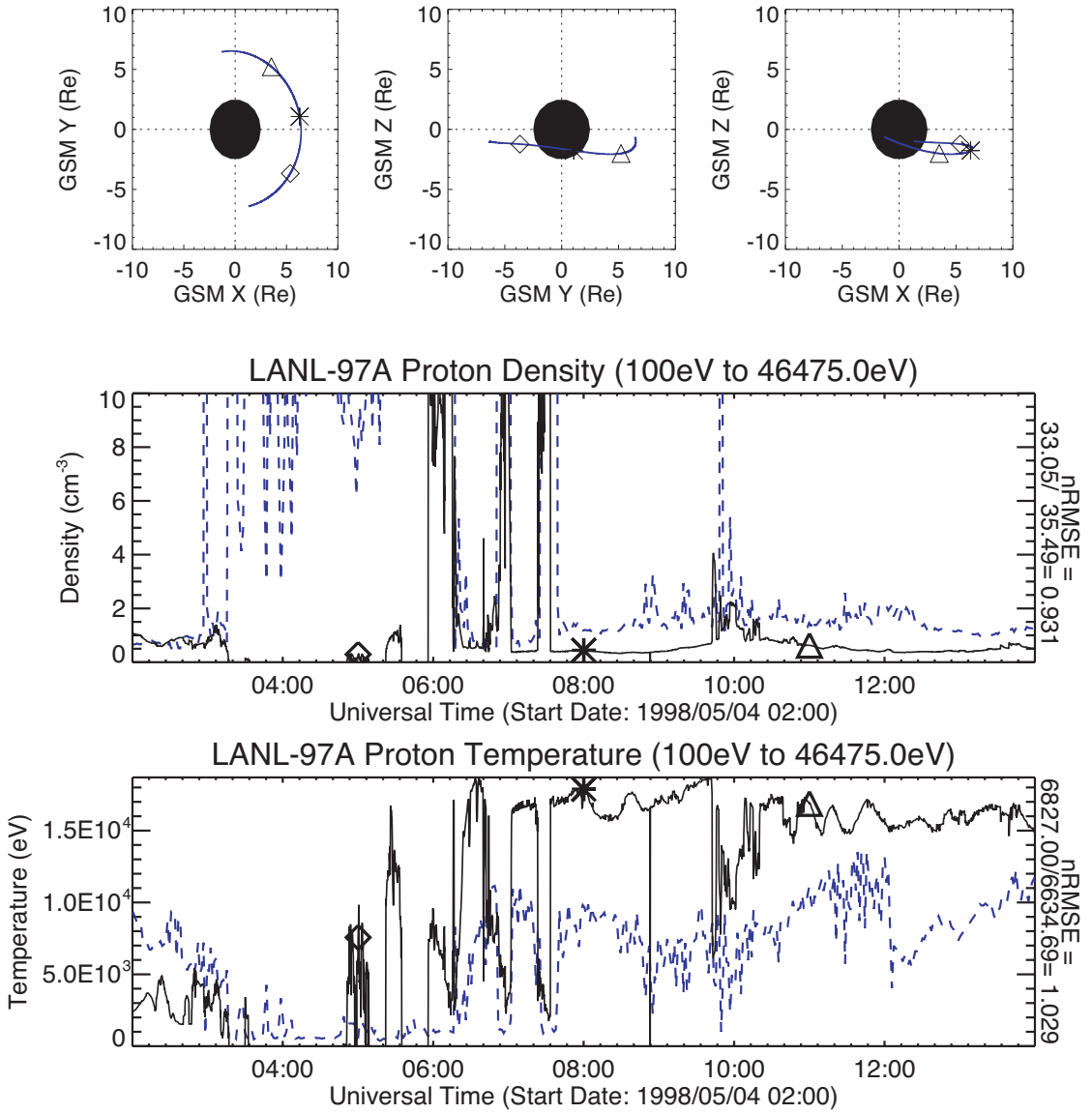

Figure 4.7: A data-model comparison similar to Figure 4.3, but for integrated proton temperature and density at the LANL-97A satellite. The simulation result (black line) was obtained by integrating the RCM result from Figure 4.5 over the same energy window that is used to generate the LANL MPA moment data (blue dashed line). Typical of results throughout the study, RCM plasma for this energy range is too warm and less dense than the in-situ measurement.

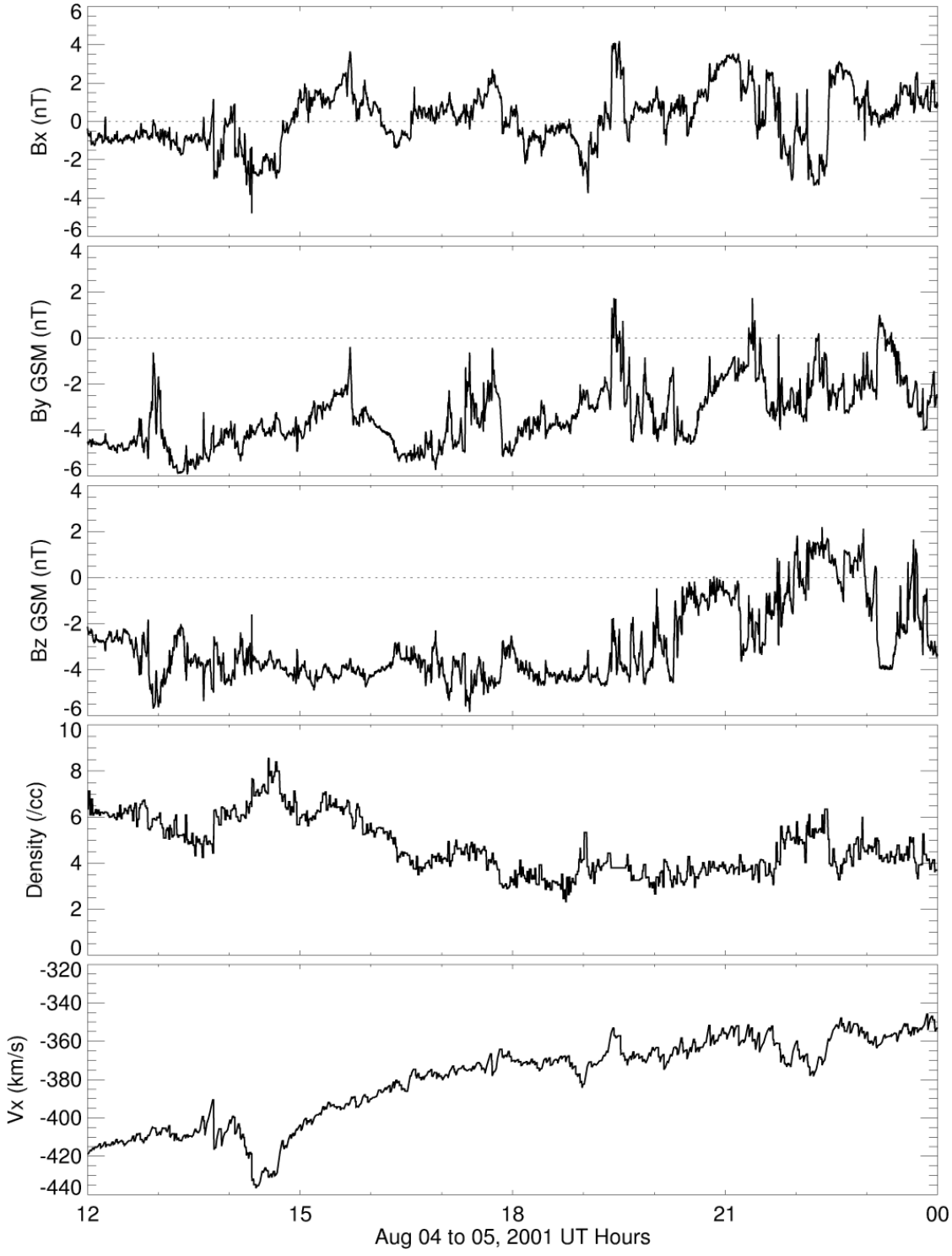

Figure 4.8: Same as Figure 4.6, but for the August 4, 2001 event.

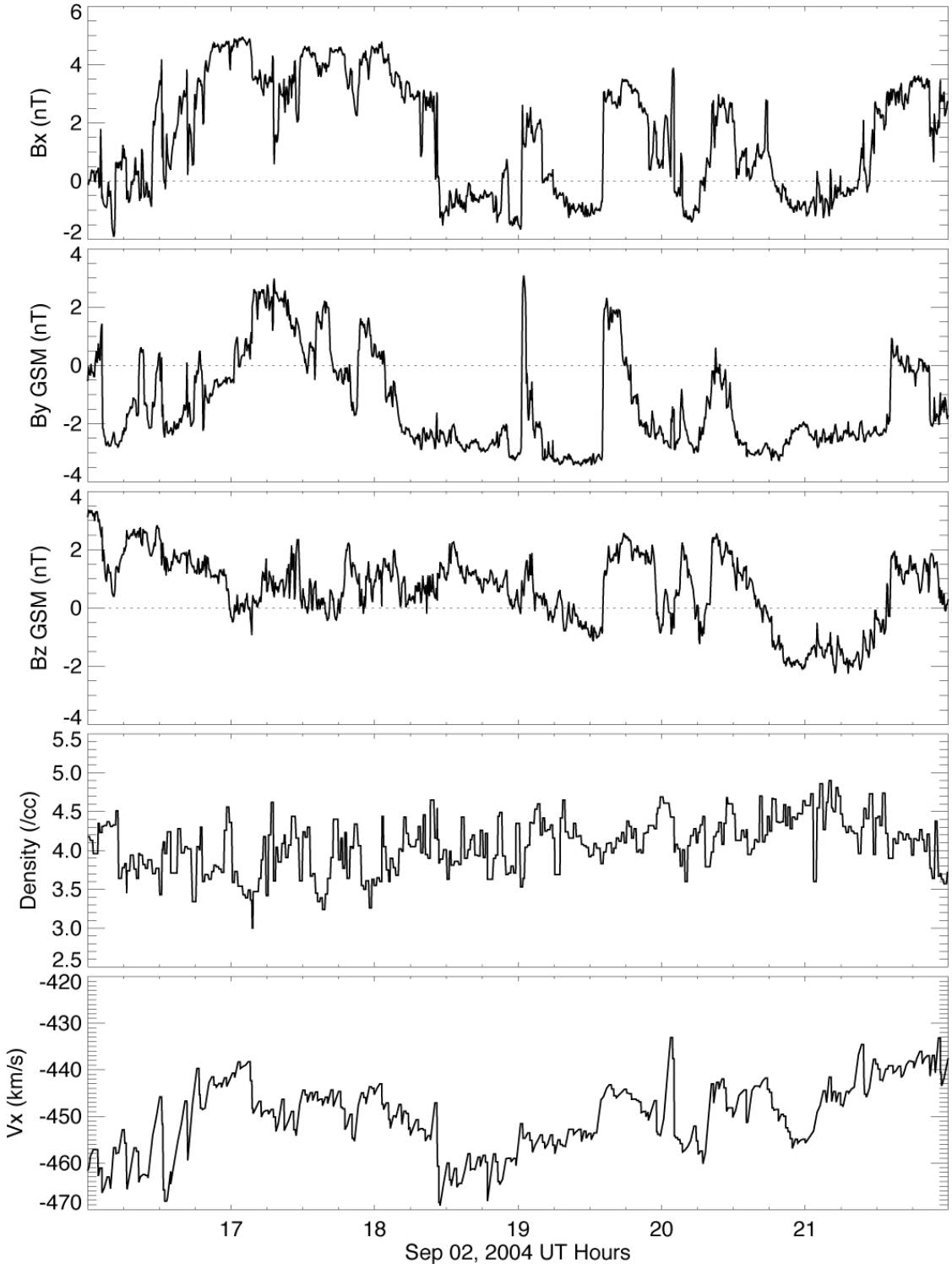

Figure 4.9: Same as Figure 4.6, but for the September 2, 2004 event.

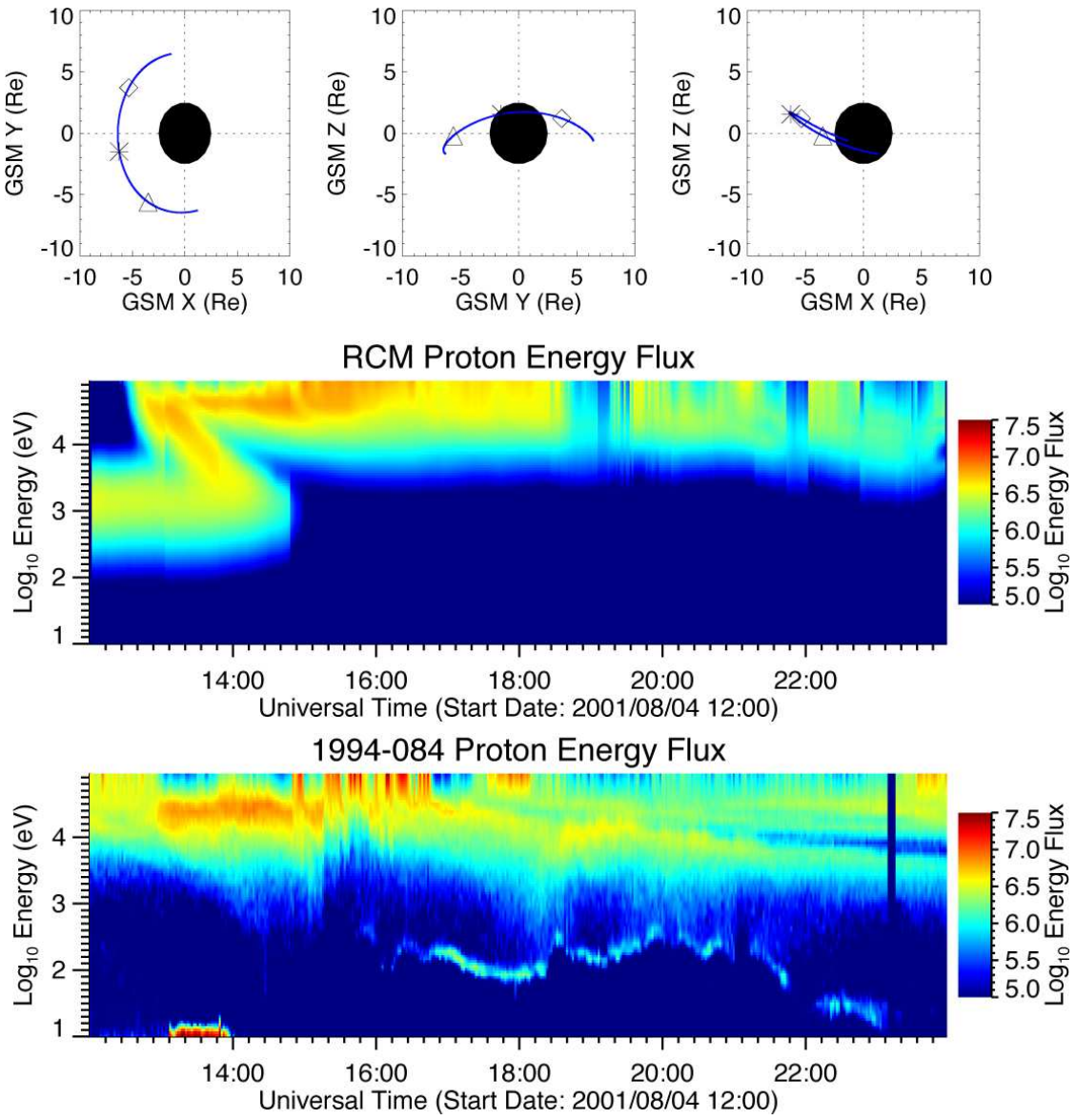

Figure 4.10: Similar to Figure 4.5 but for the LANL 1994-084 satellite during the August 4, 2001 event. The modeled particle distribution is quickly accelerated to resemble the measured distribution due to the southward IMF imposed during the event.

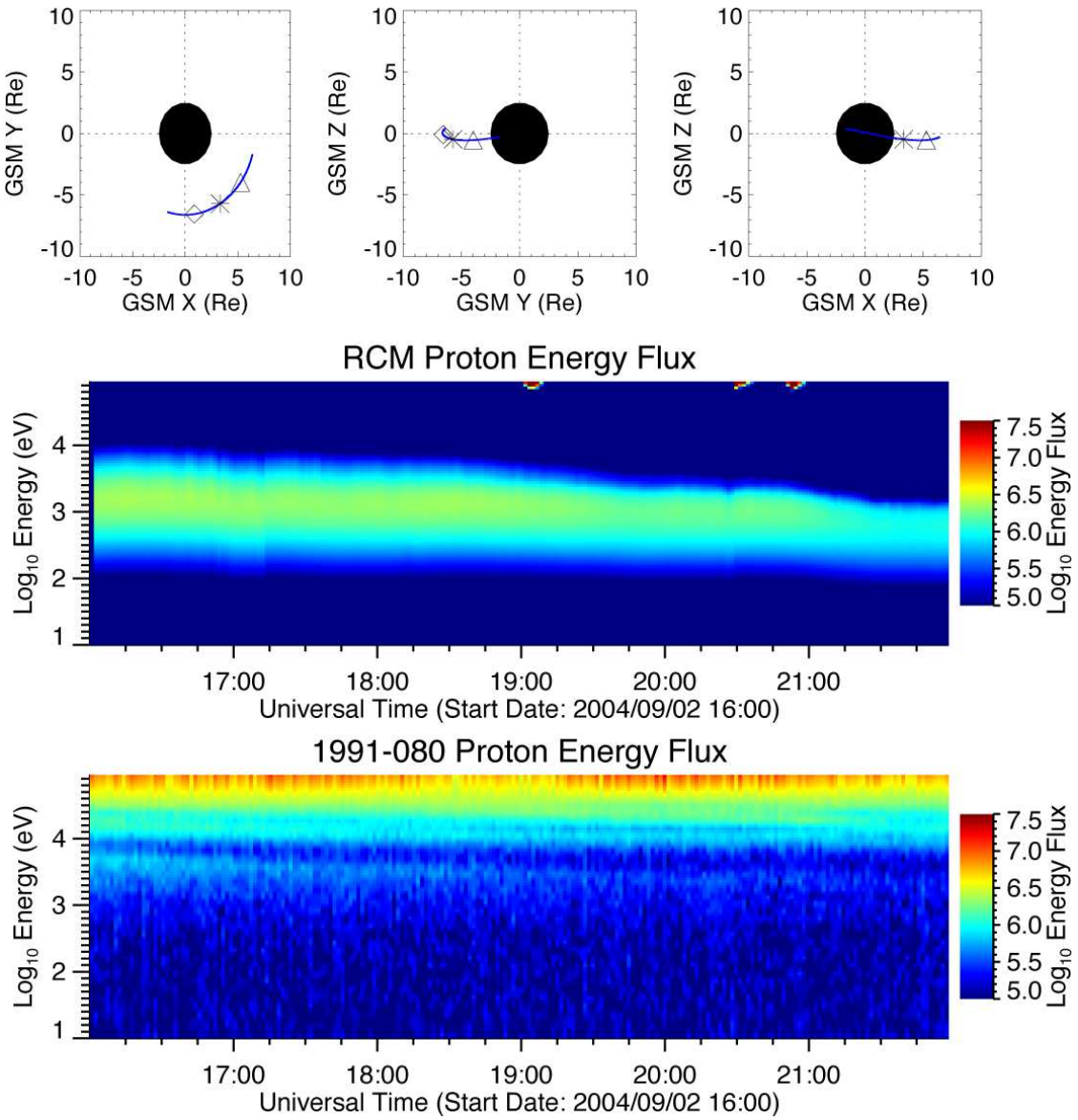

Figure 4.11: Proton energy flux comparison for the September 2, 2004 event. While both distributions show little evolution throughout the event, the model population, which changes little from the initial MHD maxwellian, poorly resembles the observations.

4.4 Summary of GM-IM-IE Results

Table 4.3 displays the average nRMSE and correlation coefficient scores for the data-model comparisons. They are divided up into three orbit categories: polar orbit (consisting of the Polar satellite), geosynchronous orbit (GOES satellites), and outer magnetosphere orbits (Geotail and a single Cluster satellite). For the outer magnetosphere category, any satellite that was upstream of the bowshock was discarded as it was merely mirroring the upstream solar wind input of the simulation. Performance measures were calculated for the three orthogonal components of the magnetic field in GSM coordinates as well as the total magnitude. The number of comparisons included in each average (n) is also listed.

	nRMSE				Corr. Coeff.				
Orbit Type	Bx	By	Bz	$\|B\|$	Bx	By	Bz	$\|B\|$	n
Polar	0.362	0.339	0.343	0.156	0.947	0.931	0.941	0.980	9
Geosynchronous	0.538	0.493	0.573	0.284	0.770	0.866	0.701	0.442	15
Outer Magnetosphere	0.794	0.736	0.669	0.476	0.638	0.666	0.607	0.532	6

Table 4.3: Average performance measures of in-situ magnetic field separated by orbit type: polar orbit, geosynchronous orbit, and outer magnetosphere orbits. Listed are the normalized root mean square errors (nRMSE) and correlation coefficients between the forecast and measured value of the three components of the magnetic field (in GSM coordinates) and the total field magnitude. The value 'n' is the number of comparisons used to generate the average. A data-model pair was discarded if there was little data available or if the measurement was made upstream of the magnetosphere.

Overall performance of the coupled models to predict magnetic field values was good. All average nRMSE scores were well below 1, showing that forecast values are closer to the measured values than the average magnitude of the measured quantity. Average correlation coefficients are greater than 0.6 for all components of the magnetic field, indicating that the model is trending with the data. In every case, the nRMSE for the total field strength was far lower than any of the components, implying that the field strength is represented well, while the field orientation is not as accurate. The opposite is true for the correlation coefficients, where correlation

drops significantly for field magnitude (with the exception of the Polar satellite). This is because, at geosynchronous orbit, the field magnitude has less variation than the individual components, so smaller variations have a large effect on correlation.

Performance of the coupled models decreases as grid resolution decreases (equivalently, as distance from the Earth increases.) The data-forecast comparisons using Polar data performed the best (Table 4.3, top row), as the field is often dominated by the intrinsic dipole as the satellite passes close to the Earth. Correlation coefficients are especially strong (average of > 0.9) for this orbit type. The framework does not perform as well at geosynchronous orbit (Table 4.3, second row), but average nRMSE is still low (< 0.6) and there is a strong correlation for all three components of the magnetic field (average > 0.7.) Forecasts for satellites in the outer magnetosphere/sheath or downstream solar wind have the weakest performance, however all average nRMSE values remain well below one. The forecasts and data values are weakly correlated; coefficients for each component ranges from 0.607 to 0.666.

The particle comparison results are presented in Table 4.4. The first two columns correspond to density and temperature results of $> 100eV$ protons; the second two columns correspond to $> 30eV$ electron density and temperature. The first row is average nRMSE values, the second row is average correlation coefficient. nRMSE values for the particle comparisons are near one, while the correlation coefficient results show that there is little to no correlation between the forecasts and data. While there is negligible difference between electron and proton density performance, on average the predicted proton temperature is more accurate than the electron temperature. Initial investigations found no apparent correlation between magnetic field performance and particle density or temperature performance.

The results of the magnetopause crossing binary event study are presented in

	$H^+(>100eV)$		$e^-(>30eV)$	
	Density	Temperature	Density	Temperature
nRMSE	0.961	0.990	1.096	1.208
Corr. Coeff.	0.274	0.177	0.266	0.096

Table 4.4: Average performance measures of forecasted and measured in-situ particle properties. 19 comparisons were made from the 10 events studied. All particle data was taken from the MPA instruments aboard the LANL geosynchronous satellites. Density and temperature from the model is taken from an energy range that matches the range of the MPA instrument used in the comparison.

Table 4.5 and Table 4.6. Each entry into these tables represents one evaluation of a time window from a single satellite's data-model comparison. For example, in Figure 4.5, a magnetopause crossing was both observed and predicted. For the whole-event time scale, this would add one to the "yes-yes" cell of the contingency table. For the hourly time scale, the first hour (2:00 UT to 3:00 UT) of Figure 4.5 would add one to the true-negative ("no-no") cell, the fifth hour (6:00 UT to 7:00 UT) would increase the number in the miss ("yes-no") cell by one. This data-model comparison would contribute only one value to the whole-event table (Table 4.5) and twelve values to the hourly table (Table 4.6).

Forecast	Observation	
	Yes	No
Yes	13	0
No	1	22
Total	36	

Table 4.5: Contingency table for magnetopause crossings using whole-event time resolution. Events that were both observed and forecasted are "hits", observed but not forecasted are "misses", forecasted but not observed are "false alarms", and events that were not forecasted and not observed are "correct rejections." The analysis of the 36 data-model comparisons yielded a hit rate of 92.9%, a false alarm rate of 0%, and a critical success rate of 92.9%.

Forecast	Observation	
	Yes	No
Yes	32	6
No	31	412
Total	481	

Table 4.6: Contingency table for magnetopause crossings using houly time resolution, similar to Table 4.5. The analysis of the 481 hours of data-model comparisons yielded a hit rate of 50.8%, a false alarm rate of 1.4%, and a critical success rate of 46.4%.

When examining magnetopause crossings on a whole-event time scale (Table 4.5), the SWMF yields a very high hit rate and CSI (both 92.9%) and produced zero false alarms in all 36 satellite data-model pairs examined in the 10 event study. Increasing the time resolution to hourly (Table 4.6) nearly halved the hit rate (50.8%) and CSI (46.4%). The false alarm rate rose only a negligible amount, from 0% to 1.4%. The low false alarm rates show that the SWMF can provide value as a magnetopause crossing predictor for geosynchronous satellites because it rarely predicts a crossing that does not occur. The number of missed crossings, however, is still an issue that needs to be addressed.

4.5 Different Module Combinations

4.5.1 GM-IE

The expected benefit of using the RCM in the IM module is to increase the pressure in the MHD solution. This should help inflate the inner magnetosphere and stretch the field lines to better match observations. This coupling alone is not enough to stretch the field lines to their observed orientations, as is evidenced in the previous sections. This begs the question of how much improvement the RCM is providing the coupled system. To investigate this, the validation simulations were repeated without the IM component. These simulations ran, on average, at 2.5 times faster than real time. Geosynchronous results were recalculated and compared to the previous results to quantify the impact of the RCM.

Table 4.7 shows the difference between the average metrics before and after the IM module is used. For the X and Y components of the magnetic field, there is a slight improvement in both nRMSE and correlation coefficient when the IM is activated. There is a decline in the metrics in the Z component that offsets the improvement in X and Y. All of these changes, however, are small percentages of the

total calculated metrics, so the change in results when IM is activated is negligible. This means, using this model resolution and setup, the RCM has little consequences on the configuration of the inner magnetosphere configuration. The real strength of using the RCM is acquiring full distribution function information of the plasma.

Component	Average nRMSE	Avg. Corr. Coeff.
Bx	-0.037(+)	0.023(+)
By	-0.008(+)	0.011(+)
Bz	0.023(−)	-0.037(−)

Table 4.7: The difference between the average metric scores when the IM module is activated and when the IM module is deactivated. Values marked with a (+) denote an improvement in the results when IM is used, (-) denotes a decline in metric scores.

4.5.2 GM-IM-IE-PW

A single event, the May 4, 1998 strong storm, was simulated again with an additional component: the Polar Wind, or PW module, simulated by the Polar Wind Outflow Model (PWOM). This experiment serves two purposes: to explore the performance of the new PW module, and to get a preliminary evaluation of non-static ionospheric outflow on the coupled models and metric results. The run speed was lowered to less than real time.

Figure 4.12 shows the data-model comparison for GOES 9 satellite magnetic field resulting from the GM-IM-IE-PW simulation. This plot is directly analogous to Figure 4.3. The impact of activating the PW module is increased field line stretching, drastically improving the results for all three components. The difference between the metric scores when the PW is active and inactive is shown in table 4.8. All metrics show drastic improvement. The biggest improvement occurs in the Bz component, where the correlation coeffecient increased from 0.037 (no correlation) to 0.630 (significant correlation). While the field topology shows improvement, the dipolarizations observed at 8:00 and 9:00 UT are still not captured by the coupled

codes.

Component	nRMSE	Corr. Coeff.
Bx	-0.114(+)	0.080(+)
By	-0.278(+)	0.009(+)
Bz	-0.218(+)	0.593(+)

Table 4.8: The difference between the metric scores when the PW module is activated and when the PW module is deactivated. Values marked with a (+) denote an improvement in the results when PW is used, (-) denotes a decline in metric scores.

This result has important implications for the magnetosphere. Not only is the PW mass outflow reaching the inner magnetosphere, it is being energized through the IM component to increase the GM pressure, stretching the field lines. This demonstrates that the ionospheric outflow is vital for properly modeling the plasma sheet and ring current. Because the PW is intrinsically a multispecies code, the additional mass entering the system is H^+ as well as heavier O^+. Further simulations must be performed to cement these results, as well as investigate the impact of O^+ entering the plasma sheet.

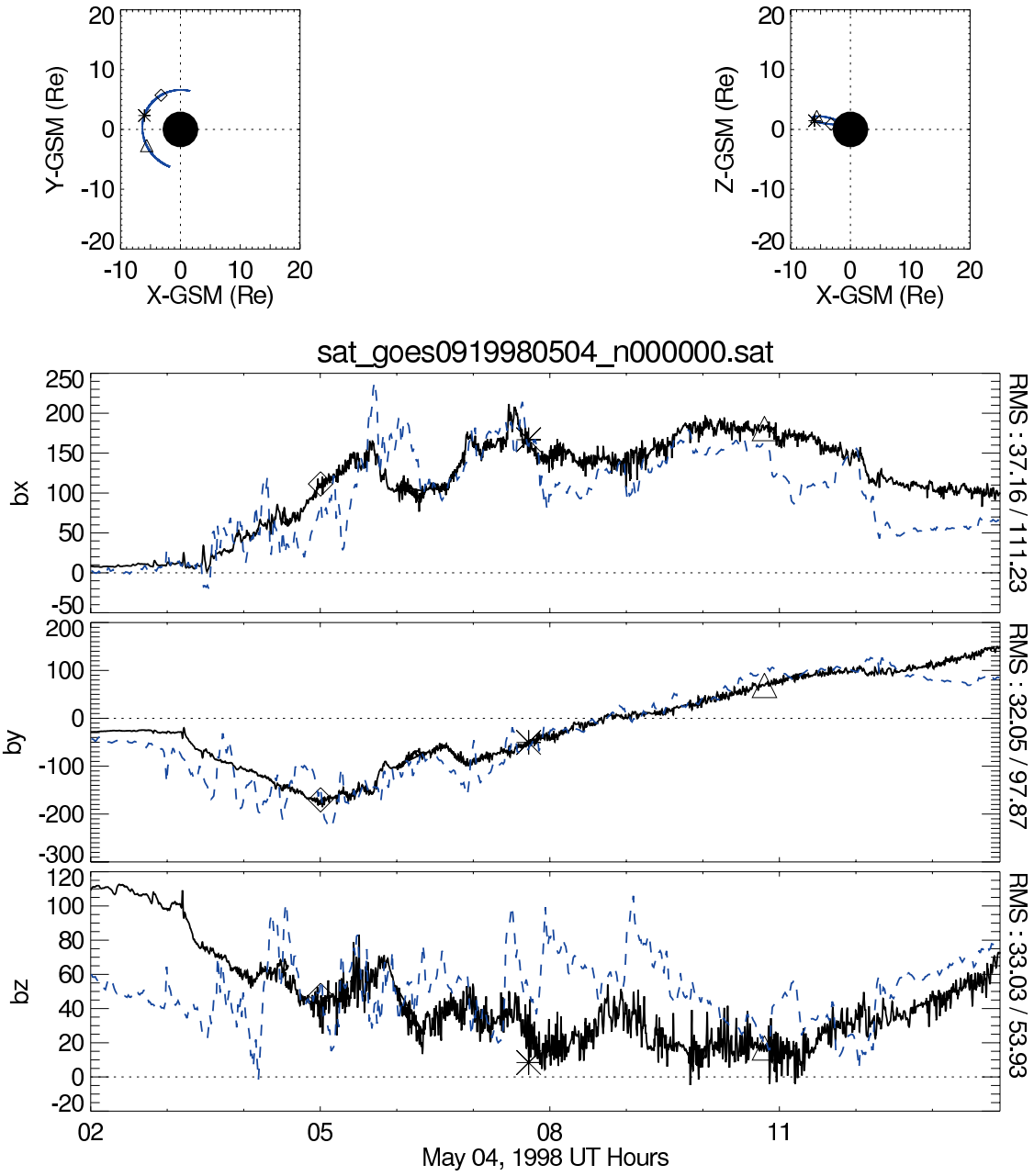

Figure 4.12: Same as Figure 4.3, but for the GM-IM-IE-PW system setup.

4.6 Conclusions

This study demonstrates the capabilities of the SWMF to predict satellite-specific magnetic field, plasma energy distribution, and geosynchronous magnetopause crossings, all for the terrestrial magnetosphere. The model predicts magnetic quantities exceptionally well, even in regions of low resolution. Integrated plasma density and temperature values predicted by the model are near the average measured values. All simulations were completed at near real time run speeds using a limited amount of computing resources, demonstrating the SWMF's operational capabilities.

The coupled codes also proved competent at predicting magnetopause crossings for satellites in geosynchronous orbits. The exceptionally low false alarm rates provide operational users confidence that a modeled crossing nearly always correctly predicts a real crossing. Missed crossings may still be a problem, especially those driven by solar wind pressure pulses. These results must be expanded upon in the future by investigating the crossings with finer time resolution and applying a full signal processing analysis to the binary results as outlined by Jolliffe and Stephenson (2003).

Changing the module combinations used produced interesting results. Although it was expected that the RCM should be a strong factor in the stretching of the inner magnetosphere, it only provided a negligible change in the results. Adding the PW module yielded drastic changes in the results, implying that the ionosphere is an important plasma source in the magnetosphere. These results give operators and scientists insight into the impact that these different codes have on the system and can affect their choice of modules when weighing accuracy versus computational costs.

Several deficiencies need to be addressed in order to improve the results presented

here. The most important problems are the large magnetic reconnection rates, under stretched field lines in the inner magnetosphere, and lack of cold particle sources in the inner magnetosphere. These issues may be treated by improving and expanding upon the physics used in the various models. For example, a non-ideal version of the BATSRUS MHD code that includes the Hall resistive term in the induction equation (Tóth et al., 2008) could be used in place of the version used here in order to improve reconnection physics. Such changes may improve the nRMSE and correlation coefficient scores, but require additional computational resources.

Although sufficient for selecting the model setup used in this study, the results presented in Table 4.2 must be expanded upon. A complete sensitivity study that involves all events and a broader range of parameter settings is required to obtain a robust understanding of the SWMF's performance. The impact of grid layout and resolution is needed as well.

Future work will also include comparisons between SWMF predictions and rudimentary prediction methods and computationally inexpensive empirical codes. Such comparisons test for "skill", or the improvement in quality of one prediction method over another. Such work quantifies the advantage of using the computationally expensive SWMF over other predictive methods.

The results presented here will serve as a baseline to compare to future validation results of similar quantities. This allows model developers to track code performance as the system evolves, and observe the impact new codes have on the coupled system. It also provides operational users with quantitative assessment of the system's performance. This and future studies are vital for scientific and operational users of the SWMF, who need to fully understand the model's capabilities.

CHAPTER V

The Source of Magnetospheric Plasma in the SWMF

5.1 Introduction

The dominant source and entry mechanism for plasma sheet and ring current particles is a topic that has been the focus of many studies over the past several decades. A simplified summary of the debate yields two possible sources: solar wind entry versus ionospheric outflow into the plasma sheet. Two entry paths are considered to deliver mass from these sources to the inner magnetosphere: either vertical transport with convecting magnetic field lines into the plasma sheet then into the ring current region, or flank entry into the plasma sheet through a variety of mechanisms. Unraveling this mystery is of utmost importance to achieve a thorough understanding of the terrestrial magnetosphere.

Early evidence for ionospheric sources came in the form of O^+ measurements in these regions by Shelley et al. (1974). Confirming the first measurements were studies that found O^+ composition increasing during increased solar and magnetospheric activity (e.g. Lennartsson and Shelley (1986); Nosé et al. (2003); Denton et al. (2005)). Others have taken a step further and concluded that ionospheric outflow is indeed the dominant source for sheet and ring current plasma (Chappell et al., 1987). Many of these studies assert that outflowing ionospheric plasma enters the

sheet from above and below as they convect with magnetic field lines (e.g. Chappell et al. (2000)).

Solar wind sources remain a probable alternative, however. Measurements of the boundary layers and plasma sheet (Eastman et al., 1985), especially detections of He^{++} (Lennartsson, 2001), imply plasma from solar wind origins. The entry mechanism is not yet agreed upon, with some presenting data and model work supporting entry through the day side reconnection region (Lennartsson, 2001; Winglee, 2003; Moore et al., 2005), and others supporting flank entry (Eastman et al., 1985; Peroomian and El-Alaoui, 2008).

In this chapter, the sources of plasma in the magnetosphere are examined using two modules with the SWMF: Global Magnetosphere (GM) and Ionospheric Electrodynamics (IE). Simulations of idealized solar wind and magnetospheric conditions are first used to assess the importance of ionospheric and solar wind plasma sources. These results are then tested with simulations of real-world events. Data-model comparisons are performed to evaluate the veracity of the conclusions drawn from the models.

5.2 Methodology

In order to gain a simple, first order understanding of the plasma entry process into the magnetosphere, idealized simulations are carried out utilizing the BATS-R-US code (Powell et al., 1999; De Zeeuw et al., 2000) coupled to a serial ionosphere electrodynamics solver (Ridley and Liemohn, 2002; Ridley et al., 2004) through the SWMF. To simplify these simulations, constant solar wind and IMF are used. Additionally, the dipole axis is aligned with the terrestrial spin axis, removing the effects of the dipole's tilt towards or away from the Sun. The results are analyzed by ex-

amining the magnetospheric configuration, plasma flow paths, and the destination of plasma originating from the solar wind and ionosphere.

Single fluid, ideal magnetohydrodynamics, as outlined in Chapter III, is incapable of distinguishing between plasma of different sources. Because of this, it is necessary to switch from single fluid BATS-R-US to the multispecies version, described in Ma et al. (2002). As opposed to treating the entire plasma population as a single fluid, as in Equations 3.1 through 3.4, the number density is divided into several different species, as defined by the model user. This creates a new set of MHD equations that are solved by the model (Equations 5.1). With a separate continuity equation for each species, the different populations may now be traced through the simulation domain. However, there remains only a single momentum and energy equation, so the solution is still, essentially, single-fluid.

$$
\left(\begin{array}{c}
\frac{\partial \rho_1}{\partial t} + \nabla \cdot (\rho_1 \mathbf{u}) = 0 \\
\vdots \\
\frac{\partial \rho_n}{\partial t} + \nabla \cdot (\rho_n \mathbf{u}) = 0 \\
\rho_{total} = \rho_1 + \rho_2 + \cdots + \rho_n \\
\frac{\partial \rho_{total}\mathbf{u}}{\partial t} + \nabla \cdot (\rho_{total}\mathbf{uu} - \mathbf{BB}) + \nabla p_{total} = 0 \\
\frac{\partial e}{\partial t} + \nabla \cdot (\mathbf{u}e + \mathbf{u}p_{total} - \mathbf{BB} \cdot \mathbf{u}) = 0 \\
\frac{\partial \mathbf{B}}{\partial t} + \nabla \cdot (\mathbf{uB} - \mathbf{Bu}) = 0
\end{array}\right) \tag{5.1}
$$

For the purposes of investigating magnetospheric plasma sources, two proton species are defined in the code: solar wind and ionospheric. At the upstream boundary, the plasma is set to be nearly 100% solar wind protons; at the inner boundary it is 100% ionospheric protons. Each simulation is initialized with pure ionospheric plasma . This setup furnishes an easy assessment of if and how solar wind plasma

enters the magnetosphere.

Figure 5.1 shows the grid layout used in this study. Near-body resolution is $1/8R_E$; geosynchronous satellites reside in the region of $1/4R_E$ resolution. Higher resolution regions are expanded tailwards to better capture tail dynamics. This setup yields approximately 1.9 million grid points.

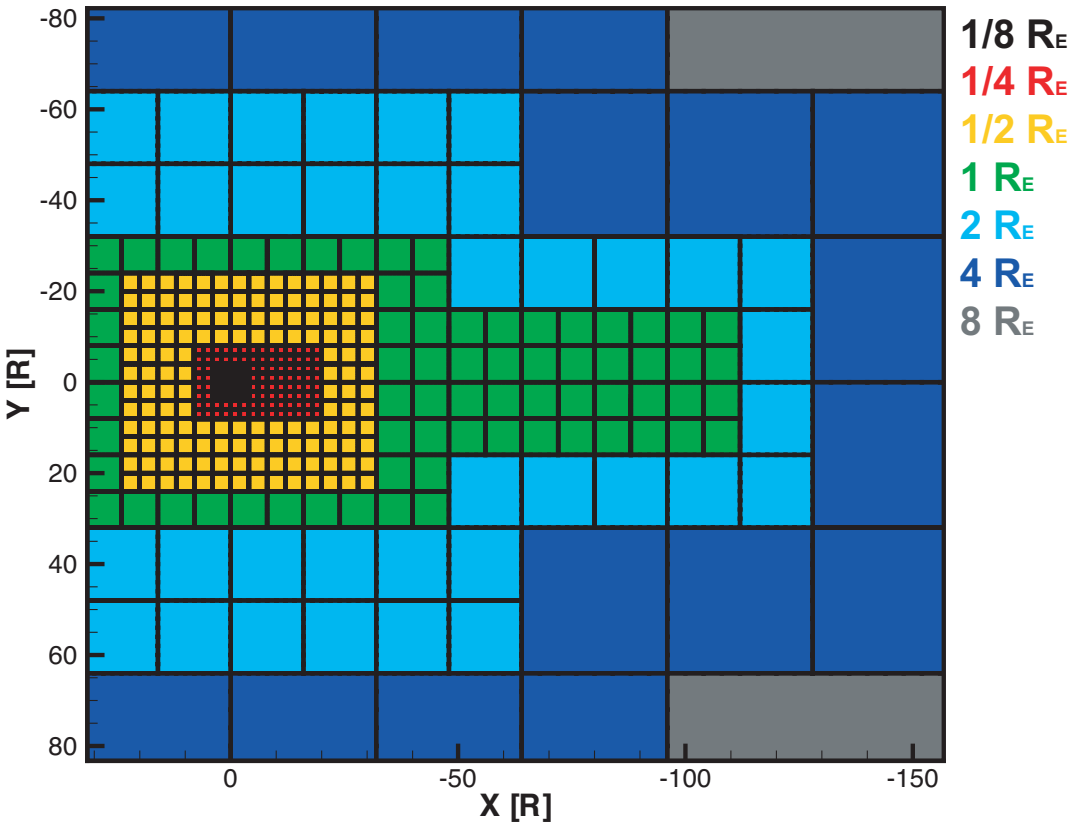

Figure 5.1: The grid used for the BATSRUS code as seen in the Z=0 plane. The grid extends to $\pm 128R_E$ in the Y and Z directions, and from 32 R_E to $-224R_E$ in the X direction. The grid is symmetric such that a slice in the Y=0 plane would look identical to this slice. Resolution is denoted by color and corresponds to the key to the right of the grid.

5.3 Idealized Results

5.3.1 Southward IMF

The first simulation was performed with a constant southward IMF configuration. Solar wind velocity and density was held constant at average values ($450^{km}/_s$ and $8.7cm^{-3}$). Like all simulations in this study, it began with 5000 iterations in local

time stepping mode (Ridley et al., 2002) to accelerate the system to a steady state, then it was allowed to run in time-accurate mode until any lingering, large-scale dynamics settled.

The left frame of Figure 5.2 shows the configuration and content of the magnetosphere during southward ($B_z = 10nT$) IMF conditions in the Y=0, or noon-midnight meridional, plane. The inner boundary is denoted by the black circle of radius $2.5R_E$, and the black lines show the field topology (line density does not necessarily imply field strength). Contours show the percent of plasma that is of solar wind origins (solar wind species from the upstream boundary.)

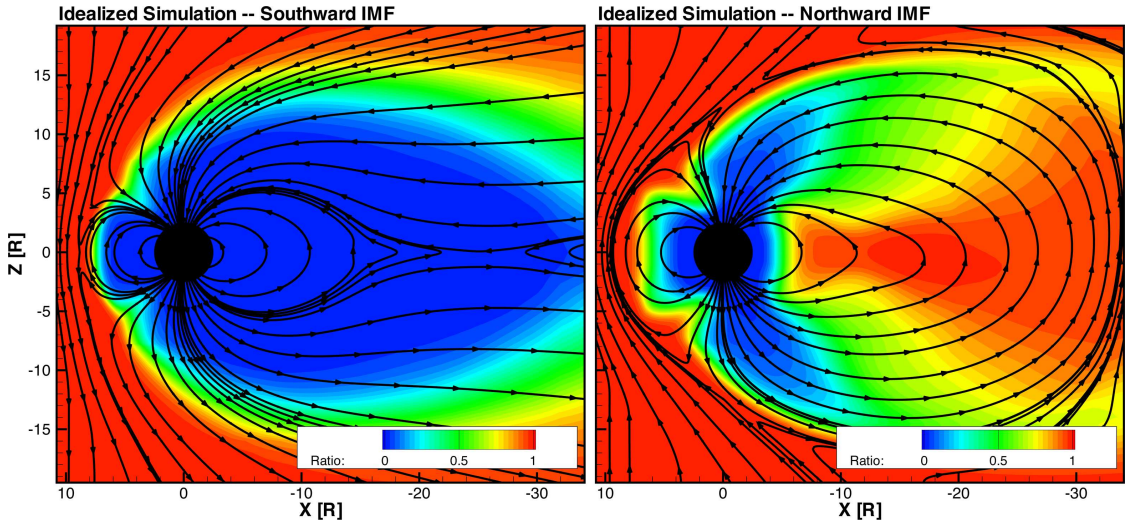

Figure 5.2: Slices of the magnetosphere in the Y=0 (noon-midnight meridional) plane. The dark circle is the inner boundary of the simulation domain (a sphere of $2.5R_E$), black lines show magnetic field configuration. Contours show percent of the plasma that is the solar wind species. Left frame is during southward IMF B_z conditions, the right frame is for northward IMF B_z.

Figure 5.2 demonstrates that there is no solar wind entry into the magnetosphere in the BATS-R-US model during southward oriented IMF. Ionosphere plasma dominates the inner and outer magnetosphere through the plasma sheet well past the tail reconnection point. The solar wind plasma begins to mix along the magnetopause but does not penetrate deeply into the magnetosphere.

Figure 5.3 illustrates how the ionosphere species enters the plasma sheet and ring current regions. This Y=0 slice shows pressure as black contour lines and a single streamline of inner boundary-originating plasma. Color of the streamline shows the temperature of the plasma along its path.

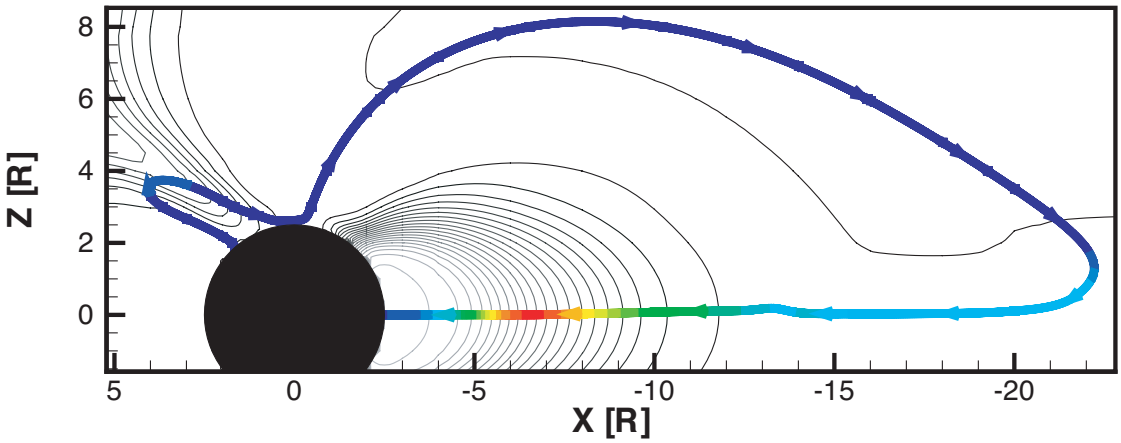

Figure 5.3: A slice of the magnetosphere in the Y=0 plane with a single plasma streamline from the ionosphere to the plasma sheet. The dark contours are equipressure lines. Color along the streamline shows the temperature, in electron volts, of the plasma as it is transported into the tail.

Ionosphere plasma is first sucked away from the inner boundary by pressure gradient forces. This particular path in Figure 5.3 shows the plasma first entering the cusp and then pushed back towards the Earth, again by pressure gradient forces. The plasma then begins to $\mathbf{E} \times \mathbf{B}$ drift with the convecting magnetic field lines towards the night side. Low pressure in the lobes pulls the ionospheric plasma down tail, where it convects towards the plasma sheet. The plasma is heated as it passes near the magnetic x-line, and then further as it moves Earthward adiabatically. At the temperature peak (approximately 17.5keV), the plasma begins to electromagnetically drift perpendicular to the plane of the plot.

Through this motion, ionospheric plasma is brought into the plasma sheet and is heated to contribute to the ring current. Plasma originating equatorward of the streamline displayed in Figure 5.3 escapes down tail; plasma originating poleward

of the streamline shown enters the plasma sheet further Earthward of the magnetic x-line and contributes to the higher latitude plasma sheet. Further detail of this motion is shown in the upper left frame of Figure 5.4, explained in detail below.

5.3.2 Northward IMF

The first idealized simulation was repeated, but at the four hour mark, the IMF B_Z orientation was flipped from -10nT to +10nT. The magnetospheric configuration and plasma content after large scale dynamics settled are shown in the right frame of Figure 5.2. The topology is what is expected for the solar wind drivers: reconnection over the cusps adds magnetic flux to the day side and the tail region is inflated. In stark contrast to the southward IMF case, solar wind plasma has entered several regions in the magnetosphere where it was not found before. Most importantly, solar wind protons dominate the plasma sheet density.

Figure 5.4 compares and contrasts the two cases to help explain the differences in plasma sources. Contours again show plasma content, but the dark lines now show flow streamlines. The left column presents the southward IMF case, while the right column presents the northward case. Plots in the top row are cuts of the magnetosphere in the Y=0 plane (same as Figure 5.2) and there are tremendous differences between flow patterns in this plane for the different solar wind drivers. The upper left frame expands upon the plasma flow illustrated in Figure 5.3.

These flow patterns are what is expected when magnetospheric convection of field lines as described by Dungey (1961) is superposed with plasma motion parallel to the field lines. Recall from Chapter I that the Dungey paradigm for convection is the flow of field lines away from the day side reconnection point to the night side reconnection zone, then from the night side reconnection region back Earthwards, and eventually returning to the day side. The path takes the field lines directly over (under) the

north (south) pole, then equatorward as the field lines are brought together in the plasma sheet. This flow combined with the outflowing of the ionospheric plasma is equivalent to the flow description of Figure 5.3 and can occur only during southward IMF conditions.

The flow pattern changes drastically for the northward IMF case (upper right frame of Figure 5.4). In the now predominately solar wind tail, flow lines diverge from a flow reversal region that is spatially larger and nearer to the Earth than what is seen in the southward IMF case. Patterns no longer reflect that of what would be expected in a "Dungey-type" magnetosphere.

Plots in the bottom row are cuts in the equatorial plane (Z=0) and further explain the dynamics seen in the top row. For the southward IMF case (bottom left frame), the plasma sheet and inner magnetosphere are flanked by large flow vortices. These vortices are driven by numeric diffusion of particles and momentum across the magnetopause and allow mixing of the two species defined in the model. Such features are indicative of viscous interaction between the magnetosphere and the solar wind populations, driving magnetosphere convection- a mechanism first proposed by Axford and Hines (1961). Although these vortices are important, they are not the dominant convection method for the southward IMF case. Dungey-type convection brings in the majority of central plasma sheet and ring current material into the tail from the top and bottom, not the sides. When this mechanism is shut off, as in the case of the northward IMF simulation (lower right frame), Axford and Hines (1961) convection becomes the dominant driver in the magnetosphere. The vortices are now capable of bringing in the solar wind species, which dominates the plasma sheet and ring current regions. This source becomes so important in the simulation that the only ionosphere-source plasma found in the equatorial plane is a tightly defined,

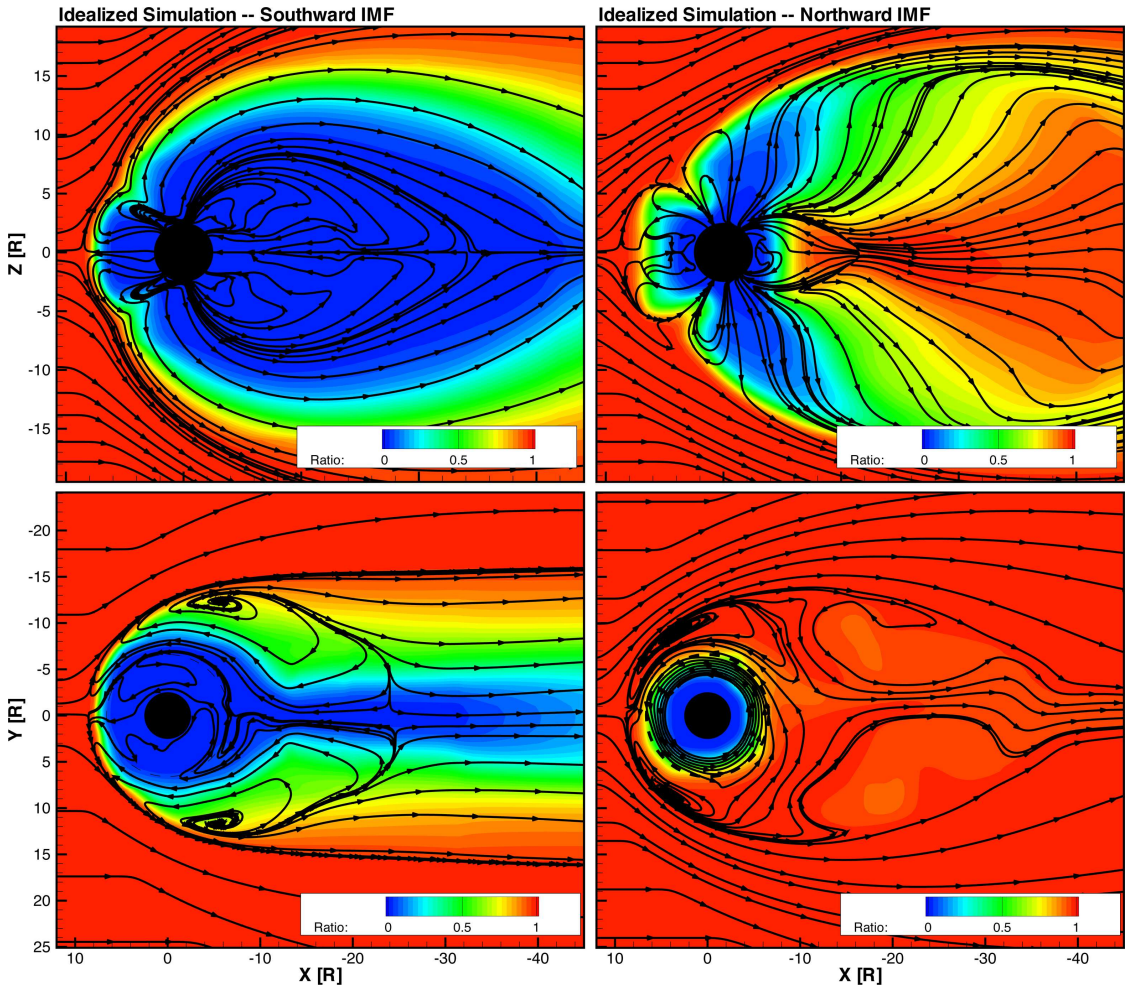

Figure 5.4: Slices of the magnetosphere in the Y=0 (top row) and Z=0 (equatorial, bottom row) planes. Contours show percent of plasma that is solar wind species. Black lines show plasma streamlines. The left column is during southward IMF B_z conditions, the right is for northward IMF B_z.

corotating plasmasphere.

The differences arising from the different driving mechanisms are seen in the ionosphere as well. Ionospheric radial current and potential patterns for each IMF configuration is seen in Figure 5.5. The top row results from the southward IMF simulation, bottom from the northward IMF case. Field-aligned currents are on the left and electric potentials on the right. During the negative B_Z periods, the SWMF produces the expected two-cell potential pattern and region-1 field aligned currents (Dungey, 1961; Iijima and Potemra, 1976; Lester et al., 2006). For northward IMF, a

four-celled potential pattern emerges where the poleward pair is reversed in polarity compared to the southward IMF case. This convection pattern is the well known NBZ pattern (named for its association with northward IMF conditions) (Burke et al., 1979; Iijima et al., 1984; Reiff and Heelis, 1994; Huang et al., 2000). The lower latitude field aligned currents map to the viscous-driven flow vortices seen in Figure 5.4. The SWMF's ability to clearly reproduce well known features in the magnetosphere for both IMF orientations lends support to the results of the idealized runs.

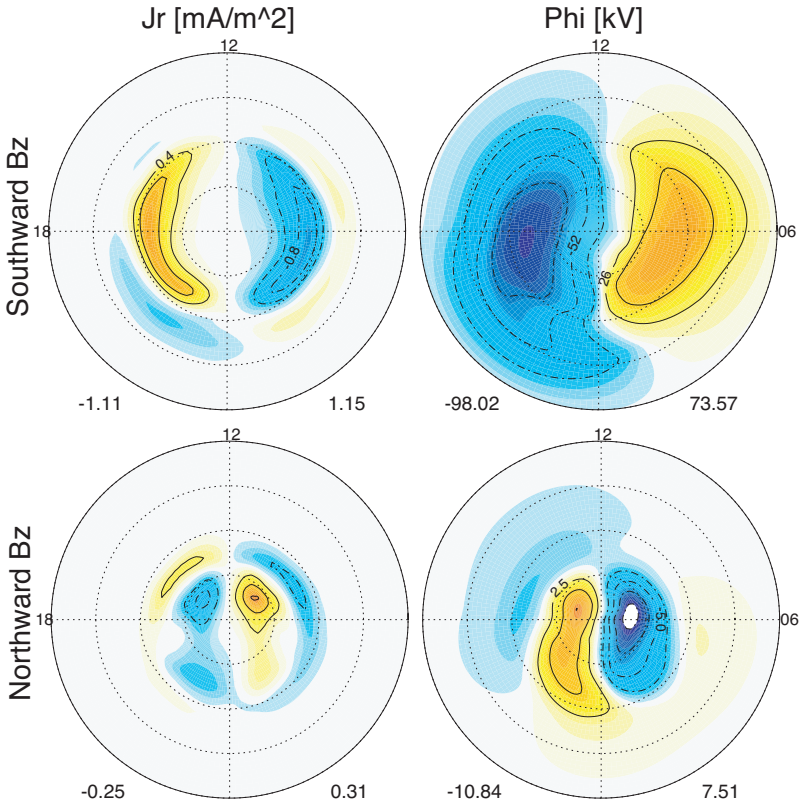

Figure 5.5: Ionospheric maps of radial field-aligned current (left column) and potential patterns (right column) for southward and northward IMF B_Z conditions. Yellow contours are positive values, blue are negative. Maximum and minimum values for each plot are shown to the lower right and left of the circle.

Changes in the plasma sheet due to IMF configuration are illustrated in Figure 5.6. The top frame is a time series of plasma temperature at Z=-7R_E, the bottom frame

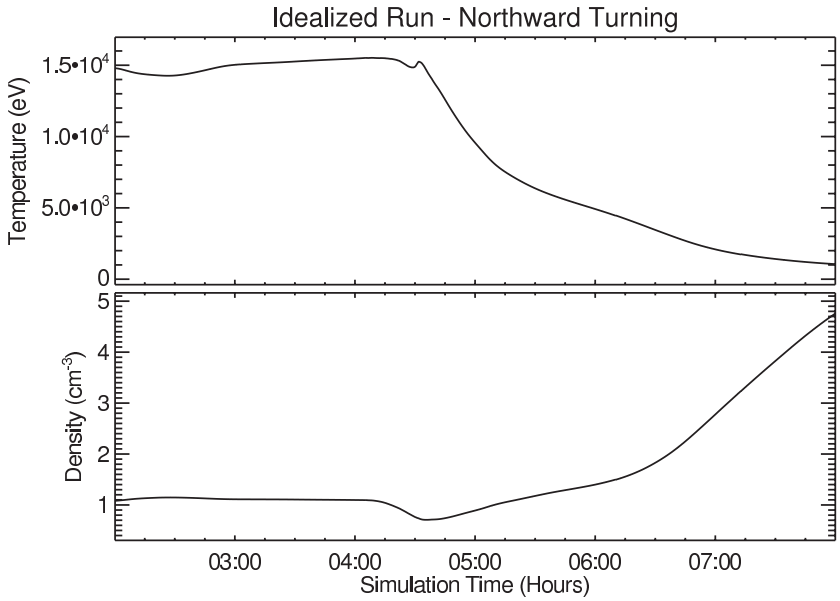

Figure 5.6: Time profile of temperature and density at $7R_E$ down tail. At 4 hours into the simulation, IMF B_Z turns southward to northward.

is the same but for number density. Before the northward turning, the ionosphere plasma is well heated because it enters near the magnetic x-line and must travel the length of the tail, adiabatically heating for the duration of the trip. After the IMF northward turning, which occurs four hours into the simulation, solar wind plasma enters through the flanks (as demonstrated in Figure 5.4). This plasma is significantly cooler because it experiences much less adiabatic heating by the time it reaches the point of measurement. This mechanism also brings in more plasma than its Dungey (1961) counterpart, creating a cold, dense plasma sheet, another well studied feature of the magnetosphere (Lennartsson and Shelley, 1986; Lennartsson, 1992; Terasawa et al., 1997; Fujimoto et al., 1998; Phan et al., 2000; Huang et al., 2002) which has been established as consisting of solar wind plasma (Lennartsson, 1992; Fujimoto et al., 1998).

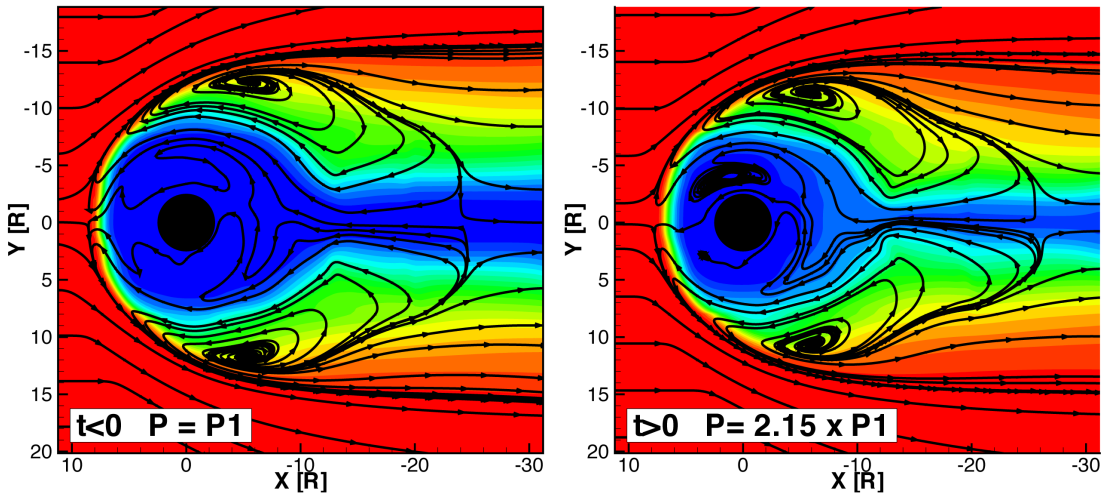

Figure 5.7: Equatorial cuts of the magnetosphere showing content and plasma streamlines, similar to Figure 5.4. The left frame shows the magnetosphere before the pressure increase ($t < 0$), while the right frame shows the magnetosphere afterwards ($t > 0$). The pressure increases by a factor of 2.15.

5.3.3 Pressure Effects

To test the effects of changing dynamic pressure on plasma sources, the southward IMF simulation was repeated, but the solar wind number density was increased from $8.7cm^{-3}$ to $18.7cm^{-3}$, raising the dynamic pressure by a factor of 2.15. The increase occurred over the span of one minute, similar to short time scale pressure pulses observed in the solar wind that often signifies the onset of a magnetic storm. Again, the simulation was allowed to settle after the pressure pulse.

Figure 5.7 shows slices of the magnetosphere taken in the equatorial plane both before and after the pressure increase. As in the bottom row of Figure 5.4, the contour shows the percent of the plasma that is of solar wind origins. The left frame displays the now familiar configuration of the magnetosphere during southward IMF, where both reconnection and viscous interaction driven convection are acting on the magnetosphere. The right frame shows the configuration after the pressure increase. The flank vortices have grown in size and have constricted the inner magnetosphere as

well as the central plasma sheet, which is still drawing in ionospheric plasma through night side reconnection. This is due to the solar wind dynamic pressure constricting the size of the magnetosphere as well as the increase in solar wind momentum, which strengthens the vortices. As the vortices are forced towards the center of the plasma sheet, solar wind plasma begins to diffuse into Earthward flow, mixing with ionosphere plasma. This demonstrates that the two modes of driving are in a constant balance that depends on dynamic pressure and $-B_Z$ driven reconnection.

Figure 5.8 demonstrates the effect on the central plasma sheet temperature and density $7R_E$ down tail. Similar to the effects on the plasma sheet due to a northward turning of the IMF, flank delivery of solar wind plasma increases the density and decreases the temperature. This feature is not nearly as strong as what is seen in Figure 5.6 because the IMF remains southward and thoroughly heated ionospheric plasma is still dominant. The results here provide an explanation for the observations of Thomsen et al. (2003), who found that cold, dense plasma sheet material could penetrate the inner magnetosphere by means of a solar wind pressure pulse.

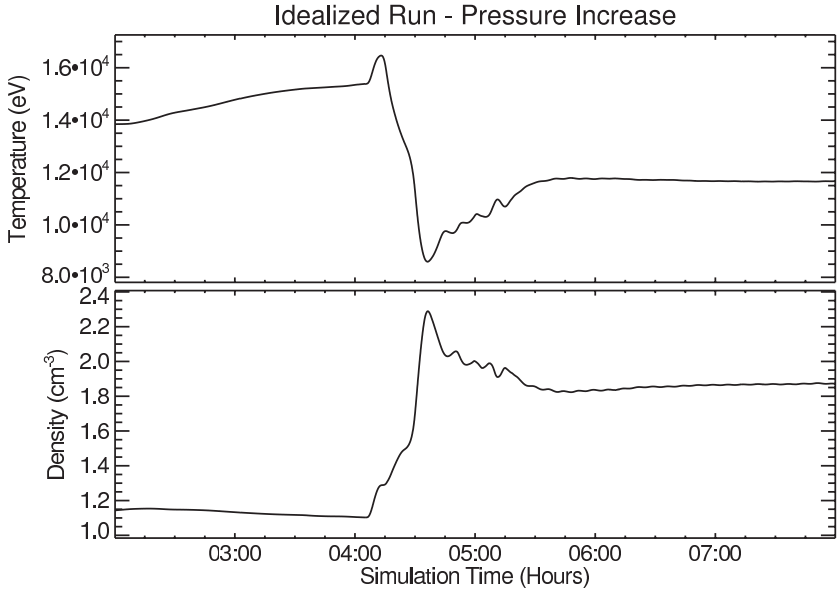

Figure 5.8: Same as Figure 5.6, but for the pressure increase simulation. The pressure increases sharply at 4 hours into the simulation.

5.4 Event Analysis

5.4.1 August 4, 2001

The first real world event to be studied is August 4, 2001, spanning from 12:00 UT to the end of the day. The solar wind conditions as measured by the ACE spacecraft used to drive the simulation are shown in Figure 5.9. This event features a nearly constant -4nT IMF B_Z (center frame of Figure 5.9) for the first nine hours, at which point it slowly rotates northward. The number density and velocity (bottom two frames of Figure 5.9) both decrease smoothly and slightly during the first four hours, reducing the dynamic pressure of the solar wind during this period. The solar wind is reasonably steady and this would not be considered "stormy" space weather conditions.

The results of the simulation are summarized in Figure 5.10 that shows three plots of the magnetosphere similar to those shown in Figure 5.2. The results of this event agree with the entry mechanisms predicted by the idealized runs. Early in the simulation, solar wind conditions favor viscous driving and some solar wind plasma gets into the plasma sheet through the flanks (top frame of Figure 5.10, taken at 13:50 UT). This effect is diminished as the solar wind dynamic pressure is reduced (center frame of Figure 5.10, 18:30 UT). After this time, as the B_Z component of the IMF turns northward, flank entry of solar wind plasma is detected (bottom frame of Figure 5.10, 23:00 UT). Overall, the additional complexities of real world drivers and terrestrial field tilt provided minimal changes to the conclusions of the idealized simulations.

During this time period, there are two Los Alamos National Laboratory (LANL) geosynchronous science satellites that pass through the night side of the magnetosphere. This location is where the ring current and plasma sheet region overlap,

making it a key area to investigate the source of ring current and inner magnetospheric plasma. The results of the simulation are compared against data coming from the Magnetospheric Plasma Analyzer (MPA) instrument aboard these satellites. The MPA instruments are electrostatic analyzers that measure the energy-per-charge distribution. Temperature and density moments are calculated from this data for two energy windows: "cold" (0-100eV for protons, 0-30eV for electrons) and "hot" (100eV or 30eV up to 45keV). The cold and hot moment densities are added together to produce a total plasma mass density and pressure. These values are easily comparable to results from the BATS-R-US model.

Figure 5.11 shows the data-model comparisons along the two LANL spacecraft trajectories. The left column is the comparison for the 1991-080 spacecraft, the right column for the 1994-084 satellite. The satellite's position is shown in the top row, with proton number density and pressure given in the next two rows. The blue dashed lines are in-situ measurements; black lines are simulated values. While the satellites are on the night side of the magnetosphere, density values show excellent agreement. MHD pressure is consistently too low, but comes close to the measured pressure when the satellites are nearest to local midnight. The only exception to both of these results is during a brief moment of very cold, dense plasma, simultaneously observed by both satellites near 13:00 UT. As the 1991-080 satellite reaches the day side, both measured and simulated number densities increase, but the MHD density becomes almost twice as much as the measured. The too large of densities on the day side, as well as the low pressure on the night side, are persistent features of MHD results. The latter is a result of insufficient adiabatic heating due to the under stretched (hence, shorter) tail in BATS-R-US as discussed in Chapter IV. The former feature will be discussed later.

The excellent agreement with both satellite measurements while in the plasma sheet region demonstrates that the amount of plasma present is predicted very well by the BATS-R-US model. While this data set does not give an indication of whether the plasma is of ionospheric or solar wind origin, the fact that the MHD code appears to model the density correctly gives credence to the mechanisms observed in the simulations. It demonstrates that the results from the idealized and real-world simulations are reasonable representations of the magnetosphere.

To determine the source of the plasma, ion composition of the plasma sheet is required. For example, the presence of oxygen indicates ionospheric origins. The MPA instrument does not differentiate ion type, but oxygen content can be inferred from the moment data. The process, detailed by Denton et al. (2005), begins with the simple statement of charge neutrality given in Equation 5.2, where N_{HE} is the hot electron density moment. Equation 5.2 neglects other ions and assumes that the hot electron and ion populations are much denser than the cold populations. From the calculation of the velocity distribution function (Thomsen et al., 1999), the contribution to the total number density by ions of mass m_i is $\sqrt{m_p/m_i}$ (1/4 for singly ionized oxygen). Hence, the hot proton density moment, N_{HP}, is given by Equation 5.3. Combining Equations 5.2 and 5.3 yields Equation 5.4. When the MPA instrument indicates the presence of O^+, the plasma has an ionospheric component, while when there is no O^+ content, there is likely little ionospheric content.

$$N_{HE} = N_{H^+} + N_{O^+} \tag{5.2}$$

$$N_{HP} = N_{H^+} + N_{O^+}/4 \tag{5.3}$$

$$\frac{N_{O^+}}{N_p} = \frac{4\,(N_{HE} - N_{HP})}{(4N_{HP} - N_{HE})} \tag{5.4}$$

For this calculation to be valid, the ratio of cold to hot density moments (N_{LP}/N_{HP}, where N_{LP} is the low temperature proton density moment) must be negligible. Additionally, away from local midnight, electrons are shielded from the inner magnetosphere (Korth et al., 1999) and the quasi-neutrality assumption breaks down. Hence, this ratio is only valid within a few hours of local midnight. Despite these restrictions, this method for inferring O^+ in the plasma sheet allows further verification or rejection of the BATS-R-US results.

The only useful data set for this analysis during the August, 2001 event is from the 1994-084 satellite. The results are shown in Figure 5.12; the top frame shows the N_{LP}/N_{HP} ratio and the bottom frame shows the N_{O^+}/N_{H^+} ratio. The inference is valid in the region denoted by the yellow window, which is centered over local midnight and stretches one hour local time in each direction, and when the N_{LP}/N_{HP} ratio is much less than one. During these times, the N_{O^+}/N_{H^+} reaches $\sim$30%, demonstrating ionospheric origins of the plasma sheet material. As described above, during this time period, the MHD code indicated that the plasma sheet was dominated by ionospheric plasma. This analysis indicates that the results of the simulation reasonably reflect the real world processes.

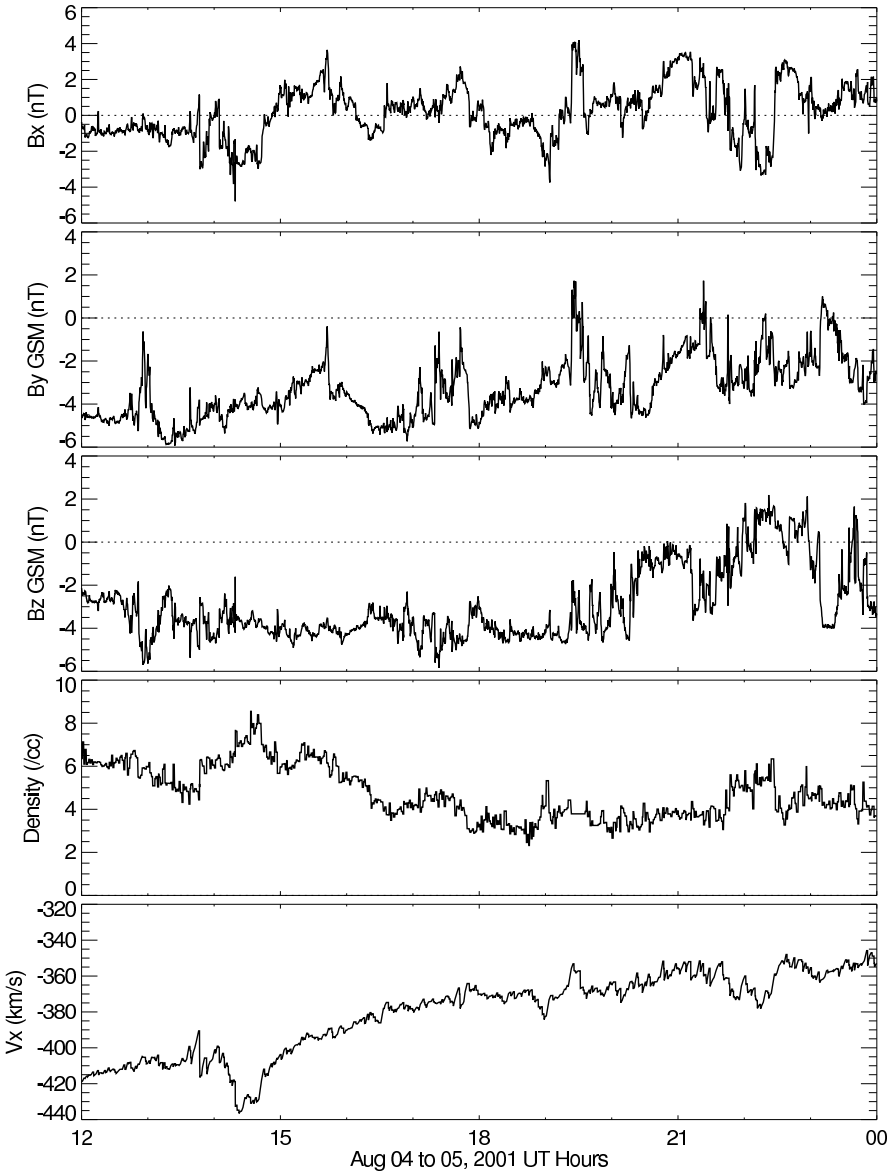

Figure 5.9: Solar wind drivers for the August 4, 2001 event study. The frames, from top to bottom, display the three components of the IMF, proton number density, and flow velocity in the X direction, where negative values indicate Earthward flow. All values were observed by the ACE spacecraft and time shifted from the L1 point to the upstream boundary of the simulation's spatial domain.

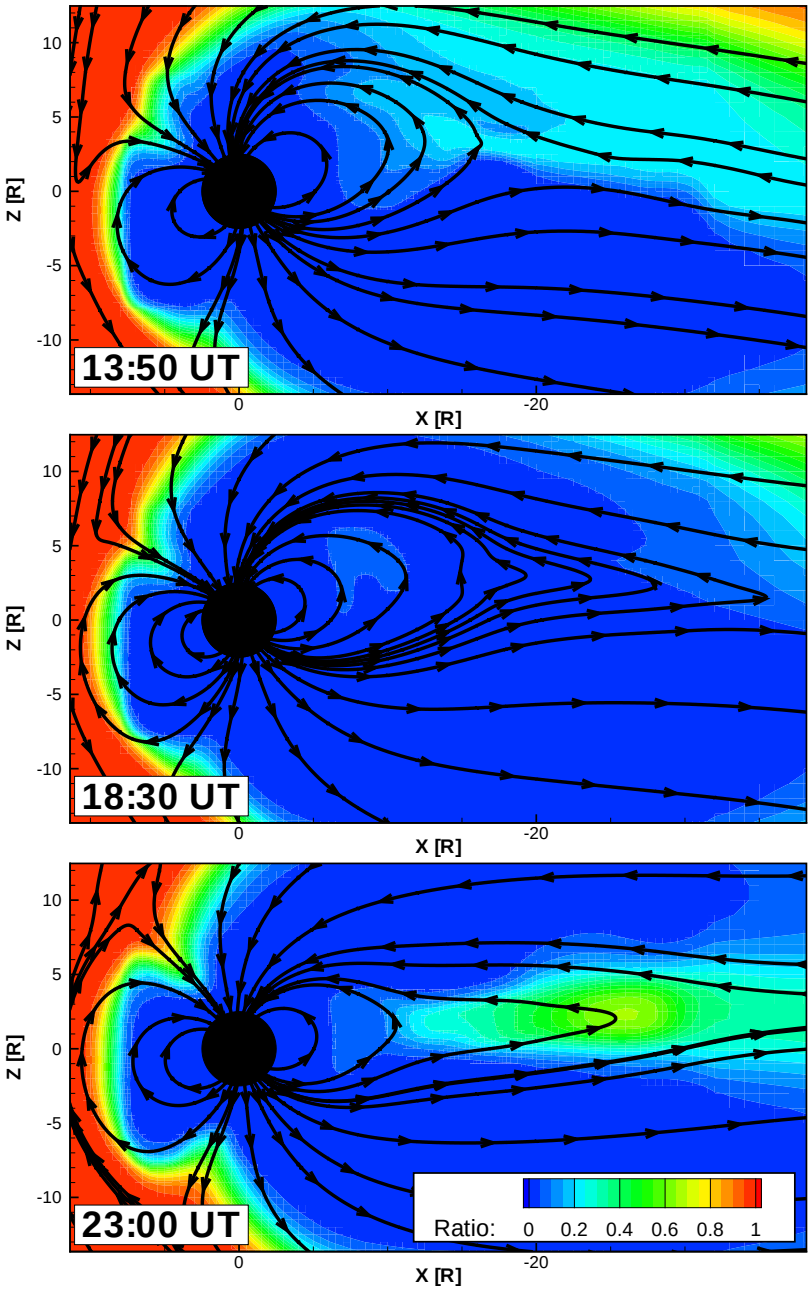

Figure 5.10: Y=0 slices of the magnetosphere showing content and field lines (similar to Figure 5.2) from three separate epochs during the August 4, 2001 event.

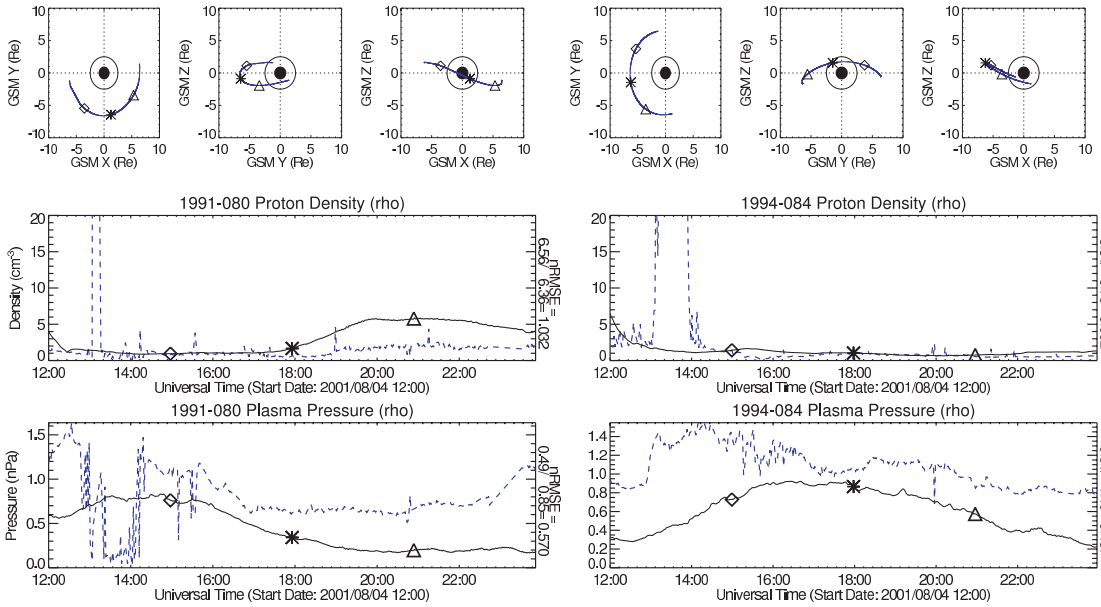

Figure 5.11: Data-model comparisons for the August 4, 2001 event. The left column is the comparisons for the LANL 1991-080 geosynchronous satellite, the right is for the 1994-084 satellite. The top row shows the position of the satellite in the Z, X, and Y=0 planes. Markers in the position plots correspond to the markers in the plots below. The middle and bottom rows show number density and plasma pressure comparisons. Blue dashed lines are in-situ measured data, black lines are results from the simulations.

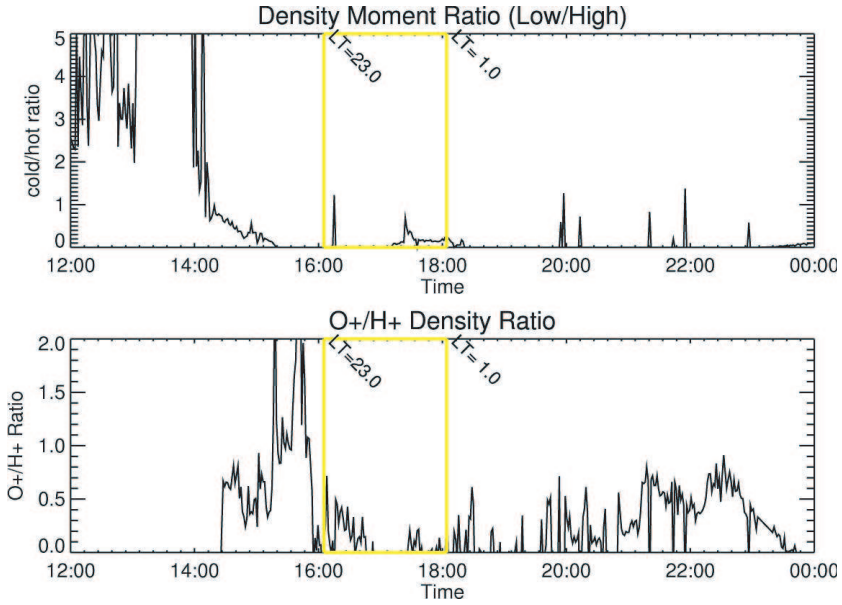

Figure 5.12: Plasma content information from the 1994-084 satellite. The top frame shows the ratio of cold (0-100eV) to hot (0.1-45keV) plasma density. The bottom frame shows the ratio of inferred oxygen to hydrogen number density. The inferred oxygen content is only considered valid when the cold to hot density ratio is very low and when the satellite is within a few hours of local midnight, a region denoted by the yellow boxes.

5.4.2 September 2, 2004

Figure 5.13 shows the IMF and solar wind conditions for September 2, 2004, which features a persistent, yet weak, northward IMF B_z (top frame) as well as nearly constant number density and velocity (bottom two frames). There are several southward turnings, most notably at 14:15 UT. This event was chosen to investigate the veracity of the northward IMF idealized results.

The results of this simulation are consistent with the idealized results, but the southward turnings throughout the event demonstrate the interplay between the two prevalent driving mechanisms. The left frame of Figure 5.14 shows the configuration and content of the magnetosphere at 14:10 UT, during northward IMF but immediately before the southward turning. Solar wind plasma is prevalent in the plasma sheet, but quickly drains after the turning. An hour later (Figure 5.14, right frame), ionosphere plasma dominates the plasma sheet, only to be quickly replaced as the IMF turns northward again. The two sources are constantly changing the content as the event continues.

This interplay is reflected in data from the LANL-97A satellite, which passes through the night hemisphere during this event. Figure 5.15 shows the data-model comparison for this satellite. At 14:30 UT, the number density drops (center frame, blue line) while the plasma pressure increases (bottom frame, blue line). This behavior is what is expected if what is predicted by the model is correct: for northward IMF, the colder, denser plasma sheet forms through solar wind flank entry, but during even weak southward turnings, ionosphere plasma enters via tail reconnection and is warmed adiabatically to temperatures greater than the flank-entering solar wind plasma.

The model results, seen in Figure 5.15 as the black, solid lines, capture the pressure

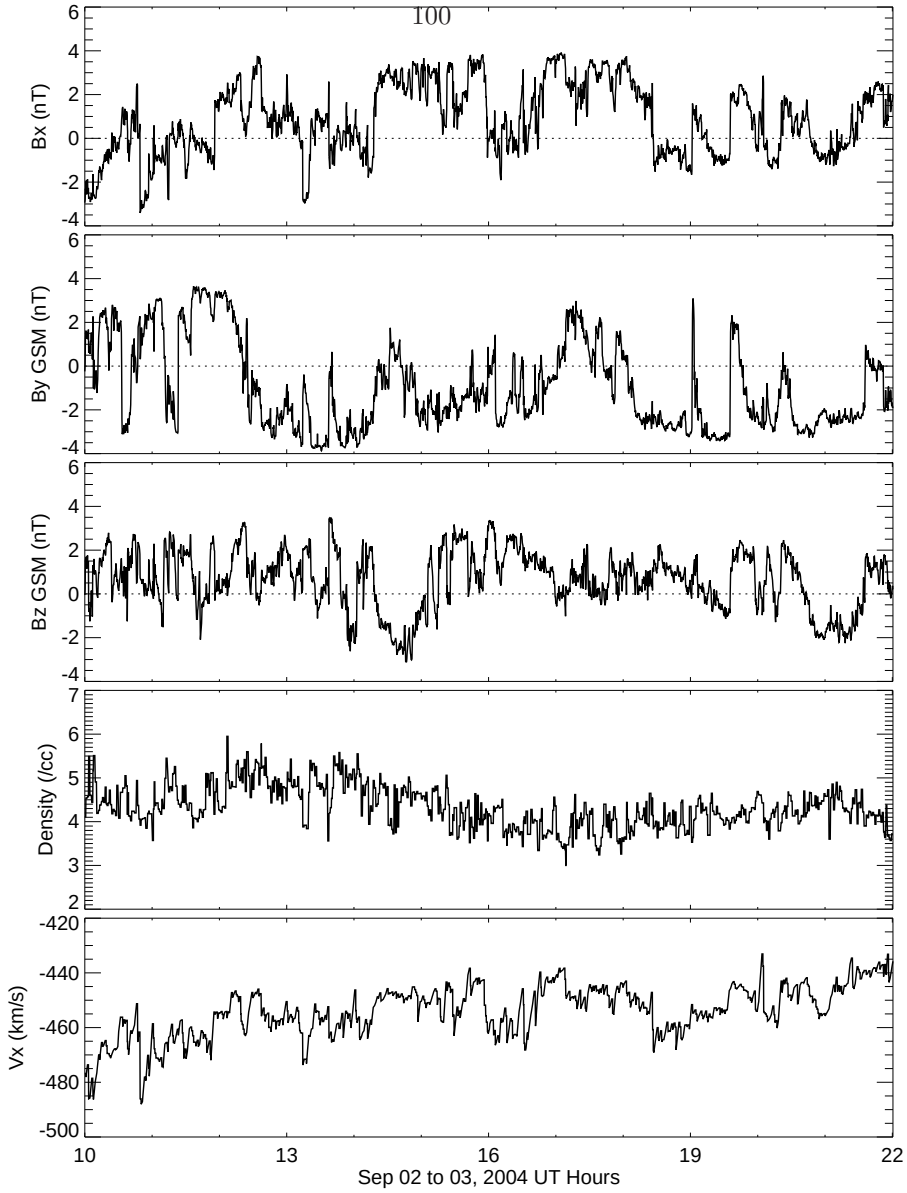

Figure 5.13: The same as Figure 5.9, but for the September 2, 2004 event.

jump but not the density drop. Examining the position of this satellite with relation to the plasma sheet in Figure 5.14, the satellite is just within the boundary of the solar wind dominated plasma sheet, so it does not observe the denser flank plasma during the simulation. Noting that the solar wind dynamic pressure is weaker than what is used in the idealized northward IMF simulation, where flank-entering, solar wind plasma reached deeper into the magnetosphere, it is likely that BATS-R-US is under-predicting the strength of the viscous driving.

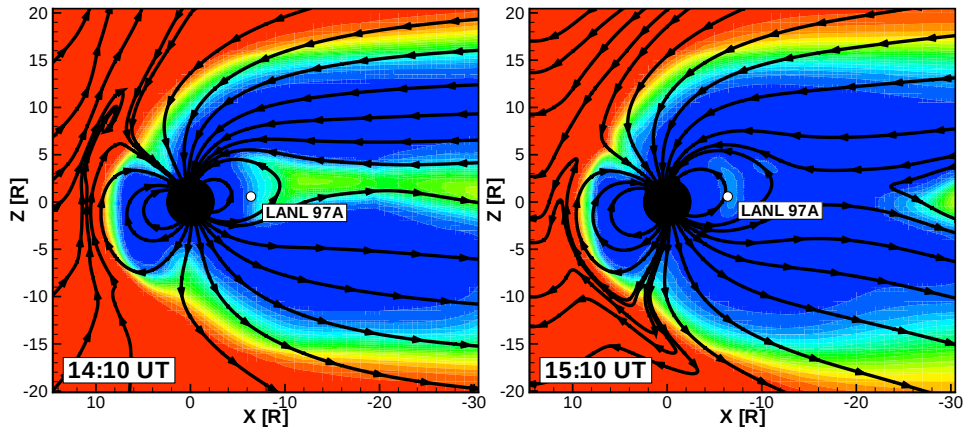

Figure 5.14: Similar to Figure 5.10, but for the September 2, 2004 event. The position of the LANL-97A satellite is shown as the labeled white dot in each frame.

Analysis of possible oxygen content for this satellite is shown in Figure 5.16. The ratio of cold to hot plasma density remains high for most of the run, as expected given the northward IMF conditions. Around 14:30 UT, however, this ratio dives to almost nothing, yielding a narrow time period within the yellow box where a proper inference about the O^+ content of the plasma sheet can be made. During this brief time, N_{O^+}/N_{H^+} reaches $\sim$20%, implying the population is of ionospheric source. These results further support the idealized simulation results.

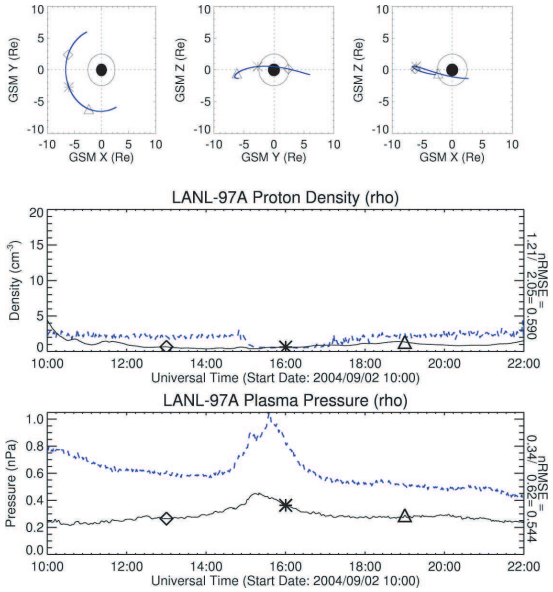

Figure 5.15: The same as Figure 5.11, but for the LANL-97A satellite during the September 2, 2004 event.

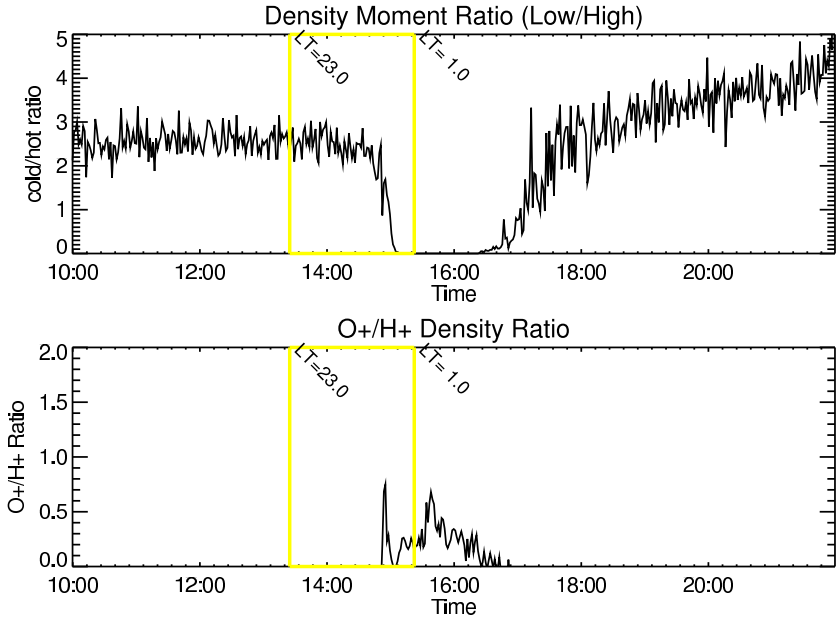

Figure 5.16: The same as Figure 5.12, but for the LANL-97A satellite during the September 2, 2004 event.

5.5 Discussion

The results presented here are supported by previous numerical studies. The ionospheric dominance of the plasma sheet during southward IMF conditions was predicted by Chappell et al. (1987, 2000). Good agreement is found with the true multifluid simulations of Winglee (1998, 2000) for southward IMF cases and solar wind dominance during northward IMF. Huddleston et al. (2005) predicts entry paths for ionospheric plasma into the central plasma sheet via particle tracing routines that qualitatively mirror those shown in Figure 5.3. Peroomian and El-Alaoui (2008) finds flank entry to be an appreciable, but not dominant, entry path for solar wind particles during storm time conditions.

There are important differences found in other investigations, most notably solar wind access to the plasma sheet via day side reconnection. Both Peroomian and El-Alaoui (2008) and Winglee (2003) observe solar wind particles in the plasma sheet that entered from the day side reconnection site in particle tracing results during storm time periods. Moore et al. (2005) finds this to be the dominant source for plasma sheet mass during constant southward IMF conditions when both solar wind and ionospheric source populations are traced through MHD-generated fields. In the results presented here, this entry mechanism is unavailable to the solar wind species.

This difference illustrates a key limitation in the methodology applied here. Because the individual species evolve as a single fluid (they share momentum and energy equations), the outflowing ionosphere plasma acts to shield solar wind plasma from moving Earthward along open magnetic field lines through pressure balance. Mixing of the two species along field lines is controlled by numerical diffusion in the solution of the continuity equations, which is too weak to allow penetration of the solar wind

species to regions Earthward of the magnetic x-line in the central plasma sheet. This may mean that these results are contingent on the inner boundary number density and that a true multifluid simulation would allow an appreciable entry of solar wind plasma through reconnection driven convection.

Figure 5.17 addresses the first of these concerns. The top frame again shows the results for the August 4, 2001 event at the 1991-080 satellite, shown earlier as the center row of Figure 5.11. During this simulation, the inner boundary number density is held constant over the entire boundary at a value of $28cm^{-3}$, which was chosen to balance code stability with realistic conditions. Outflow in the the coupled ionosphere-magnetosphere models occurs by diffusion of mass out of the inner boundary, which is then accelerated by the convection electric field (across field lines) as well as pressure gradients (primarily along field lines). To investigate the effects of reducing the inner boundary density, the value was lowered to $17cm^{-3}$ and the simulation performed again. This number is consistent with what is used in Huddleston et al. (2005) and was generated from surface charging corrected TIDE measurements originally presented by Su et al. (1998). The bottom frame of Figure 5.17 demonstrates that in the night hemisphere, there is no difference between the results when the inner boundary density is changed. The density on the day side is reduced, improving agreement between the data and the model. The species content did not change. Hence, density inner boundary conditions are unimportant to central plasma sheet composition when this simplified outflow is used.

Improved day side results presented in Figure 5.17 for different inner boundary conditions also sheds light on the problem of too high day side number density in BATS-R-US results, discussed in Section 5.4.1. On the day side, the field lines are convecting slowly around the magnetosphere and have ample time to fill with

ionospheric plasma until pressure balance is achieved between plasma in a flux tube and the ionospheric plasma pressure at the flux tube foot point. By lowering the inner boundary density, the foot point pressure is lowered, and equilibrium is achieved at lower densities at equatorial locations. The data-model comparisons at the day side of the magnetosphere in Figure 5.11 demonstrate that, at least for this time period, the density inner boundary condition used are too high. Because ionospheric outflow is dynamic and dependent on solar activity (Yau and André, 1997), dynamic inner boundary conditions could improve results.

As for the second concern, a true multifluid simulation allows for counter-streaming populations, which could potentially allow significant solar wind entry into the central plasma sheet. While some solar wind entry is expected when such a system is used, the initial evidence is that this contribution would be much less than the ionospheric contribution, as demonstrated in Section IV. The consistently under stretched field lines, especially during storm times, imply that the basic outflow generated in the MHD code is under-predicting the actual outflow. When the realistic outflow generated by the PWOM was used in Section 4.5.2, it increased inner magnetosphere pressure, vastly improving the magnetic field results at geosynchronous orbit. It was the increase in the ionospheric source, not the solar wind source, that produced more realistic model results. Effects increasing outflow can be seen by the similar studies of Moore et al. (2005) and Huddleston et al. (2005): both used similar methodologies, but the latter used an increased outflow flux and velocity by re-examining TIDE data and adjusting for spacecraft charging. While Moore et al. (2005) found that ionospheric sources were secondary compared to solar wind sources, Huddleston et al. (2005) found that the ionosphere, using the increased outflow, could easily account for all plasma sheet mass.

Another important difference between these results and others is the predominance of flank entry for northward IMF as opposed to high latitude entry at cusp reconnection points, found in the results of Moore et al. (2005) and Winglee (2000). As seen in the northward IMF results of Figures 5.2 and 5.4, NB_Z-type reconnection is occurring and drawing in solar wind plasma into the day side magnetosphere. However, the flow of this plasma is overcome by the flank vortices, and rather than moving towards the night side, it is swept around the flanks. This may indicate an over prediction of the strength of the viscous driving. It may be argued that the formation of the solar wind dominated boundary layer seen in this study is the result of NBz reconnection and transport as decribed by Song and Russell (1992). Because the layer is present for both northward and southward orientations, it is not likely that the Song and Russell (1992) mechanism is dominant.

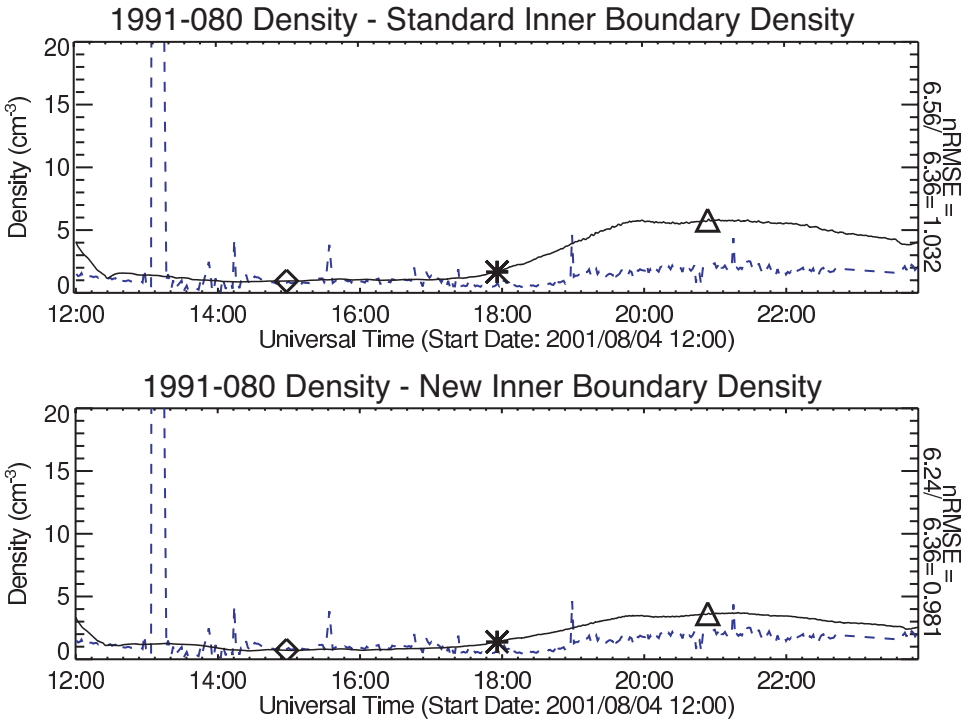

Figure 5.17: Comparisons of number density at geosynchronous orbit for standard BATS-R-US inner boundary density ($28cm^{-3}$) (same as Figure 5.11) and new, realistic inner boundary density ($17cm^{-3}$).

5.6 Conclusions

This study is the first investigation of the source of plasma sheet and inner magnetosphere plasma using purely fluid simulations by means of the multispecies BATS-R-US code. Two species of protons are defined: one for ionosphere sources and one for solar wind sources. Idealized and real events were performed to evaluate the importance of each source as well as the entry mechanism.

Through idealized simulations with steady southward IMF, it was determined that the overwhelming source of plasma in the magnetosphere is ionospheric in origin. The mechanism responsible for bringing this plasma into the plasma sheet is convection of magnetic field lines from the day side to the night side due to reconnection in the subsolar region. Ionospheric plasma trapped along convecting field lines is brought into the plasma sheet, where it adiabatically heats as it moves Earthward along the greater portion of the magnetotail. Concurrently, momentum transfer along the flanks causes large vortices to form. While these voritices allow solar wind plasma to mix with ionosphere plasma along the flanks, no plasma is advected to the central plasma sheet or inner magnetosphere.

Idealized simulations of the magnetosphere being driven by constant northward IMF show that the plasma sheet and ring current regions are dominated by solar wind plasma when the IMF is northward. This is the result of shutting off reconnection driven convection, allowing the flank vortices to become the primary dynamic of the magnetosphere. Flank-entering plasma enters further upstream than the ionosphere plasma that advects vertically into the plasma sheet, resulting in less heating of this population. This leads to a cold, dense plasma sheet with a well defined, corotating plasmasphere that stretches out nearly to geosynchronous orbit.

Varying the dynamic pressure of the solar wind demonstrated that magnetospheric dynamics is a balance between viscous interaction driven and reconnection driven convection. As pressure is increased, flank vortices grow and begin to gain access to the plasma sheet, allowing solar wind plasma to penetrate deeper into the central plasma sheet. The interplay between the strength of these two driving mechanisms ultimately determines the origin, and therefore the temperature and density, of magnetospheric plasma.

Realistic simulations of the August 4, 2001 and September 2, 2004 periods further demonstrate these dynamics under non-steady driving. Data-model comparisons during these events using MPA moment data provide support for these conclusions. Although the plasma temperature is under predicted by the model, number density on the night side of the magnetosphere is captured extremely well. Furthermore, the in-situ measurements reflect what is expected if the model predictions are true: hotter plasma and oxygen content during periods of southward IMF.

This work provides a unifying explanation for many magnetospheric observations:

1. The results allow for entry of both solar wind and ionospheric particles, explaining observations of O^+ (e.g., Shelley et al. (1974)) as well as He^{++} (Lennartsson, 2001), a population associated with solar wind plasma.

2. The long-standing mechanisms proposed by Dungey (1961) and Axford and Hines (1961) are both acting to bring in plasma from different sources, but hang in balance of one another as determined by solar wind conditions.

3. Development of a cold, dense plasma sheet during northward IMF conditions is in agreement with many observations of this phenomena.

4. For northward IMF conditions, the model predicts a four celled ionospheric

convection pattern consisting of a poleward, reverse convection pair and a lower latitude, forward convection pair. This is consistent with the long studied NBZ current system and demonstrates the models ability to correctly predict the state of the ionosphere/magnetosphere. The outer cells map to the viscously driven vortices, which continually drive forward convection.

Future work to addresses these issues and expand upon these findings must begin with an examination of the viscous driving present in the model. While proposing their model for viscous driving, Axford and Hines (1961) asserted that the exact mechanism for these flank interactions is not important, just so long as they exist. At present, this view is reflected in the MHD model because the momentum transfer is due to numerical diffusion along the flanks. While this does not preclude the existence of an actual mechanism, it requires further investigation to ensure that the diffusion rate is representative of real world conditions. Strong discrepancies between model and real-world energy transfer across the flank could have important implications for the interpretation of the model results.

Several other additions to the study will be made in the future to further test these conclusions. This study is limited in the range of events selected, and strong driving and storm time events must be examined. It is likely that such simulations will continue to support this work, as indicated by 4.5.2. Further measurements of plasma sheet content are also needed, especially considering the assumptions taken in the MPA data analysis. Finally, the impact of accurate polar wind outflow on these results must be examined, as this outflow clearly has important implications on the magnetosphere.

CHAPTER VI

Conclusions

This body of work has addressed the three goals stated in Chapter I:

1. Further investigate the connections between the hazards presented by the space environment and anomalous spacecraft behavior.
2. Evaluate the capabilities of the Space Weather Modeling Framework, under the constraints imposed of an operational environment, to predict the state of the magnetosphere at satellite specific locations.
3. Use the validated framework to investigate the critical issue of plasma sources and entry mechanisms into the magnetosphere.

Chapter II addressed the first goal by demonstrating a relationship between lifetime high-energy particle exposure experienced by spacecraft and the likelihood of an operational anomaly occurring. A new metric for assessing particle exposure, "perceived age", was introduced to illustrate the effects of long-term subjection to space weather. Using this metric, it was found that 73.5% of all of the anomalies included in the study had received a disproportionate ($\geq 2\times$) high-energy particle exposure compared to their chronological age. This work is the first statistical study of spacecraft anomalies that takes into account each satellite's lifetime exposure to the space environment.

The results of Chapter II may have important implications for satellite operators. Clearly, a satellite's perceived age must be taken into consideration when evaluating the likelihood of anomaly occurrence. Operators must monitor the lifetime particle exposure experienced by their spacecraft using a combination of in-situ measurements and numerical models.

Chapter IV explored the feasibility of using the SWMF as an operational tool and achieved the second goal of this dissertation. By performing this work in an operational environment (fewer computational resources and real-time run speeds), the SWMF's current operational capabilities have been demonstrated. The validation is the first step towards converting the framework into a now-casting and forecasting system that can be used to predict and mitigate the adverse effects of space weather.

The work outlined in Chapter IV has set many new benchmarks in the field of data-model validation of space weather codes. It is the first comprehensive and systematic validation against in-situ magnetic field and plasma temperature and density using the SWMF and several different module combinations. The capabilities of the framework were also expanded to provide the first satellite-specific full plasma distribution results from the coupled BATS-R-US and RCM codes - an important product for operators wishing to monitor surface charging effects. Finally, the impact of the new polar wind model, PWOM, was presented. Not only did this model vastly improve results for the May 4, 1998 storm, but it also foreshadowed the results of Chapter V.

The validation illustrates the current strengths and weaknesses of the coupled models. Reconnection speeds appear too fast in the results, and the field is far too under stretched. The first issue arises from numerical diffusion in the code allowing the field to reconnect faster than the real world rate. The second results from lower

inner magnetosphere pressure, which is required to push the tail further away from the Earth. Despite these issues, the SWMF captures average values of the magnetic field and plasma properties reasonably well in addition to demonstrating adeptness in predicting dayside magnetopause crossings.

The negligible difference between the metric scores of the RCM/no RCM simulations is frankly disappointing. The addition of this module was believed to improve the BATS-R-US results significantly, but it clearly fails to do so in these validation runs. Operational users may forgo the inclusion of this model in favor of faster simulation completion speeds if energy distribution information is not valuable. Science users may seek to alter the coupling algorithms to increase the strength of the IM feedback on the GM module, or turn to other numerical codes to simulate the IM module.

The third and final goal of this dissertation was reached in Chapter V. The multispecies version of BATS-R-US was used to track ionospheric and solar wind contributions to the magnetospheric particle population during idealized and real-world simulations. The results show that there are two modes for plasma entry. The first is ionospheric outflow that is advected far downtail during reconnection driven magnetospheric convection. The second is viscously-driven flank entry of solar wind plasma. Solar wind pressure and IMF configuration controls which of these two mechanisms is the dominant contributor. Agreement between model results and observations lend credence to the simulation output. This agreement is found both on large scales, such as ionospheric potential patterns and the formation of the cold, dense plasma sheet when expected, and on small scales, as seen in the comparisons with single satellite measurements.

While the topic of magnetospheric plasma sources has been widely studied in the past, the methodology used in this work provides a unique perspective on the problem. It is the first use of the BATS-R-US model and the first use of a multispecies MHD code to address this topic. It is also one of the handful of studies that does not employ particle tracing routines to study entry paths, retaining self consistency. Finally, it is one of the few plasma entry experiments that uses data-model comparisons to test the veracity of the numerical results.

The results of Chapter V combined with those of Section 4.5.2 have important ramifications. Because ionospheric sources play an indispensable role in the SWMF, the gap region cannot be neglected. This is further demonstrated by the improvement in the metric scores produced when realistic ionospheric outflow from the PWOM model is included. It is apparent that accurate magnetospheric modeling requires accurate ionospheric outflow modeling; operational and scientific users striving for high-accuracy results must keep this in mind.

Future work is required to continually test and expand upon the results here, especially the validation work. Additional metrics must be added in order to increase the robustness and create a comprehensive evaluation of the code. Comparisons against baseline results from empirical and unskilled (e.g. persistence) models must be included to calculate the "skill" of the SWMF. The addition of new modules and codes, as is currently being performed with the PWOM, is equally important.

Validation is an interminable process, and steps have already been taken to allow this work to continue with ease. Input and data files have been committed to a validation repository so that the simulations can be reproduced repeatedly. Much of the effort is minimized through automation via computer scripts, also available with the input files. This reduces the calculation of metrics to a single command.

Evaluations of future versions of the SWMF with older ones will be expedited by this automation.

Future steps of the plasma source research will include more simulations, more data comparisons, and more complexities in the modeling methodology. The real world simulations focused on periods of weak to moderate solar wind activity; storm time simulations are needed to test the effects of extreme driving. Data comparisons using instruments that differentiate between ion species must be included to either support or repudiate the results of the MPA comparisons. There are two clear improvements that can be made to the model setup that will have interesting effects on the results. First, addition of the PWOM model will yield results that should be increasingly true to real world conditions. Secondly, switching to a full multi-fluid MHD code is necessary to ensure that no physical processes are neglected by the single fluid approach. These improvements will help to explain the key differences in the results of this study and the results of other computer experiments on magnetospheric plasma entry.

While there are many ways to expand upon most of the work presented, this is not the case for the results of the lifetime exposure study. Additional research of this topic requires a larger database of satellite anomalies. Spacecraft operators and engineers, due to the competitive nature of the industry and fears of increased insurance costs, do not share such databases. For this reason, it is unlikely that any further work to confirm or repudiate the results from Chapter II will occur in the academic arena.

The work presented in the preceding chapters has married operational and scientific approaches to space environment research. Though traditionally separate paradigms, the benefits of interplay between them is illustrated in Chapters IV and

V. The advancement of the validation work provided clues to the source of plasma in the magnetosphere while explaining the low pressure in the dayside results of BATS-R-US. Feedback from the study of the source of plasma in the magnetosphere came in the form of clear knowledge of why PWOM results can improve the metrics. Continuing this relationship can accelerate the creation of beneficial, dependable operational tools and complete understanding of the space environment.

These conclusions also highlight areas of focus as the SWMF is converted to an operational forecasting system. A working module that predicts relativistic particles has become far more necessary given the relationship between lifetime exposure and anomaly occurrence. Given the contribution it makes to the central plasma sheet, polar wind outflow should become a staple of magnetosphere simulations. Improvements to the IM module are required to determine if inclusion of that module is worth the decrease in run speed. Addressing these needs will make the SWMF the most attractive option for space weather forecasting.

BIBLIOGRAPHY

BIBLIOGRAPHY

, ????

Abe, T., Whalen, B. A., Yau, A. W., Horita, R. E., Watanabe, S., Sagawa, E., Jul. 1993. EXOS D (Akebono) suprathermal mass spectrometer observations of the polar wind. J. Geophys. Res. 98, 11191–+.

Akasofu, S.-I., Apr. 1964. The development of the auroral substorm. Planetary Science 12, 273–+.

Amm, O., 1996. Comment on "A three-dimensional, iterative mapping procedure for the implementation of an ionosphere-magnetosphere anisotropic Ohm's law boundary condition in global magnetohydrodynamic simulations". Ann. Geophysic. 14, 773.

Andre, M., Yau, A., Apr. 1997. Theories and Observations of Ion Energization and Outflow in the High Latitude Magnetosphere. Space Science Reviews 80, 27–48.

Ashour-Abdalla, M., Okuda, H., Apr. 1984. Turbulent heating of heavy ions on auroral field lines 89, 2235–2250.

Axford, W. I., 1968. The Polar Wind and the Terrestrial Helium Budget. J. Geophys. Res. 73, 6855–6859.

Axford, W. I., Hines, C. O., 1961. A unifying theory of high-latitude geophysical phenomena and geomagnetic storms. Can. J. Phys./Rev. 39(10), 1433–1464.

Baker, D., Dec. 2000a. The Occurrence of Operational Anomalies in Spacecraft and Thei Relationship to Space Weather. IEEE Transactions on Plasma Science 28 (6), 2007–2016.

Baker, D., Dec. 2000b. The Occurrence of Operational Anomalies in Spacecraft and Their Relationship to Space Weather. IEEE Transactions on Plasma Science 28 (6), 2007–2016.

Baker, D. N., Pulkkinen, T. I., Hesse, M., McPherron, R. L., Apr. 1997. A quantitative assessment of energy storage and release in the Earth's magnetotail. J. Geophys. Res. 102, 7159–7168.

Banks, P. M., Holzer, T. E., 1968. The Polar Wind. J. Geophys. Res. 73, 6846–6854.

Berger, M. J., Colella, P., 1989. Local adaptive mesh refinement for shock hydrodynamics. J. Comput. Phys. 82, 67–84.

Berger, M. J., Jameson, A., 1985. Automatic adaptive grid refinement for the Euler equations. AIAA Journal 32 (4), 561–568.

Borovsky, J., Hesse, M., 2007. The reconnection of magnetic fields between plasmas with different densities: Scaling relations. Plasma Phys. 14, 102309.

Borovsky, J. E., Apr. 1984. The production of ion conics by oblique double layers 89, 2251–2266.

Burke, W. J., Kelley, M. C., Sagalyn, R. C., Smiddy, M., Lai, S. T., 1979. Polar cap electric field structures with a northward interplanetary magnetic field. Geophys. Res. Lett. 6, 21.

Burlaga, L. F., 1995. Interplanetary magnetohydrodynamics. Int. Ser. Astron. Astrophys., Vol. 3, 3.

Cassak, P., Shay, M., 2007. Scaling of Asymmetric Magnetic Reconnection: General Theory and Collisional Simulations. Plasma Phys. 14, 102114.

Chang, T., Coppi, B., Dec. 1981. Lower hybrid acceleration and ion evolution in the suprauroral region 8, 1253–1256.

Chang, T., Crew, G. B., Hershkowitz, N., Jasperse, J. R., Retterer, J. M., Jul. 1986. Transverse acceleration of oxygen ions by electromagnetic ion cyclotron resonance with broad band left-hand polarized waves 13, 636–639.

Chapman, S., Bartels, J., 1940. Geomagnetism. Clarendon, Oxford.

Chappell, C. R., Giles, B. L., Moore, T. E., Delcourt, D. C., Craven, P. D., Chandler, M. O., Apr. 2000. The adequacy of the ionospheric source in supplying magnetospheric plasma. Journal of Atmospheric and Solar-Terrestrial Physics 62, 421–436.

Chappell, C. R., Moore, T. E., Waite, Jr., J. H., Jun. 1987. The ionosphere as a fully adequate source of plasma for the earth's magnetosphere 92, 5896–5910.

Coleman, I. J., Chisham, G., Pinnock, M., Freeman, M. P., Dec. 2001. An ionospheric convection signature of antiparallel reconnection. J. Geophys. Res. 106, 28995–29008.

Cowley, S. W. H., Mar. 1996. A beginner's guide to the Earth's magnetosphere. Earth and Space 8, 9–13.

Cowley, S. W. H., Morelli, J. P., Lockwood, M., Apr. 1991. Dependence of convective flows and particle precipitation in the high-latitude dayside ionosphere on the X and Y components of the interplanetary magnetic field. J. Geophys. Res. 96, 5557–5564.

Damiano, P. A., Lotko, W., Wiltberger, M. J., Lyon, J. G., May 2008. Multi-fluid MHD simulations of solar wind entry into the magnetosphere. AGU Spring Meeting Abstracts, A8+.

De Zeeuw, D., Sazykin, S., Wolf, R., Gombosi, T., Ridley, A., Tóth, G., 2004. Coupling of a global MHD code and an inner magnetosphere model: Initial results. J. Geophys. Res. 109 (A12), A12219, doi:10.1029/2003JA010366.

De Zeeuw, D. L., Gombosi, T. I., Groth, C. P. T., Powell, K. G., Stout, Q. F., 2000. An adaptive MHD method for global space weather simulations. IEEE Trans. Plasma Sci. 28, 1956–1965.

DeJong, A. D., Clauer, C. R., Dec. 2005. Polar UVI images to study steady magnetospheric convection events: Initial results. Geophys. Res. Lett. 32, 24101–+.

Denton, M. H., Thomsen, M. F., Korth, H., Lynch, S., Zhang, J. C., Liemohn, M. W., Jul. 2005. Bulk plasma properties at geosynchronous orbit. Journal of Geophysical Research (Space Physics) 110 (A9), 7223–+.

Drake, J. F., Shay, M. A., 2007. Basic theory of collisionless reconnection. In: Birn, J., Priest, E. (Eds.), Reconnection of Magnetic Fields. Cambridge University Press, New York, NY, pp. 87 – 166.

Dungey, J. W., 1953. Conditions for the occurrence of electrical discharges in astrophysical systems. Phil. Mag. 44, 725–738.

Dungey, J. W., 1961. Interplanetary magnetic field and the auroral zones. Phys. Rev. Lett. 6:47.

Dungey, J. W., 1963. Interactions of solar plasma with the geomagnetic field. Planetary and Space Science 10, 233–237.

Dyer, C., Mar. 2002. Radiation effects on spacecraft & aircraft. In: Sawaya-Lacoste, H. (Ed.), Solspa 2001, Proceedings of the Second Solar Cycle and Space Weather Euroconference. Vol. 477 of ESA Special Publication. pp. 505–512.

Eastman, T. E., Frank, L. A., Huang, C. Y., Oct. 1985. The boundary layers as the primary transport regions of the earth's magnetotail. J. Geophys. Res. 90, 9541–9560.

Fairfield, D. H., Otto, A., Mukai, T., Kokubun, S., Lepping, R., Steinberg, J., Lazarus, A., Yamamoto, T., 2000. Geotail observations of the Kelvin-Helmholtz instability at the equatorial magnetotail boundary for parallel northward fields. J. Geophys. Res. 105, 21159–21173.

Fennell, J. F., Koons, H. C., Roeder, J. L., Blake, J. B., Nov. 2001. Spacecraft Charging: Observations and Relationship to Satellite Anomalies. In: Harris, R. A. (Ed.), Spacecraft Charging Technology. Vol. 476 of ESA Special Publication. pp. 279–+.

Feynman, J., Gabriel, S. B., May 2000. On space weather consequences and predictions. JGR 105, 10543–10564.

Feynman, J., Gu, X. Y., Aug. 1986. Prediction of geomagnetic activity on time scales of one to ten years. Reviews of Geophysics 24, 650–666.

Frahm, R., Winningham, J., Sharber, J. R., Link, R., Crowley, G., Gaines, E. E., Chenette, D. L., Anderson, B. J., Potemra, T. A., 1997. The diffuse aurora: A significant source of ionization in the middle atmosphere. J. Geophys. Res. 102, 28203.

Friis-Christensen, E., Wilhjelm, J., Apr. 1975. Polar cap currents for different directions of the interplanetary magnetic field in the Y-Z plane 80, 1248–1260.

Fujimoto, M., Terasawa, T., Mukai, T., Saito, Y., Yamamoto, T., Kokubun, S., 1998. Plasma entry from the flanks of the near-earth magnetotail: Geotail observations. J. Geophys. Res. 103, 4391.

Galand, M., Fuller-Rowell, T., Codrescu, M., 2001. Response of the upper atmosphere to auroral protons. J. Geophys. Res. 106, 127.

Ganguli, S. B., 1996. The polar wind. Reviews of Geophysics 34, 311–348.

Glocer, A., Gombosi, T., Toth, G., Hansen, K., Ridley, A., Nagy, A., 2007. Polar wind outflow model: Saturn results. J. Geophys. Res., 112.

Goertz, C. K., Shan, L.-H., Smith, R. A., May 1993. Prediction of geomagnetic activity. J. Geophys. Res. 98, 7673–7684.

Gold, T., Sep. 1959. Motions in the Magnetosphere of the Earth 64, 1219–+.

Gombosi, T. I., Aug. 1998. Physics of the Space Environment. Physics of the Space Environment, by Tamas I. Gombosi, pp. 357. ISBN 052160768X. Cambridge, UK: Cambridge University Press, August 1998.

Gombosi, T. I., Cravens, T. E., Nagy, A. F., 1985. A time-dependent theoretical model of the polar wind: Preliminary results. Geophys. Res. Lett. 12, 167–170.

Gombosi, T. I., Kerr, L. K., Nagy, A. F., Cannata, R. W., 1991. Helium in the polar wind. Adv. Space Res. 12 (6), 183–186.

Gombosi, T. I., Nagy, A., 1989. Time-dependent modeling of field aligned current-generated ion transients in the polar wind. J. Geophys. Res. 94, 359–369.

Gombosi, T. I., Tóth, G., De Zeeuw, D. L., Hansen, K. C., Kabin, K., Powell, K. G., 2002. Semi-relativistic magnetohydrodynamics and physics-based convergence acceleration. J. Comput. Phys. 177, 176–205.

Goodman, M. L., 1995. A three-dimensional, iterative mapping procedure for the implementation of an ionosphere-magnetosphere anisotropic Ohm's law boundary condition in global magnetohydrodynamic simulations. Ann. Geophysic. 13, 843.

Gubby, R., Evans, J., 2002. Space environment effects and satellite design. Journal of Atmospheric and Solar-Terrestrial Physics 64, 1723–1733.

Harel, M., Wolf, R. A., Reiff, P. H., Spiro, R. W., Burke, W. J., Rich, F. J., Smiddy, M., 1981. Quantitative simulation of a magnetospheric substorm 1, Model logic and overview. J. Geophys. Res. 86, 2217.

Heelis, R. A., Bailey, G. J., Sellek, R., Moffett, R. J., Jenkins, B., Dec. 1993. Field-aligned drifts in subauroral ion drift events 98, 21493–+.

Hones, Jr., E. W. (Ed.), 1984. Magnetic Reconnection in Space and Laboratory Plasmas.

Horne, R., 2001. Space weather parameters required by the users. Contractor Report WP1300 and WP1400, European Space Agency.

Horwitz, J. L., Singh, N., Nov. 1991. Refilling of the Earth's plasmasphere. EOS, Trans. Amer. Geophys. Union 72.

Huang, C.-S., Foster, J. C., Song, P., Sofko, G. J., Frank, L. A., Paterson, W. R., Feb. 2002. Geotail observations of magnetospheric midtail during an extended period of strongly northward interplanetary magnetic field 29 (4), 040000–1.

Huang, C.-S., Sofko, G. J., Koustov, A. V., Andre, D. A., Ruohoniemi, J. M., Greenwald, R. A., Hairston, M. R., Dec. 2000. Evolution of ionospheric multicell convection during northward interplanetary magnetic field with bz/by greater than 1 105, 27095–27108.

Huddleston, M. M., Chappell, C. R., Delcourt, D. C., Moore, T. E., Giles, B. L., Chandler, M. O., Dec. 2005. An examination of the process and magnitude of ionospheric plasma supply to the magnetosphere. Journal of Geophysical Research (Space Physics) 110 (A9), 12202–+.

Hughes, W. J., Apr. 1995. The magnetopause, magnetotail, and magnetic reconnection. In: Kivelson, M. G., Russell, C. T. (Eds.), Introduction to Space Physics. Cambridge University Press, pp. 227–287.

Hultqvist, B., Nov. 1991. On the motion of electrons in the slow electric field fluctuations observed by Viking 96, 19513–+.

Hundhausen, A. J., 1972. Coronal Expansion and Solar Wind. Springer-Verlag Berlin Heidelberg New York.

Iijima, T., Potemra, T. A., Dec. 1976. Field-aligned currents in the dayside cusp observed by Triad 81, 5971–5979.

Iijima, T., Zanetti, L. J., Bythrow, P. F., 1984. Large-scale Birkeland currents in the dayside polar region during strongly northward IMF: A new birkeland current system. J. Geophys. Res. 89, 7441.

Iucci, N., Levitin, A., Belov, A., Eroshenko, E., Ptitsyna, N., Villoresi, G., Chizhenkov, G., Dorman, L., Gromova, L., Parisi, M., Tyasto, M., Yanke, V., 2005. Space weather conditions and spacecraft anomalies in different orbits. Space Weather 3.

Jolliffe, I., Stephenson, D., 2003. Forecast Verification: A Practitioner's Guide in Atmospheric Science. Wiley, Hoboken, New Jersey.

Kamide, Y., Slavin, J. A. (Eds.), 1986. Solar Wind Magnetosphere Coupling: A.S.S.L.:126, 1986. Vol. 126 of Astrophysics and Space Science Library.

Kivelson, M. G., Apr. 1995. Physics of space plasmas. In: Kivelson, M. G., Russell, C. T. (Eds.), Introduction to Space Physics. Cambridge University Press, pp. 27–57.

Kivelson, M. G., Spence, H. E., Dec. 1988. On the possibility of quasi-static convection in the quiet magnetotail. Geophys. Res. Lett. 15, 1541–1544.

Klumpar, D. M., Peterson, W. K., Shelley, E. G., Dec. 1984. Direct evidence for two-stage (bimodal) acceleration of ionospheric ions 89, 10779–10787.

Koons, H. C., Mazur, J. E., Selesnick, R. S., Blake, J. B., Fennell, J. F., Jul. 1999. The Impact of the Space Environment on Space Systems. NASA STI/Recon Technical Report N, 69036–+.

Korth, H., Thomsen, M. F., Borovsky, J. E., McComas, D. J., Nov. 1999. Plasma sheet access to geosynchronous orbit 104, 25047–25062.

Krause, L., Dichter, B., Knipp, D., Ray, K., Dec. 2000. The Relationship Between DSCS III Sunlit Surface Charging and Geomagnetic Activity Indices. IEEE Transactions on Nuclear Science 47 (6), 2224–2230.

Lennartsson, O. W., Aug. 2001. Ion composition aspects of magnetotail plasma flows. J. Geophys. Res. 106, 15621–15634.

Lennartsson, W., Dec. 1992. A scenario for solar wind penetration of earth's magnetic tail based on ion composition data from the ISEE 1 spacecraft 97, 19221–+.

Lennartsson, W., Shelley, E. G., Mar. 1986. Survey of 0.1- to 16-keV/e plasma sheet ion composition 91, 3061–3076.

Lester, M., Provan, G., Wild, J., Nov. 2006. Review of Ionospheric Effects of Solar Wind Magnetosphere Coupling in the Context of the Expanding Contracting Polar Cap Boundary Model. Space Science Reviews 124, 117.

Loranc, M., St.-Maurice, J.-P., Hanson, W. B., Heelis, R. A., Mar. 1991. A morphological study of vertical ionospheric flows in the high-latitude F region 96, 3627–3646.

Luhmann, J. G., Walker, R. J., Russell, C. T., Crooker, N. U., Spreiter, J. R., Stahara, S. S., Mar. 1984. Patterns of potential magnetic field merging sites on the dayside magnetopause. J. Geophys. Res. 89, 1741–1744.

Lyon, J., Fedder, J., Mobarry, C., 2004. The Lyon-Fedder-Mobarry (LFM) global MHD magnetospheric simulation code. J. Atmos. Sol-Terr. Phys. 66, 1333.

Ma, Y., Nagy, A. F., Hansen, K. C., De Zeeuw, D. L., Gombosi, T. I., Powell, K., 2002. Three-dimensional multispecies MHD studies of the solar wind interaction with Mars in the presence of crustal fields. J. Geophys. Res. 107 (A10), 1282, doi:10.1029/2002JA009293.

Malou, F., Bezerra, F., Salvaterra, G., Chatry, C., Falo, W., David, J.-P., Duzellier, S., Dec. 2002. Total dose and single event effects irradiation of various commercial integrated circuits in logic families and line interfaces. In: Harris, R. A. (Ed.), European Space Components Conference, ESCCON 2002. Vol. 507 of ESA Special Publication. pp. 387–+.

McComas, D. J., Bame, S. J., Barraclough, B. L., Donart, J. R., Elphic, R. C., Gosling, J. T., Moldwin, M. B., Moore, K. R., Thomsen, M. F., 1993. Magnetospheric plasma analyzer: initial three-spacecraft observations from geosynchronous orbit. J. Geophys. Res. 98, 13453.

McComas, D. J., Elphic, R. C., Moldwin, M. B., Thomsen, M. F., 1994. Plasma observations of magnetopause crossings at geosynchronous orbit. J. Geophys. Res. 99, 21,249–21,555.

McPherron, R. L., 1973. Satellite studies of magnetospheric substorms on August 15, 1968 78, 3044–3053.

Miyoshi, Y. S., Jordanova, V. K., Morioka, A., Evans, D. S., Oct. 2004. Solar cycle variations of the electron radiation belts: Observations and radial diffusion simulation. Space Weather 2, 0–+.

Moen, J., Brekke, A., 1993. The solar flux influence of quiet-time conductances in the auroral ionosphere. Geophys. Res. Lett. 20, 971.

Moore, T. E., Fok, M.-C., Chandler, M. O., Chappell, C. R., Christon, S. P., Delcourt, D. C., Fedder, J., Huddleston, M., Liemohn, M., Peterson, W. K., Slinker, S., Feb. 2005. Plasma sheet and (nonstorm) ring current formation from solar and polar wind sources. Journal of Geophysical Research (Space Physics) 110 (A9), 2210–+.

Newell, P., Meng, C.-I., 1992. Mapping the dayside ionosphere to the magnetosphere according to particle precipitation characteristics. Geophys. Res. Lett. 19, 609.

Nosé, M., McEntire, R. W., Christon, S. P., May 2003. Change of the plasma sheet ion composition during magnetic storm development observed by the Geotail spacecraft. Journal of Geophysical Research (Space Physics) 108, 1201–+.

Ö. Sonnerup, B. U., Laird, M. J., Jan. 1963. On Magnetospheric Interchange Instability 68, 131–+.

Papitashvili, V., Rich, F., 2002. High-latitude ionospheric convection models derived from Defense Meteorological Satellite Program ion drift observations and parameterized by the interplanetary magnetic field strength and direction. J. Geophys. Res. 107, 10.1029/2001JA000264.

Parker, E. N., Dec. 1957. Sweet's Mechanism for Merging Magnetic Fields in Conducting Fluids. J. Geophys. Res. 62, 509–520.

Parker, E. N., Nov. 1958. Dynamics of the interplanetary gas and magnetic fields. Astrophys. J. 128 (3), 664–676.

Peroomian, V., El-Alaoui, M., Jun. 2008. The storm-time access of solar wind ions to the nightside ring current and plasma sheet. Journal of Geophysical Research (Space Physics) 113, 6215–+.

Petschek, H. E., 1964. Magnetic Field Annihilation. In: Hess, W. N. (Ed.), The Physics of Solar Flares. pp. 425–+.

Phan, T. D., Lin, R. P., Fuselier, S. A., Fujimoto, M., Mar. 2000. Wind observations of mixed magnetosheath-plasma sheet ions deep inside the magnetosphere 105, 5497–5506.

Pilipenko, V., Yagova, N., Romanova, N., Allen, J., 2006. Statistical relationships between satellite anomalies at geostationary orbit and high-energy particles. Advances in Space Research 37, 1192–1205.

Pirjola, R., Kauristie, K., Lappalainen, H., Viljanen, A., 2005a. Space weather risk. Space Weather 3.

Pirjola, R., Kauristie, K., Lappalainen, H., Viljanen, A., 2005b. Space weather risk. Space Weather 3.

Powell, K., Roe, P., Linde, T., Gombosi, T., De Zeeuw, D. L., 1999. A solution-adaptive upwind scheme for ideal magnetohydrodynamics. J. Comp. Phys. 154, 284–309.

Raeder, J., McPherron, R., Frank, L., Kokubun, S., Lu, G., Mukai, T., Paterson, W., Sigwarth, J., Singer, H., Slavin, J., 2001. Global simulation of the Geospace Environment Modeling substorm challenge event. J. Geophys. Res. 106, 281.

Reiff, P. H., Heelis, R. A., Mar. 1994. Four cells or two? Are four convection cells really necessary? 99, 3955–3959.

Reiff, P. H., Spiro, R. W., Hill, T. W., Sep. 1981. Dependence of polar cap potential drop on interplanetary parameters. J. Geophys. Res. 86, 7639–7648.

Richmond, A., Kamide, Y., 1988. Mapping electrodynamic features of the high-latitude ionosphere from localized observations: Technique. J. Geophys. Res. 93, 5741–5759.

Ridley, A., 2005. A new formulation for the ionospheric cross polar cap potential including saturation effects. Ann. Geophys.

Ridley, A., 2007. The magnetosphere and ionosphere during sub-alfvénic solar wind conditions. Ann. Geophys. 25, 533.

Ridley, A., Gombosi, T., De Zeeuw, D. L., 2004. Ionospheric control of the magnetospheric configuration: Conductance. Ann. Geophys. 22, 567–584.

Ridley, A. J., De Zeeuw, D. L., Gombosi, T. I., Powell, K. G., 2001. Using steady-state MHD results to predict the global state of the magnetosphere-ionosphere system. J. Geophys. Res. 106, 30,067–30,076.

Ridley, A. J., Hansen, K. C., Tóth, G., De Zueew, D. L., Gombosi, T. I., Powell, K. G., 2002. University of Michigan MHD results of the GGCM metrics challenge. J. Geophys. Res. 107 (A10), 1290, doi:10.1029/2001JA000253.

Ridley, J. A., Liemohn, M. W., 2002. A model-derived storm time asymmetric ring current driven electric field description. J. Geophys. Res. 107 (A8), doi:10.1029/2001JA000051.

Rostoker, G., Akasofu, S.-I., Foster, J., Greenwald, R. A., Lui, A. T. Y., Kamide, Y., Kawasaki, K., McPherron, R. L., Russell, C. T., Apr. 1980. Magnetospheric substorms - Definition and signatures. J. Geophys. Res. 85, 1663–1668.

Rufenach, C., R.F. Martin, J., Sauer, H., 1989. A study of geosynchronous magnetopause crossing. J. Geophys. Res. 94, 15,125.

Russell, C. T., McPherron, R. L., Nov. 1973. The Magnetotail and Substorms. Space Science Reviews 15, 205–266.

Sandholt, P. E., Farrugia, C. J., Dec. 2003. Does the aurora provide evidence for the occurrence of antiparallel magnetopause reconnection? Journal of Geophysical Research (Space Physics) 108, 1466–+.

Sazykin, S. Y., 2000. Theoretical studies of penetration of magnetospheric electric fields to the ionosphere. Ph.D. thesis, Utah State University, Logan, Utah.

Scarpulla, J., Yarbrough, A., 2003. What Could Go Wrong? The Effects of Ionizing Radiation on Space Electronics. Crosslink 4, 15–19.

Sckopke, N., Paschmann, G., Haerendel, G., Sonnerup, B. U. O., Bame, S. J., Forbes, T. G., Hones, Jr., E. W., Russell, C. T., Apr. 1981. Structure of the low-latitude boundary layer. J. Geophys. Res. 86, 2099–2110.

Shelley, E. G., Johnson, R. G., Sharp, R. D., 1972. Satellite Observations of Energetic Heavy Ions during a Geomagnetic Storm. J. Geophys. Res. 77, 6104–6110.

Shelley, E. G., Johnson, R. G., Sharp, R. D., 1974. Morphology of Energetic O+ in the Magnetosphere. In: Magnetospheric Physics. Vol. 44 of Astrophysics and Space Science Library. pp. 135–+.

Simunac, K. D. C., Armstrong, T. P., Oct. 2004. Solar cycle variations in solar and interplanetary ions observed with Interplanetary Monitoring Platform 8. Journal of Geophysical Research (Space Physics) 109 (A18), 10101–+.

Siscoe, G. L., Erickson, G., Sonnerup, B., Maynard, N., Schoendorf, J., Siebert, K., Weimer, D., White, W., Wilson, G., 2002. Hill model of transpolar potential saturation: Comparisons with MHD simulations. J. Geophys. Res. 107, 1321.

Sonett, C. P., Jul 1960. Coupling of the solar wind and the exosphere. Phys. Rev. Lett. 5 (2), 46–48.

Song, P., Russell, C. T., 1992. A model of the formation of the low latitude boundary layer. J. Geophys. Res. 97, 1411.

Sonnerup, B. U. O., 1974. Magnetpause reconnection rate. J. Geophys. Res. 79, 1546.

Su, Y.-J., Horwitz, J. L., Moore, T. E., Giles, B. L., Chandler, M. O., Craven, P. D., Hirahara, M., Pollock, C. J., Dec. 1998. Polar wind survey with the Thermal Ion Dynamics Experiment/Plasma Source Instrument suite aboard POLAR 103, 29305–29338.

Sweet, P. A., 1958. The Neutral Point Theory of Solar Flares. In: Lehnert, B. (Ed.), Electromagnetic Phenomena in Cosmical Physics. Vol. 6 of IAU Symposium. pp. 123–+.

Temerin, M., Oct. 1986. Evidence for a large bulk ion conic heating region 13, 1059–1062.

Terasawa, T., Fujimoto, M., Mukai, T., Shinohara, I., Saito, Y., Yamamoto, T., Machida, S., Kokubun, S., Lazarus, A. J., Steinberg, J. T., Lepping, R. P., 1997. Solar wind control of density and temperature in the near-Earth plasma sheet: WIND/GEOTAIL collaboration 24, 935–938.

Thomsen, M., Noveroske, E., Borovsky, J., McComas, D., 1999. Calculation of moments from measurements by the Los Alamos magnetospheric plasma analyzer. Los Alamos National Laboratory Tech Report LA 135666-MS.

Thomsen, M. F., Borovsky, J. E., Skoug, R. M., Smith, C. W., Apr. 2003. Delivery of cold, dense plasma sheet material into the near-Earth region. Journal of Geophysical Research (Space Physics) 108, 1151–+.

Toffoletto, F., Sazykin, S., Spiro, R., Wolf, R., 2003. Inner magnetospheric modeling with the Rice Convection Model. Space Sci. Rev. 107, 175–196.

Tóth, G., Ma, Y. J., Gombosi, T. I., 2008. Hall magnetohydrodynamics on block adaptive grids. J. Comput. Phys. 227, 6967–6984.

Tóth, G., Odstrčil, D., Oct. 1996. Comparison of some flux corrected transport and total variation diminishing numerical schemes for hydrodynamic and megnetohydrodynamic problems. J. Comput. Phys. 128 (1), 82–100.

Tóth, G., Sokolov, I. V., Gombosi, T. I., Chesney, D. R., Clauer, C., Zeeuw, D. L. D., Hansen, K. C., Kane, K. J., Manchester, W. B., Powell, K. G., Ridley, A. J., Roussev, I. I., Stout, Q. F., Volberg, O., Wolf, R. A., Sazykin, S., Chan, A., Yu, B., Kóta, J., 2005. Space weather modeling framework: A new tool for the space science community. J. Geophys. Res. 110, A12226, doi:10.1029/2005JA011126.

Tóth, G., Zeeuw, D. L. D., Gombosi, T. I., Manchester, W. B., Ridley, A. J., Sokolov, I. V., Roussev, I. I., 2007. Sun to thermosphere simulation of the October 28-30, 2003 storm with the Space Weather Modeling Framework. Space Weather Journal 5, S06003.

Tsyganenko, N. A., 2002a. A model of the near magnetosphere with a dawn-dusk asymmetry - 1. mathematical structure. J. Geophys. Res. 107, 10.1029/2001JA000219.

Tsyganenko, N. A., 2002b. A model of the near magnetosphere with a dawn-dusk asymmetry - 2. parameterization and fitting to observations. J. Geophys.Res. 107, 10.1029/2001JA000220.

van Leer, B., Tai, C. H., Powell, K. G., 1989. Design of optimally-smoothing multi-stage schemes for the Euler equations. In: AIAA 9th Computational Fluid Dynamics Conference. AIA-89-1933-CP, Buffalo, New York.

Vasyliunas, V. M., 1970. Mathematical models of magnetospheric convection and its coupling to the ionosphere. In: McCormack, B. M. (Ed.), Particles and fields in the magnetosphere. D. Reidel Publishing, Dordrecht, Holland, pp. 60–71.

Wahlund, J.-E., Opgenoorth, H. J., Haggstrom, I., Winser, K. J., Jones, G. O. L., Mar. 1992. EISCAT observations of topside ionospheric ion outflows during auroral activity - Revisited 97, 3019–3037.

Wajima, K., Kawaguchi, N., Murata, Y., Hirabayashi, H., Dec. 2007. Radiation Testing of Consumer High-Speed LSI Chips for the Next Space VLBI Mission 59, 1221–+.

Wang, H., Ridley, A. J., Luhr, H., Mar. 2008. Validation of the Space Weather Modeling Framework using observations from CHAMP and DMSP. Space Weather 6.

Weimer, D., 1996. A flexible, IMF dependent model of high-latitude electric potential having "space weather" applications. Geophys. Res. Lett. 23, 2549.

Wilkinson, D., 1989. Trends in environmentally induced spacecraft anomalies. In: NASA/SDIO Space Environmental Effects on Materials Workshop. NASA Conf. Publ. 3035. Washington D.C., pp. 123–131.

Wilkinson, D. C., Daughtridge, S. C., Stone, J. L., Sauer, H. H., Darling, P., Dec. 1991. TDRS-1 single event upsets and the effect of the space environment. IEEE Transactions on Nuclear Science 38, 1708–1712.

Wilson, G. R., Sep. 1994. Kinetic modeling of O(+) upflows resulting from E x B convection heating in the high-latitude F region ionosphere 99, 17453–+.

Winglee, R. M., 1998. Multi-fluid simulations of the magnetosphere: The identification of the geopause and its variation with IMF. Geophys. Res. Lett. 25, 4441–4444.

Winglee, R. M., 2000. Mapping of ionospheric outflows into the magnetosphere for varying IMF conditions. J. Atmos. and Terr. Phys. 62, 527.

Winglee, R. M., Oct. 2003. Circulation of ionospheric and solar wind particle populations during extended southward interplanetary magnetic field. Journal of Geophysical Research (Space Physics) 108, 1385–+.

Wolf, R. A., 1983. The quasi-static (slow-flow) region of the magnetosphere. In: Carovillano, R. L., Forbes, J. M. (Eds.), Solar Terrestrial Physics. D. Reidel Publishing, Hingham, MA, pp. 303–368.

Wolf, R. A., Apr. 1995. Magnetospheric configuration. In: Kivelson, M. G., Russell, C. T. (Eds.), Introduction to Space Physics. Cambridge University Press, pp. 288–299.

Yau, A., André, M., 1997. Sources of ion outflow in the high latitude ionosphere. Space Sci. Rev. 80, 1.

Yu, Y., Ridley, A. J., May 2008. Validation of the space weather modeling framework using ground-based magnetometers. Space Weather 6, 5002–+.